DISCOVERY AND CHARACTERIZATION OF TRANSITING CIRCUMBINARY PLANETS FROM NASA's KEPLER MISSION

by

Veselin B. Kostov

A dissertation submitted to The Johns Hopkins University in conformity with the requirements for the degree of Doctor of Philosophy.

Baltimore, Maryland

August, 2014

Abstract

Planets with two suns have long fascinated our imagination yet it was only recently that astronomers were able to provide direct evidence of their existence. Several candidates have been proposed since 2003, based on measured timing variations in binary stellar systems, but it was not until 2011 and the launch of NASA's *Kepler* mission that circumbinary planets were unambiguously detected through their transits. At the time of writing, the peerless-quality data from *K*epler has enabled the confirmation of eight planets orbiting both members of seven gravitationally bound, eclipsing binaries (one of the systems has two circumbinary planets). This thesis presents our contribution to the field in terms of discovery and characterization of three of these transiting circumbinary planetary systems, specifically Kepler-47, Kepler-64, Kepler-413.

As predicted by theoretical models, the planets we discovered are smaller than Jupiter, have orbits close to the limit for dynamical stability, and are nearly co-planar to their host binaries (although the circumbinary system Kepler-413 is sufficiently misaligned that, due to fast orbital precession, the planet does not transit at every inferior conjunction). The results of our work deliver important insight into the nature of this remarkable new class of

objects, and provide deeper understanding of a) the type of binary stars that can support circumbinary planets; b) the orbital and physical properties of these fascinating systems (e.g. sizes, masses, orbital eccentricities, inclinations, precession rates); and c) planet formation and evolution in multiple stellar systems. Adding new members to the still small family of circumbinary planets has direct relevance for estimating the occurrence frequency of planets around binary stars in particular, and the Galactic planetary census in general, and for the extension of the concept of habitability to binary stellar systems.

Here we describe the unique observational signatures of transiting circumbinary planets, the detection method and analysis tools we developed to find and characterize these systems, and the theoretical implications of our discoveries. Specifically, we present the custom-built algorithm we invented to search for individual transit signatures in a light curve. We applied the algorithm to the light curves of ~ 800 eclipsing binaries from *K*epler, and discovered the aperiodic planetary transits in the three circumbinary systems mentioned above. To capitalize on these transits, we developed an analytical model that uses their measured depths and durations to constrain the properties of the host binary star. In addition, we present our ground-based spectroscopic and photometric observations that allowed us to measure the radial velocities of the circumbinary host stars and to constrain photometric contamination from unresolved sources. Finally, we discuss the photometric-dynamic model we developed and applied for the complete characterization of the transiting circumbinary systems Kepler-64 and Kepler-413.

Primary Reader: Peter R. McCullough

Secondary Reader: Holland C. Ford

Acknowledgements

I would like to thank Peter McCullough, Holland Ford, Colin Norman, and Zlatan Tsvetanov for their invaluable guidance, support, and encouragement to pursue my passion for finding planets; our collaborators Joshua Carter, Magali Deleuil, Rodrigo Díaz, Daniel Fabrycky, Guillaume Hébrard, Tobias Hinse, Tsevi Mazeh, Jerome Orosz, Jeff Valenti and William Welsh for their contribution and help; Dániel Apai for introducing me to exoplanet research, and giving me my first real taste of observational astronomy; the indispensable staff at Bloomberg and at STScI for always being there when I needed help; Peter Kunchev, Edward Baron, David Branch and Ronald Kantowski for seeing me through my first projects; the entire team behind the *Kepler* mission; and my friends Ivan Kirov, Krum Simeonov, Borislav Stoyanov, Alexander Atanasov, Pedro Llanos, Ye Zhang, Alireza Mortazavi, Bingxiao Xu, Daniel Allan, Daniel Richman, Justin Rogers, Nikolaus Hartman, and Waqas Bhatti for being with me along the way. Thank you!

The author gratefully acknowledges the financial support from NASA Origins of Solar Systems grant NNX10AG30G through Peter McCullough, from NESSF grant NNX13AM33H through Holland Ford, and from STScI Director's Discretionary Program through Dániel

Apai. This work is based on observations made with the *K*epler space telescope, which is funded by NASA's Science Mission Directorate, with the SOPHIE instrument on the 1.93-m telescope at Observatoire de Haute-Provence, and with the Dual-Imaging Spectrograph and the Near-Infrared Camera & Fabry-Perot Spectrometer on the 3.5-m Apache Point Telescope. This research made use of the SIMBAD database, operated at CDS, Strasbourg, France; data products from the Two Micron All Sky Survey, the Digitized Sky Survey, and the NASA exoplanet archive NexSci.

To my wife Tzveti, without whose support, patience and understanding none of this would have been possible; to my family – Dani, Dora, Boyan & grandma Veselina – for putting up with "you and your astronomy"; and to my uncle Misho – for getting me started on all of this. Thanks!

Contents

List of Tables

List of Figures

Chapter 1

Introduction

1.1 Exoplanets

Twenty years ago the only planets known to humanity were those of the Solar System. The road to discovery of extrasolar planets (or exoplanets) was long and difficult, built on determination and persistence. In 1855 W. Jacob (Jacob 1855) argued for the presence of an invisible third, planetary body in the 70 Ophiuchi binary star system that is gravitationally perturbing the observed orbit of the binary. Its existence was further proposed by T. See in 1896[1] (See 1896) and, half a century later, by Dirk & Holmberg (Dirk & Holmberg 1943), who also provided a mass estimate of 0.01 that of the Sun (but pointed out that it may not be stable). In 1988 W. Heintz (Heintz 1988) argued against the presence of the proposed third body by attributing the observed orbital perturbations of 70 Ophiuci to systematic effects.

[1] Who referred to it as a "dark satellite" but not as a planet.

Interest in this binary star system has not diminished, however, and new radial velocity observations have excluded the presence of planetary companions with $M_p \sin(i) \geq 7 M_{Jup}$ on circular orbits with periods of up to 5 years[2] (Wittenmyer et al. 2006). Another claim for an exoplanet detection was made by van de Kamp in 1963 (van de Kamp 1963) based on observations of astrometric variations in the apparent path on the sky of Barnard's star. After a twenty-five year long monitoring campaign of the star, the author suggested the presence of a planetary companion with a mass of $1.6 M_{Jup}$. After further analysis of the system, van de Kamp proposed an alternative scenario with two Jovian planets orbiting Barnard's star (van de Kamp 1969). Neither of these claims were confirmed independently (Gatewood & Eichhorn 1973). Recent observations of Barnard's star rule out the presence of planetary companions with $M_p \sin(i) \geq 10 M_{Earth}$ on orbital periods as long as two years (Choi et al. 2013).

It was not until the last decade of the twentieth century that exoplanets matured from candidates to confirmed planets. And the initial discoveries were of planets quite unlike the ones we were familiar with. Measurements of periodic variations in the pulse arrival times of the millisecond radio pulsar PSR1257+12 were attributed by Wolszczan & Frail to the gravitational perturbation from two Earth-mass planets (Wolszczan & Frail 1992), leading the authors to announce the first exoplanet detection[3]. Another first, an exoplanet orbiting around the solar-type star 51 Pegasi, was detected through measurements of the radial velocity Doppler shift of the host star's spectral lines caused by the gravitational in-

[2] Where i denotes the (unknown) inclination of the orbit.

[3] The presence of a third planet in the system was announced two years later (Wolszczan 1994).

fluence of the unseen planet (Mayor & Queloz 1995). An intriguing system indeed – the semi-major axis of the planet 51 Peg b (0.052 AU) is well within Mercury's orbit (0.39 AU)[4]. Dubbed a "Hot Jupiter", 51 Peg b has since proved to be a member of a distinct class of giant exoplanets on very short orbits (Howard et al. 2010; Seager & Lissauer 2011). In fact, Otto Struve suggested in 1952 (Struve 1952) that such planets may indeed exist and be detectable by the very same method that 51 Peg b was discovered. His second prediction, that these close-in planets could also be searched for photometrically by monitoring the stellar brightness for minima caused by a planet crossing in front of the host star, was validated in 2000 when Charbonneau et al. announced the first detection of a planetary transit across a stellar disk other than the Sun's – the hot Jupiter system HD209458 (Charbonneau et al. 2000), previously discovered by radial velocity measurements[5] (Mazeh et al. 2000).

The field of exoplanets has since blossomed as one of the most vibrant in modern astrophysics. Today it spans a vast landscape of planetary systems with incredible diversity in terms of architecture and orbital dynamics. Besides exoplanets around such exotic hosts as neutron stars, or those on short orbits around their main-sequence parent stars, recent years have seen a plethora of fascinating discoveries. From the perspective of the Solar System, some of the more unusual examples are of planets truly alien to human intuition. Astronomers have found planets on highly inclined (e.g. XO-3b, Hébrard et al. (2008); Winn et al. (2009)) or even retrograde orbits (e.g. WASP-17b, Anderson et al. (2010)),

[4]Even earlier radial velocity measurements of another system, HD 114762, have suggested the presence of a sub-stellar companion with a minimum mass of $M_p \sin(i) \sim 11 M_{Jup}$ (Latham et al. 1989)

[5]Lecavelier des Etang et al. (Lecavelier des Etang et al. 1995) argue for a detected transit of β Pic b in 1981 – a directly-imaged giant exoplanet discovered in 2008 (Lagrange et al. 2010).

star-less (or free floating) planets (Sumi et al. 2011), compact multiplanet systems (e.g. Kepler-11, a 6-planet-system inside the aphelion of Mercury, Lissauer et al. (2011a))[6], disintegrating planets (e.g. KIC 12557548b, Rappaport et al. (2012)), planets around evolved stars (e.g. HD 104985, Sato et al. (2003)), planets on highly eccentric orbits (e.g. HD 80606b with an eccentricity of $e \sim 0.93$, Fossey et al. (2009)) and as of 2011 – transiting planets that orbit both members of a gravitationally bound pair of main sequence stars[7].

The detection methods used to find exoplanets are as diverse as the discoveries they produce. Here we provide a list of some of the more successful efforts sorted by observing technique[8].

Dedicated ground-based facilities such the Hungarian Automated Telescope Network (HATNet, Bakos et al. (2004)), the Kilodegree Extremely Little Telescope (KELT, Beatty et al. (2012)), the MEarth Project (MEarth, Nutzman & Charbonneau (2006)), the Trans-Atlantic Exoplanet Survey (TrES, Alonso et al. (2004)), the Wide Angle Search for Planets (WASP, Pollacco et al. (2006)), and the XO Project (XO, McCullough et al. (2006)), together with space-based searches with the COnvection ROtation and planetary Transits mission (CoRoT, Boisnard & Auvergne (2004)), NASA's *Kepler* mission (Borucki et al. (2010)), the Microvariability and Oscillations of Stars mission (MOST, Walker et al.

[6]Throughout this thesis we will refer to a particular *Kepler* system as Kepler-NN, where NN will stand for its catalog number, and to any planets present in that system by adding lower-case "b,c,d" after the number, e.g. Kepler-NNb, -NNc, -NNd, etc.

[7]The first discovered circumbinary planet is non-transiting, and orbits around the pulsar binary B1620-26 (Sigurdsson et al. (2003)); there are also several non-transiting post-common envelope circumbinary planet candidates.

[8]For a comprehensive inventory of exoplanet searches and for detailed description of the detection methods we defer the reader to Fischer et al. (2014); Wright & Gaudi (2013), and http://www.exoplanet.eu/research/

(2003)) and the Sagittarius Window Eclipsing Extrasolar Planet Search (SWEEPS, Sahu et al. (2006)) monitor the brightness of tens of thousands of stars to capture a diminutive planetary transit across the disk of its parent star.

Custom-built spectrographs like the High Accuracy Radial velocity Planet Searcher (HARPS, Pepe et al. (2002a)), or the Spectrographe pour lObservation des Phnomnes des Intrieurs stellaires et des Exoplantes (SOPHIE; Bouchy et al. (2009)) along with their predecessors CORALIE (Queloz et al. 2000) and ELODIE (Baranne et al. 1996), and programs such as the Anglo-Australian Planet Search (Carter et al. 2003), the California Planet Survey (Marcy et al. 1997) or the MacDonald Observatory Planet Search (Cochran & Hatzes 2003), measure the tiny radial velocity Doppler shift in the spectral lines of a star due to its orbital motion around the common center of mass.

Planet hunters use the largest ground-based observatories Gemini, Keck, Subaru and the Very Large Telescope, augmented by sophisticated adaptive-optics systems designed to correct for image artifacts introduced by the instrument or the atmospheric turbulence, to obtain high-contrast images and directly capture photons from young, hot giant exoplanets (e.g. Chauvin et al. 2004; Currie et al. 2012, 2014; Lafrenière et al. 2010; Lagrange et al. 2010; Marois et al. 2010).

Surveys such as the Microlensing Observations in Astrophysics (MOA, Bond et al. (2004)) and the Optical Gravitational Lensing Experiment (OGLE, Udalski et al. (2003)) search for gravitational microlensing events caused by a chance alignment between a foreground exoplanet and a background source (Gaudi 2012).

Timing measurements uncover deviations from linear ephemeris in otherwise periodic astrophysical phenomena such as the eclipses of a stellar binary (or the pulsations of a neutron star, as discussed above) to infer gravitational perturbations caused by planetary-mass companions (e.g. Sigurdsson et al. (2003); Deeg et al. (2008); Beuermann et al. (2010, 2011); Qian et al. (2011, 2012a,b); Potter et al. (2011)).

At the time of writing, the astrometric method, measuring the sky motion of the host star around a common center of mass due to an unseen companion, has produced one planetary candidate (HD 176051 b, Muterspaugh et al. (2010)). The European Space Agency's Gaia Mission, launched in 2013, is expected to significantly increase this number (Sozzetti et al. 2013).

For completeness, we note that the presence of planetary candidates can also be inferred from asymmetries (or warps) in protoplanetary and debris disks caused by the gravitational perturbations from massive planets (e.g. Lagrange et al. (2010); Garufi et al. (2013); van der Marel et al. (2013); Facchini et al. (2014))

An essential synergy exists between the different detection techniques – for example, transit observations provide the orbital period, relative size with respect to the parent star and the orbital inclination of an exoplanet. These can be combined with independent estimates of the star's radius and with radial velocity measurements of its spectrum (to determine the planet's mass) to calculate the bulk density of the planet – an important aspect for understanding its formation and evolution. We will describe in Chapters 2 and 3 how the unique observational properties of transiting circumbinary planets enable measurements of

both their absolute size and mass even when the planets are not massive enough to imprint a detectable radial velocity signal on their parent stars.

At the time of writing, the discovery methods described above have identified a total of 1808 confirmed exoplanets, outlined in Table 1.1, and additional 4234 planetary candidates from *Kepler*[9]. The number of confirmed discoveries per year has been on a steep rise ever since 1989, as shown in Fig. 1.1. These exciting new discoveries have stimulated the pursuit of novel research directions in formation and evolution of planets, and the further development of observational techniques that push the limits of the available instruments ever forward.

[9]Morton & Johnson (2011); Lissauer et al. (2012) and Fressin et al. (2013) argue that most of *Kepler's* candidates are real planets.

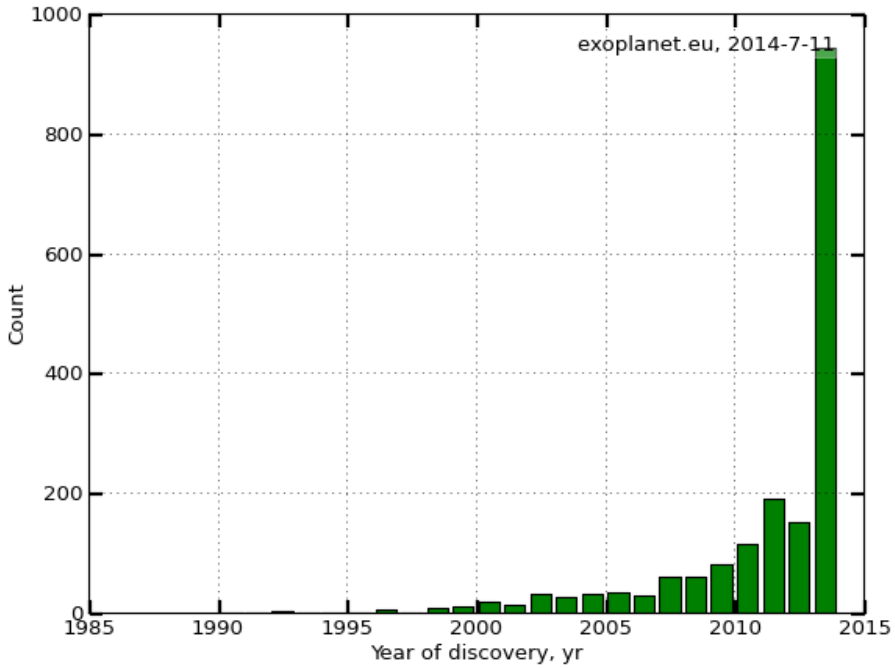

Figure 1.1 Number of confirmed exoplanet discoveries per year as of July, 2014 from all detection methods (excluding planetary candidates from *Kepler*). Data from http://exoplanets.eu/ (Schneider 2011)

Method	Transits	Radial Velocities	Imaging	Microlensing	Timing	Astrometry	*Kepler*†
Number of planets	1140	572	50	30	15	1	4234

†: Planetary candidates, data from http://kepler.nasa.gov/

Table 1.1 Confirmed exoplanets as of July, 2014, sorted by detection method. Data from the Extrasolar Planets Encyclopedia, http://exoplanets.eu/ (Schneider 2011).

With this thesis we aspire to contribute to the study of exoplanets in the dynamically-rich environments of close binary star systems. In particular, we use data from NASA's *Kepler* mission to discover and characterize transiting circumbinary planets (hereafter CBP). Our discoveries contribute to observational tests for specific theoretical predictions indicating that CBP should be a) common, and smaller in size compared to Jupiter, as suggested by numerical simulations (Pierens & Nelson 2007, 2008a,b,c, 2013); b) close to the critical limit for dynamical stability, shown in Fig. 1.2 (Holman & Wiegert 1999), due to orbital migration of the planet towards the edge of the inner disk cavity surrounding the binary star (Pierens & Nelson 2007, 2008a,b,c, 2013); and c) co-planar (to a few degrees) for binary stars with sub-AU semi-major axes due to disk-binary alignment on precession timescales (Foucart & Lai 2013, 2014). This thesis will advance our understanding of the nature of CBPs – what is their origin, how they evolve, and what type of stars can support them. In particular, our results will add new insights into the physics of planetary formation and migration in circumbinary disks. Theoretical models suggest that CBPs form further out in the disk and migrate inwards before stopping at their current location. Thus the observed orbital separations of CBPs will provide constraints on the properties of the protoplane-

tary disk they formed in (Pierens & Nelson 2007, 2008a,b,c, 2013; Kley & Haghighipour 2014). Additionally, as we will discuss in Chapter 3, our discovery of the circumbinary system Kepler-413 (Kostov et al. 2014) is an actual example system demonstrating a 20-year old prediction of the unique 'on-off' transit signatures of slightly misaligned CBPs (Schneider 1994).

Kepler-413, in particular, is also important for determining the occurrence frequency of transiting CBPs as the observational properties of the system suggest that abundance estimates need to take into account a distribution of possible planetary inclinations (Schneider 1994; Kostov et al. 2014; Martin & Triaud 2014; Armstrong et al. 2014). With several million *Kepler*-like CBP expected to orbit short-period binaries ($P < 50$ days) in the Milky Way, a lower limit suggested by preliminary estimates based on the known transiting CBP (Welsh et al. 2012), our discoveries have direct relevance for evaluating the planetary census in the Galaxy and for the extension of the concept of habitability to binary stars. More specifically, as we will show in Section 3.5.1, due to their rich orbital dynamics CBP experience significant variations in the incident stellar flux, which can have important implications for the habitability of CB Earth-size planets (and/or their hypothetical satellites).

In terms of stellar astrophysics, the transiting CBP we discover provide excellent measurements of the sizes and masses of the stellar components of the host binary stars. The measurements for the M-dwarf secondary stars in particular can contribute towards addressing a known tension between the predicted and observed characteristics of low-mass stars, where the stellar evolution models argue for smaller (and hotter) stars than measured

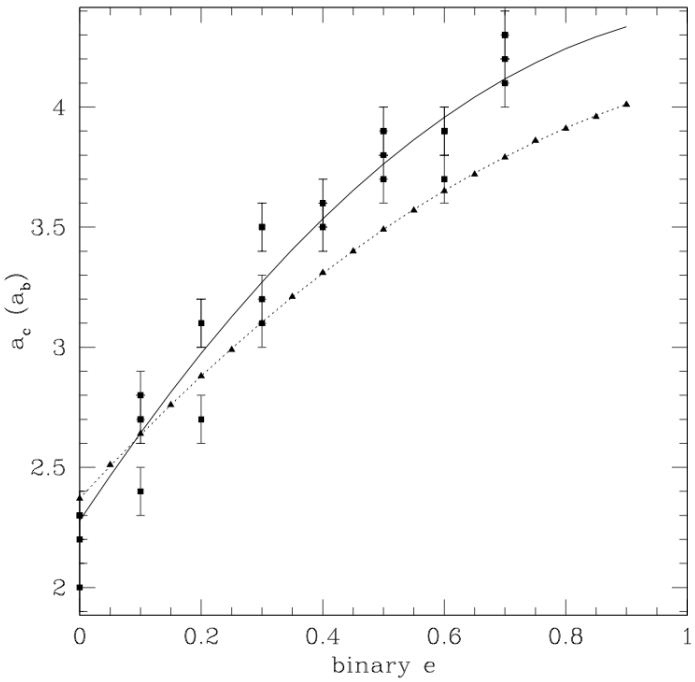

Figure 1.2 Dynamical stability limits for a CBP. The critical semi-major axis of the planet a_c (in terms of a_b, the semi-major axis of the binary) is a function of the binary eccentricity e and mass ratio (Figure 4 from Holman & Wiegert (1999)). For a given binary system, the minimum allowed distance from the two stars beyond which a CBP can have a dynamically stable orbit (the region above the lines) is typically on the order of a few binary star separations a_b. The square and triangle symbols represent the numerical results of Holman & Wiegert (1999) and of Dvorak et al. (1989) respectively (the integration time for the former is twenty times longer than the latter). The multiple square symbols per binary eccentricity indicate the stability limit for different mass ratio of the binary, $\mu = m_2/(m_1 + m_2)$ (from 0.1 to 0.5, lower to upper). The solid and dotted lines are the respective best-fits.

(Torres et al. 2010; Boyajian et al. 2012; Birkby et al. 2012). In addition, our discoveries shed new light on the still-uncertain mechanism for the formation of close binary systems (Tohline 2002). More specifically, the detected presence of a CBP strongly argues against a commonly favored formation scenario where a distant stellar companion drives tidal friction and Kozai-Lidov circularization (Kozai 1962; Lidov 1962; Fabrycky & Tremaine 2007b) of the initially wide host binary star towards its current close configuration. Under such scenario for the formation of a CBP system the binary star would have experienced excursions through the potential circumbinary disk, and sustained them on billion-year timescales – longer than the lifetime of the disk. Thus the host binaries of *Kepler's* CBP have probably achieved their present configuration via a different mechanism (Kratter & Shannon 2014).

As we demonstrate in this thesis, *Kepler* is well-suited for the detection and characterization of CBPs as it delivers, for the first time, continuous 4-years long, uninterrupted monitoring of more than 2000 eclipsing binaries (hereafter EB) (Prša et al. 2011) – an essential requirement for the detection of transiting CBP (Borucki & Summers 1984; Bell & Borucki 1995). To address the necessary steps leading to the detection of a CBP, we developed a suite of tools tailored to each particular aspect needed for its comprehensive discovery and characterization. Specifically, we invented a custom-built algorithm tailored to finding individual transit-like features in a light curve, which also allowed us to relax the assumption of strict co-planarity when searching for CBP transits. We applied the algorithm to the light curves of $\sim$ 800 *Kepler* EB (all detached EB with period greater than

3 days) to search for transiting CBP and detected several candidate systems. Next, we made ground-based observations of our best candidates to measure the radial velocities of the binary stars and to account for photometric contamination from unresolved sources. We also built a mathematical formalism, based on the observed duration and depth of the quasi-periodic transits of a CBP, to derive the a-priori unknown mass of the binary star – an important parameter for the analysis of the system. Finally, we developed a photometric-dynamical model based on a numerical three-body integrator to fully characterize a CB system in many-parameter space. These tools led us to the discovery of three of the currently known seven transiting CB systems. Compared to the total number of confirmed exoplanets, the known transiting CBP are a small but indispensable minority in the greater community of exoplanets. As the still low number statistics of CBPs limits our ability to properly characterize these fascinating systems, each of our discoveries contributed to their establishment as a new class of planets (Welsh et al. 2012).

The results from this thesis led us to the publication of two papers (reprints presented in Chapters 2 and 3). There are a few differences between these two papers and the respective chapters. We outline these differences at the beginning of each chapter and, where appropriate, annotate them throughout the text with [[ ]].

1.2 Outline of the thesis

The outline of this thesis is as follows. In Section 1.3 we describe the goal of the *Kepler* mission, touch on the properties of the observatory and the data it delivers, and highlight some milestone results. We provide an overview of the classification schemes of binary stars, and eclipsing binaries in particular, in Section 1.4, followed by an outline of the current census of CBPs in Section 1.5. Chapter 2 describes our discovery and characterization of the transiting CBP Kepler-64b and our independent confirmation of the CB system Kepler-47, and outlines our techniques and methods. In particular, we present the observational, analytical and numerical tools we developed for the proper characterization of a CB system, and discuss the implications of our findings. Chapter 3 describes our discovery of the slightly-misaligned and precessing CBP Kepler-413b that transits only occasionally, including a detailed discussion of the improvements we made to our detection and analysis techniques necessary to accommodate the unique observational signatures of the planet. We conclude this thesis in Chapter 4, where we summarize our results in the broader context of extrasolar planets and draw future prospects. We note that Veselin Kostov changed both his advisor and his research topic through his Ph.D. and published a third paper, a reprint of which is presented in Appendix A, where we describe the results from our work on mapping the atmospheric appearance of directly-imaged giant exoplanets. Specifically, we address the potential role of clouds in the observational signatures of such exoplanets and discuss how future observations will be able to constrain their properties through de-

tection of rotationally-modulated photometric and spectroscopic variability. Appendix B contains the acronym glossary.

1.3 NASA's *Kepler* mission

The *Kepler* satellite was launched on March, 7, 2009, with the goal to determine the occurrence frequency of Earth analogs[10] in the habitable zone[11] of stars similar to the Sun (Borucki et al. 2010; Koch et al. 2010). The telescope was originally trained for 4 consecutive years on a 115.6-square degrees area on the sky in the Cygnus region, and measured the brightness of ∼150,000 stars (of which ∼60% are G-type stars on or near the main sequence), searching for planets via the photometric transit method. The mission requirements were such that *Kepler* must be able to detect at least three consecutive transits of an Earth-like planet around a Solar-type star, where each transit (an 84 parts-per-million signal) is at least a 4-sigma detection in 6.5 hours[12].

The design of the mission is one of stability and simplicity. A 0.95-m diameter Schmidt telescope (with a 1.4-m diameter primary mirror and a field of view of 16 degrees in diameter) is placed on an Earth-trailing, heliocentric orbit which minimizes the influence from external torques (with the exception of Solar pressure), removes the effects of atmospheric drag, negates periodic heating (and induced voltage) from passing in and out of Earth's

[10] Small rocky planets.

[11] A spherical shell around the parent star where the incident stellar flux allows for liquid water on the surface of the planet.

[12] Corresponding to a maximum allowed noise level from all sources (i.e. measurement, shot, and stellar) of 20 parts-per-million per 6.5 hours for a V=12 magnitude star (Koch et al. 2010; Gilliland et al. 2011)

shadow, and avoids the influence from passing through the radiation belts (but can be hit by Solar flares). The only moving parts on the observatory are the reaction wheels that keep the pointing fixed during observations – there are no shutters and no filter wheel. With an orbital period of about 370 days, the telescope needs to rotate around its axis 4 times per year (so-called quarterly rolls) in order to keep its solar panels facing the Sun. The science camera consists of 42 charge-coupled devices which are read every 6.02 seconds. The detector has a plate scale of 3.98 arcsec per pixel (we will discuss the implications of the large pixel size in Sections 2.3.2 and 3.3.2) and covers the bandpass between 423 nm and 897 nm (where its spectral response function is greater than 5%), maximizing its sensitivity to solar-like stars while minimizing the effects of stellar variability (Koch et al. 2010). The primary data products are target-specific pixel data and light curves (i.e. stellar brightness as a function of time) obtained by aperture photometry over multiple pixels in two cadence modes: 30 min (long cadence) and 1 min (short cadence).

The original mission (spanning 2009 – 2013) was remarkably successful – it discovered 974 confirmed planets and 4234 candidates by 2014. Some of *Kepler*'s milestones towards achieving its goal include the discovery of a super-Earth planet ($R_p = 2.4R_{Earth}$) in the habitable zone of a star similar to the Sun (e.g. Kepler-22, Borucki et al. (2012)), two Earth-size planets ($\sim$0.9 and $\sim$1 R_{Earth}) transiting a solar-type star (e.g. Kepler-20ef, Fressin et al. (2012)), a five-planet system with two Earth-sized planets in the habitable zone of a K2V-star (e.g. Kepler-62ef, Borucki et al. (2013)), and an Earth-sized planet in the habitable zone of an M star (e.g. Kepler-186f, Quintana et al. (2014)). With the

recent failure of a second reaction wheel (May, 2013) the original mission has ended as the telescope can no longer sustain its required pointing stability with only two operational wheels. Despite this misfortune, *Kepler* is still observing, repurposed as K2 (Howell et al. 2014).

1.4 Binary Stars

The study of exoplanets is first and foremost the study of their parent stars. Binary stellar systems consist of two gravitationally-bound stars that orbit around their common center of mass. Nearly half of all Solar-type stars[13] are members of binary and higher-order stellar systems (Duquennoy & Mayor 1991; Raghavan et al. 2010). Up to 6% of these have orbital periods shorter than 50 days (Welsh et al. 2012) – the period range where the majority of of *Kepler*'s eclipsing binaries, and all of *Kepler*'s CBP eclipsing binary hosts reside. Here we outline the classification schemes for binary stars, with an emphasis on eclipsing binaries and their relevance for this thesis. For a comprehensive review on the subject we refer the reader to Hilditch (2001).

From an observational standpoint, binary stars are classified as: 1) Visual binaries, where the two stars are resolved as individual sources[14]; 2) Spectroscopic binaries (detected by the line-of-sight motion of one or both star through measurements of the Doppler shift of their spectral lines), subdivided into 2a) single-lined where only the spectral lines of

[13] Defined as F, G and K-type stars.

[14] Not to be confused with optical pairs, or optical binaries, where two stars that are not gravitationally associated happen to be close to each other on the sky.

one of the stars (usually referred to as the primary star) can be detected; and 2b) double-lined where the spectral lines of both the primary and the secondary stars can be detected; 3) Eclipsing binaries (provide relative sizes, orbits, luminosities and temperatures of the two stars), where the orbital orientation of the binary system with respect to the observer's line of sight is such that the two stars periodically eclipse each other. Depending on the configuration of the system and on the brightness ratio of the two stars, the observer can either see only a primary eclipse (when the secondary star moves across the disk of the primary star) or both primary and secondary eclipses; 4) Astrometric binaries, where the sky proper motion of the primary star around the common center-of-mass with an unseen companion can be detected.

Eclipsing binary stars, in particular, have paved the "royal road" to stellar astrophysics (Russell 1948) as calibrators for the fundamental properties of their component stars (i.e. mass, radius, temperature, luminosity) (Harmanec 1988; Southworth 2012). In Chapters 2 and 3 we will show how transiting CBP allow us to obtain the masses and sizes of both stars and of the planet, thus extending the "royal road" to the realm of exoplanets.

Binary systems where the two component stars are close enough to interact (e.g. exchange mass) due to stellar evolution (Paczyński 1971; Hilditch 2001) are defined as close binary stars. These systems are divided in three categories (Kopal 1955): a) Detached systems, where both stars reside inside their Roche lobes[15]; b) Semi-detached systems, where one of the stars has filled its Roche lobe due to stellar evolution, while the other is still

[15]The maximum volume around each star where matter belongs gravitationally to the star.

inside its Roche lobe; and c) Contact systems, where both stars have filled (or overfilled) their respective Roche lobes.

In this thesis we will focus exclusively on close eclipsing binary stars. The host stellar systems of the *Kepler* CBP we discovered are eclipsing, single-lined spectroscopic close binaries that exhibit both primary and secondary stellar eclipses. The *Kepler* EB Catalog (Prša et al. 2011; Slawson et al. 2011; Matijevič et al. 2012) contains 2165 objects[16] separated into five groups – 1261 detached, 152 semi-detached and 469 overcontact (i.e. overfilled, shared common envelope binaries) systems, together with 137 ellipsoidal variables[17] and 146 uncertain systems[18]. Each group is characterized by its distinct light curve: detached EBs have flat out-of-eclipse light curves (ignoring intrinsic stellar variability) and short, sharp stellar eclipses; semi-detached systems have more rounded out-of-eclipse regions and wider, yet still well-defined eclipses; the light curves of overcontact EBs have continuously varying out-of-eclipse sections and the stellar eclipses are less conspicuous in ingress and egress; ellipsoidal variables are characterized by sinusoidal or near-sinusoidal light curves (Prša et al. 2011). The entries in the catalog are further classified based on the morphology of their light curves by a parameter "c" ranging from 0 to 1, where $c = 0$ describes a completely detached EB and $c = 1$ describes an overcontact or ellipsoidal system. Example light curves for each group, phase-folded on their period, are shown in Fig. 1.3. For our search for transiting CBP we only used the *Kepler* light curves for the detached EB

[16]The latest version of the Catalog can be found at http://keplerebs.villanova.edu/

[17]Ellipsoidal variables describe systems where the stellar surfaces deviate from spherical and the light curves are dominated by the rotationally-modulated geometry of the stars.

[18]Systems that may not be binaries are classified as uncertain.

systems as they are generally easier to analyze due to less-pronounced stellar variability and more available data outside the stellar eclipses.[19]

1.5 Circumbinary Planets

Eclipsing binaries have long been thought of as ideal targets to search for transiting exoplanets (Borucki & Summers 1984; Schneider & Chevreton 1990; Schneider & Doyle 1995; Deeg et al. 1998). Early results on CM Draconis – a particularly well-suited EB composed of two M-dwarfs on a nearly edge-on orbit – suffered from incomplete temporal coverage and provided detection limits (Schneider & Doyle 1995; Doyle et al. 2000; Doyle & Deeg 2004). The continuous coverage of hundreds of EBs provided by *Kepler* notably improved the detectability of transiting CBPs. We note that CBPs are classified as P-type planets by Dvorak (1986).

Over the course of the last three years, data from *Kepler* has allowed us to confirm, for the first time, the existence of eight transiting circumbinary planets in seven systems. The discovery of the first transiting CBP was announced by Doyle et al. (2011) – a Saturn-sized planet orbiting the EB Kepler-16. The light curve of the system is shown on Fig. 1.4, where the prominent blue (depth of $\sim 15\%$) and yellow (depth of $\sim 2\%$) features define, respectively, the primary and secondary stellar eclipses. For this system the transits of the circumbinary planet across the primary star (green color, depth of $\sim 2\%$) are readily seen even by eye; we'll expand on this in Chapters 2 and 3. Several more transiting CBPs

[19] We will discuss these in more details in Chapters 2 and 3.

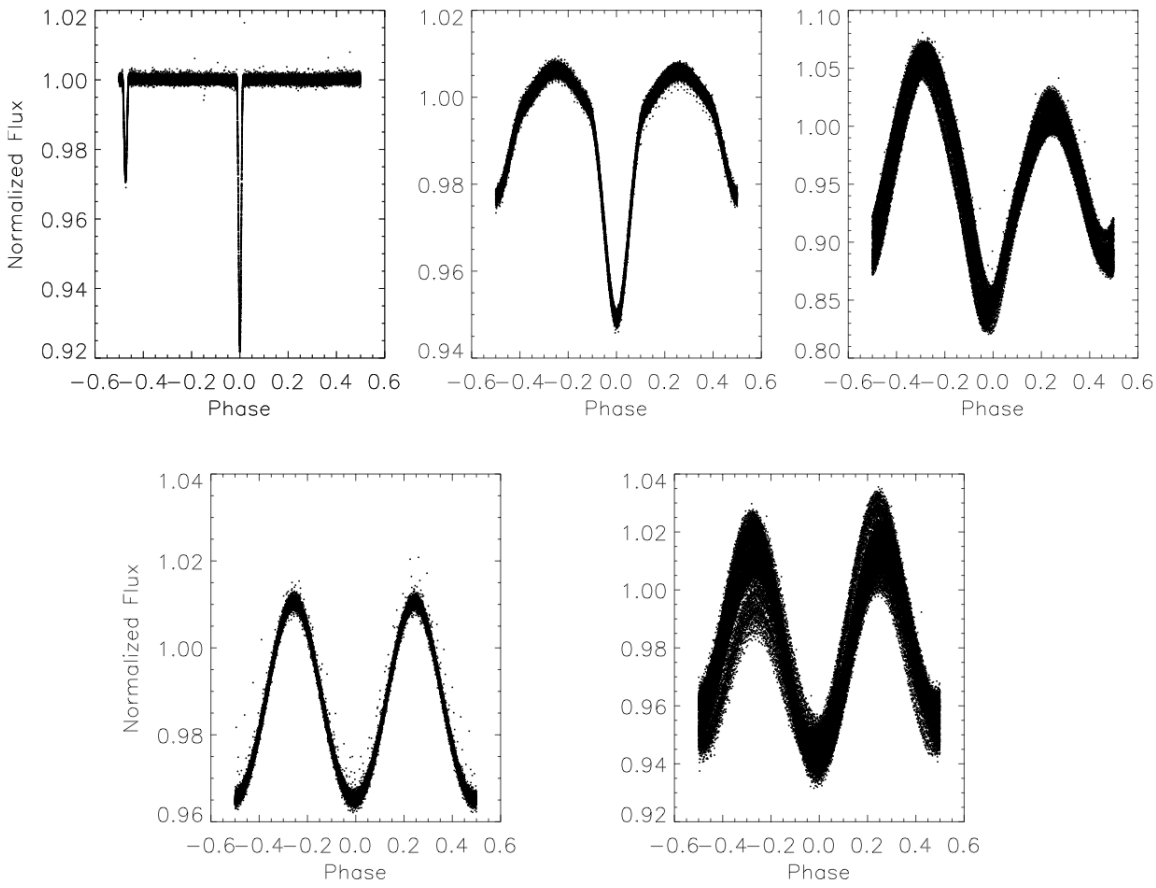

Figure 1.3 Example light curves of *Kepler* EBs (black symbols) as a function of the binary phase for detached (upper left, KIC 1026032), semi-detached (upper middle, KIC 7690843), overcontact (upper right, KIC 2302092), ellipsoidal (lower left, KIC 1868650) and uncertain systems (lower right, KIC 7204041) (Prša et al. 2011). The light curves shown here are detrended and normalized to unity. Data from http://keplerebs.villanova.edu/

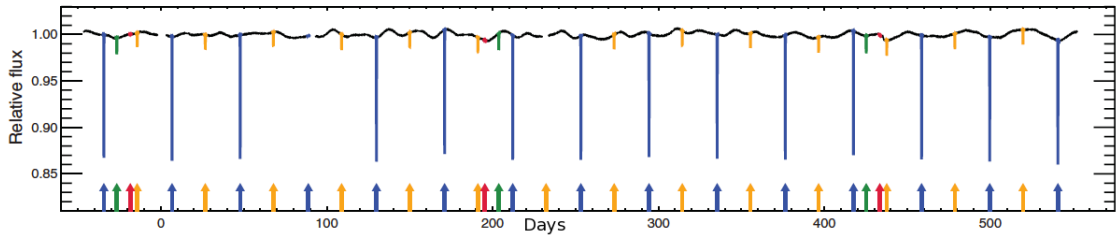

Figure 1.4 Light curve of Kepler-16 showing the primary and secondary stellar eclipses ($\sim$ 15% depth, blue and $\sim$ 2% depth, yellow respectively), and the primary (green) planetary transits (planet moves across the disk of the primary star). The secondary transits (planet crosses the disk of the secondary star) cannot be easily seen by eye on the figure. The reference epoch is BJD - 2,455,000. Figure 1 from Doyle et al. (2011).

promptly followed: Kepler-34b and Kepler-35b (Welsh et al. 2012), Kepler-38b (Orosz et al. 2012b), and the first multi-CBP system Kepler-47 (Orosz et al. 2012a). The discovery of the seventh CBP, Kepler-64b, was simultaneously announced by our team (Kostov et al. 2013) and by Planet Hunters (Schwamb et al. 2013). Another first - the slightly misaligned CBP Kepler-413b that often fails to transit its host EB at inferior conjunction due to quick orbital precession - was reported in Kostov et al. (2014), bringing the total number of confirmed transiting circumbinary planets to eight.

Chapter 2

A Gas Giant Circumbinary Planet Transiting the F Star Primary of the Eclipsing Binary Star Kepler-64 and the Independent Discovery and Characterization of the two transiting planets in the Kepler-47 System

Kostov, V. B.; McCullough, P. R.; Hinse, T. C.; Tsvetanov, Z. I.; Hébrard, G.; Díaz, R. F.; Deleuil, M.; Valenti, J. A., 2013, *The Astrophysical Journal*, **770**, 1

We note that for the circumbinary planet discovery we present in this chapter we use the label Kepler-64 instead of KIC 4862625 (used in the published paper) as the former is the official new identifier for this system.

Abstract

We report the discovery of a transiting, gas giant circumbinary planet orbiting the eclipsing binary Kepler-64 and describe our independent discovery of the two transiting planets orbiting Kepler-47 (Orosz et al. 2012a). We describe a simple and semi-automated procedure for identifying individual transits in light curves and present our follow-up measurements of the two circumbinary systems. For the Kepler-64 system, the 0.52 ± 0.018 $R_{Jupiter}$ radius planet revolves every $\sim$ 138 days and occults the 1.47 ± 0.08 $M_{\odot}$, 1.7 ± 0.06 $R_{\odot}$ F8 IV primary star producing aperiodic transits of variable durations commensurate with the configuration of the eclipsing binary star. Our best-fit model indicates the orbit has a semi-major axis of 0.64 AU and is slightly eccentric, $e = 0.1$. For the Kepler-47 system, we confirm the results of Orosz et al. (2012a). Modulations in the radial velocity of Kepler-64A are measured both spectroscopically and photometrically, i.e. via Doppler boosting, and produce similar results.

2.1 Introduction

For decades the science fiction community has imagined that planets can orbit binary stars, yet only recently have such systems actually been detected. Timing variations either in the rotation period of a neutron star member of a binary system (Sigurdsson et al., 2003) or in the stellar occultations (when the two stars eclipse each other) of eight eclipsing binary (EB) systems (Deeg et al. 2008; Lee et al. 2009; Beuermann et al. 2010, 2011; Potter et al. 2011; Qian et al. 2011; Qian et al. 2012) have been interpreted as the gravitational perturbation of additional bodies on the binary stellar system, suggesting the presence of a total of 12 circumbinary (CB) planets on wide orbits with periods of tens of years.

The lower limits on the masses of all twelve objects, however, fall in the super-Jupiter regime, making their planetary nature uncertain. Furthermore, the orbital stability of some of the multi-planet circumbinary systems (HW Vir, HU Aqr and NN Ser) have been studied recently, showing that some of them are on highly unstable orbits (Horner et al., 2011; Hinse et al., 2012; Horner et al., 2012a,b; Goździewski et al., 2012; Beuermann et al., 2012).

Doyle et al. (2011) announced the first direct evidence of a Saturn-sized planet that transits both members of an EB eclipsing binary, specifically Kepler-16. Since then, five more CB planets have been announced: Saturn-sized planets that transit Kepler-34b and Kepler-35b (Welsh et al. 2012), the first Neptune-sized planet that transits Kepler-38 (Orosz et al. 2012b), and two Neptune-sized planets that transit Kepler-47 (Orosz et al. 2012a).

The latter system is the first binary discovered to have two planets, one Neptune-sized on a 300 day orbit and the other Earth-sized on a 49.5 day orbit.

Substantial efforts in theoretical modeling indicate that planets such as these should not be uncommon. Simulations of dynamical stability show that beyond a critical distance, CB planets can have stable orbits in practically all binary configurations. The critical distance is on the order of a few binary separations (Dvorak 1986; Holman & Weigert 1999; Scholl et al. 2007; Haghighipour et al. 2010; Schwarz et al. 2011; Doolin & Blundell 2011). The orbits of Kepler-16b, 34b, 35b and 38b are indeed outside the critical orbital semi-major axis, but only by 21%, 24%, 14% and 26% respectively (Welsh et al. 2012; Orosz et al. 2012b). Kepler-47b, while notably farther from the instability region (Orosz et al. 2012a), is still not too far out, suggesting such "reaching for the limit" behavior to be typical of CB planets.

The fact that these four planets are so close to the theoretical limit for stability may suggest that their host systems had an interesting dynamical history where migration and/or planet-planet scattering may have played a significant role in sculpting their present architecture. Formation and evolution theory of giant planets around binary stars has been studied extensively (Pierens and Nelson 2007, 2008a, 2008b), providing a number of outcomes that depend on initial conditions. Simulations of gas giants have shown that Saturn-size planets (like Kepler-16b, 34b and 35b) stabilize at a 5:1 orbital resonance and may be very common, compared to Jupiter-size planets that are either scattered out of the system or gradually drift outward into the disk. Single, Neptune-size planets (such as Kepler-38b)

migrate and stop at a distance of about three times the binary stars separation, leading the authors to suggest that "the cavity edge of the precursor CB disk appears to be an excellent place to look for low mass planets in close binary systems." If there are two Neptune-size planets in the system, they become locked in a mean motion resonance, while a five-planet system is either disrupted or, in one simulation, also ends up in a resonance, implying that such multiple Neptune-size planets in resonant orbits may be indeed common. Models for the formation and evolution of terrestrial planets around binary stars (Quintana & Lissauer, 2006) have shown that, in the presence of Jupiter at 5 AU, CB terrestrial planets can readily form around a wide variety of binary systems. At least one terrestrial planet forms in all simulations presented by the authors. While the final masses of all simulated terrestrial planets vary little, the outcome for the architecture of the planetary system is very dependent on the parameters of the stellar binary. Highly eccentric binaries tend to harbor fewer, more diverse suites of planets compared to binaries with very low eccentricity, a prediction that can be addressed by the addition of more pictures to the family portrait of the five Kepler planets.

More than 20 years ago Borucki and Summers (1984) proposed monitoring EB systems to search for planets because a nearly edge-on inclination significantly increases the probability of transits. At the time it was not practical to monitor targets continuously over many days (Kepler-16b, for example, has an orbital period of 230 days). On March 6 of 2009, 380 years after Johannes Kepler predicted the transit of Venus across the disk of the Sun, NASA launched the appropriately named Kepler Mission to search for Earth-like planets in

the habitable zone of Solar-type stars and to determine their occurrence frequency (Borucki et al. 2010). To achieve this, a 0.95 Schmidt telescope on a Heliocentric Earth trailing orbit continuously and simultaneously monitors about 150,000 stars in the visible range from 423 nm to 897 nm over a 100 square degrees patch of the sky in the Cygnus region where $\sim 60\%$ of the stars are G-type stars on or near the Main Sequence. Utilizing the transit method, the instrument searches for periodic dips in the brightness of a star caused by a planet transiting across its disk. The Kepler mission has been remarkably successful in finding transiting planets, discovering more than 2300 planet candidates (Borucki et al. 2011; Batalha et al. 2012), 77 of which have been confirmed by the time of writing. Amongst this treasure throve of data are also a set of 2165 EB systems (Slawson et al. 2011), the main focus of our work.

Searching light curves of EB stars for transits of a third body is non-trivial. In addition to the significant limitations associated with intrinsic stellar variability and instrumental artifacts, CB planets have *[[varying]]* transit times, durations, and depths, all of which depend on the phase of the binary system (Schneider & Chevreton 1990). To transit one of the stars, the planet must "hit a moving target" (Orosz et al. 2012a). A benefit is that these transit signatures cannot be attributed to the stars themselves, to a background EB, or to other unrelated astrophysical or instrumental events, strongly supporting the CB-planet hypothesis. One challenge is that traditional transit searching algorithms, e.g. Box-fitting Least Squares (BLS) (Kovacs et al. 2002), used to detect periodic, box-like signals in the light curve of a single star are not optimized for finding transiting CB planets due to the

unique nature of their signal. Several methods for the detection of transiting CB planets have been proposed. One approach is based on simulating light curves produced by an exhaustive search of possible orbits of CB-planets and fitting them to the data (Doyle et al. 2000; Ofir 2008). Carter & Agol (2013) have developed the Quasi-periodic Automated Transit Search QATS algorithm, which is similar to BLS but optimized for aperiodic pulses. QATS has been successfully applied to CB-planets. Orosz et al. (2012) report that QATS failed to detect the outer planet Kepler-47c due to decreasing sensitivity for longer periods. While transiting gas giants cause a dimming of their host star large enough to be seen by eye in light curves, the transits of smaller planets can be easily missed by visual inspection.

The initial discovery of CB transits together with the availability of exquisite Kepler data inspired us to develop a semi-automated procedure to identify aperiodic transits. We describe the procedure, which is based on the established BLS algorithm but modified and applied in a novel way. We applied it to finding transiting planets around EB stars listed in the Kepler catalog of Slawson et al. (2011). We examined the detached EB systems and identified several candidates that exhibited additional transit-like features in their light curves. Here we present the independent discoveries of two CB planets Kepler-47bc and Kepler-64b.

In this paper, we will describe the analysis as a linear, deductive process, although it is inherently iterative, with one aspect feeding back into an earlier part. For brevity and clarity, we do not emphasize the iterations. This paper is organized as follows. In Section 2.2 we describe the procedure used to discover the two CB systems, followed by radial

velocity measurements and spectra of the host stars in Section 2.3. Our data analysis and initial diagnosis of the Kepler-64 system are outlined in Sections 2.4 and 2.5 respectively. We present our results in Section 2.6 and describe the dynamical stability of the Kepler-64 system in Section 2.7. In Section 3.5 we present our discussion and draw conclusions in Section 3.6.

2.2 Kepler Photometry

2.2.1 Detrending

We began with the long-cadence (∼30 min) PDCSAP flux of Kepler-64 generated by the Kepler mission for the publicly available[1] quarters 1-14. Using the ephemeris of Prša et al. (2011) and examining the phase-folded light curve, we flagged data points within 0.12 days of the centers of the primary or secondary eclipses, or within 0.5 days of the planetary transit events.[2] To remove the instrumental discontinuities in flux created by the quarterly rotation of the Kepler focal plane, we divide each quarter's data by its median. We flagged points that differed from the rest by more than 0.2% in normalized flux.

The unflagged flux is sinusoidal with a period of $p_{rot} \approx 2.63$ d, which we attribute to modulation caused by the rotation of star A. To detrend the flux variations attributed to rotation, for the purposes of providing eclipse and planetary transit light curves normalized

[1] http://archive.stsci.edu/kepler/ or http://exoplanetarchive.ipac.caltech.edu .

[2] This is one example of the iterative analysis: first we detrended the light curve, then we identified the planetary transits, then we detrended the light curve again with the transit points flagged.

to unity, we fit a unique sin wave in the local vicinity of each data point (58763 in total), in each case using unflagged data within $p_{rot}/2$ of each data point. Each of the 58763 sin waves had a fixed period, p_{rot}, and we fit for three parameters: the mean, the amplitude, and the phase. We iterated the procedure, adjusting the value of p_{rot}, until the gradient in the phase shifts of the fitted sin waves over the entire data span was zero, indicating a best-fitted average rotational period, $p_{rot} = 2.6382 \pm 0.0037$ d, where the quoted "uncertainty" is the standard deviation of p_{rot} fit piece-wise over quarterly time spans. Finally, we divided each data point by its best-fitting sine wave evaluated at the time of each particular data point. A small section of the light curve illustrating various features (stellar eclipses and planetary transit, rotational modulation, data gaps and glitches) is shown on Fig. 2.1. The part near the planetary transit where the best-fit sin wave deviates from the rest is caused by an instrumental effect, present in many other light curves. It does not affect the determination of the primary eclipse depth. We use the resulting detrended, normalized light curve for subsequent analysis, and we use the mean values of the sin waves for the analysis of the Doppler boosting (Section 2.4.4). Exclusive of flagged data, the RMS of the residuals of the detrended, normalized light curve about unity is 222 ppm.

2.2.2 Box-fitting Least Squares, BLS, for Single Transits

We invented a semi-automated procedure to identify individual, aperiodic transit-like features in a light curve. The procedure automatically finds square-wave or "box-shaped" features within a light curve.

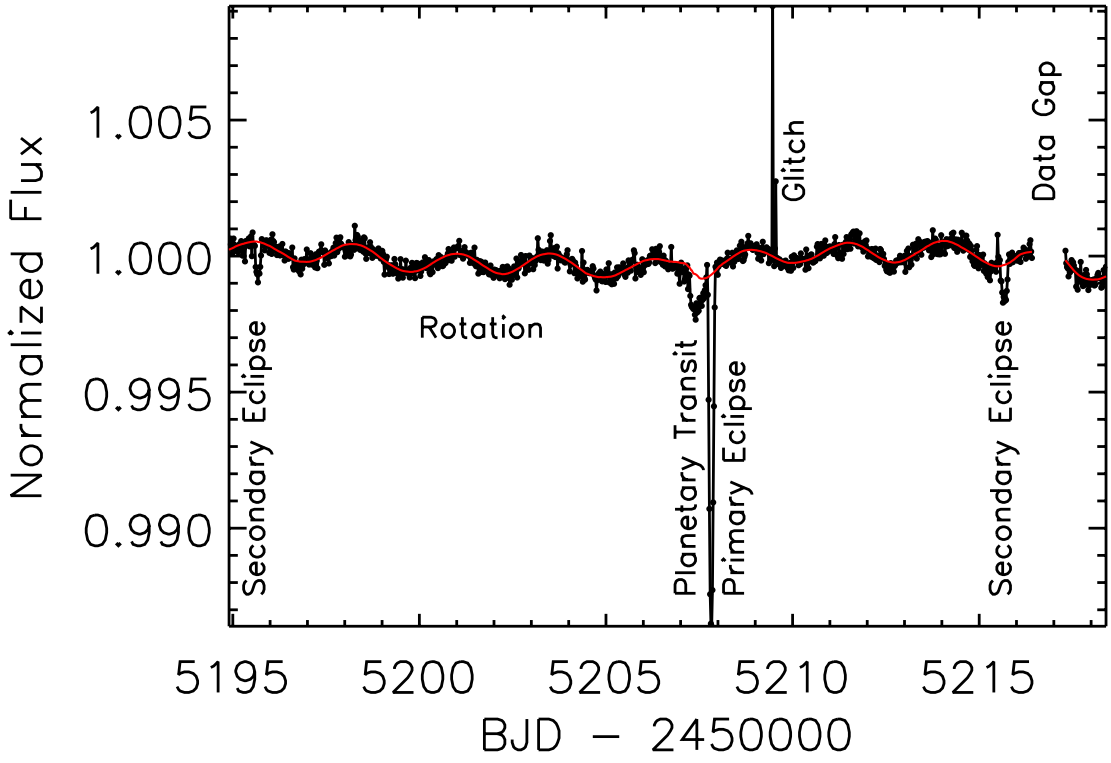

Figure 2.1 Characteristics of the light curve of Kepler-64. A 23-day portion of the Kepler light curve illustrates various phenomena. Instrumental effects are labeled above the data; astrophysical effects are labeled below the data. We flagged two data points as a "glitch," and a gap in the data is visible at BJD = 2455217. The eccentric orbit of the EB is apparent from the fact that primary eclipse is not centered in time between the two secondary eclipses. The primary eclipse is $\sim 1.4\%$ deep. The red line illustrates the sin-wave fit to the rotational modulation of the light curve. The secondary eclipses, the planetary transit, and the 2.6-day rotational modulation all have similar amplitudes, $\sim 0.1\%$.

Using the raw EB light curves SAPFLUX from the Kepler database we first normalize them and remove the EB's eclipses using the Box-fitting Least Squares method (BLS, Kovács et al. 2002). Next we detrend the data, using only those points with a SAPQUALITY flag of 0. The detrending is non-trivial and has to be done on a target-by-target basis, as each binary star has complex baseline variability that spans timescales from hours to days. We use an iterative fit with a high-order Legendre polynomial on each quarter, further broken down into smaller segments according to the data flags.

Within each segment of the light curve, the procedure automatically identifies the center, width, and depth of the two most-significant box-shaped features, one positive and one negative. The latter is a "transit" candidate and the former is an "anti-transit." Because transits are negative features in the residuals of a detrended light curve, we can validate empirically the statistical significance of the transit candidates by comparison with the anti-transits extracted from the same data. Doing so helps us to not be overwhelmed with false-positives.

The number M of light-curve segments is not particularly critical. The segment length should be longer than any actual transit. For CB planets, in principle the transits can be as long as half an orbit of the EB, in the case where the planet and the star are traveling in parallel at nearly the same projected rate (Schneider & Chevreton 1990). Such transits will be rare and generally accompanied by shorter transits, created when the planet and star are moving in opposite directions. The segment length should be shorter than the orbital period of the planet, lest only one of two genuine transits be identified in a segment. For CB

planets of P-type (Dvorak 1982), the planet's orbital period must be longer than the period of the EB, and for orbital stability the CB planet's period must be at least a few times longer than the EB's period (Section 2.7). From these two limits, the segment length should be between one half and a few times the orbital period of the EB. However, in practice, the intrinsic variability of the stars in the system [[determine]] the length of the segment. In any case, to prevent a transit being split by the segment boundaries, we analyze each light curve at least twice with the boundaries of the segments shifted.

In all cases, detrending of the light curve is crucial to our method. Very short-period EB stars, contact, and semi-detached EBs are difficult to study with our method. They are highly variable and there are few measurements in between the stellar eclipses, forcing us to use segments much larger than the binary period.

To avoid systematic effects that might mimic a transit, a merit criterion is necessary. As a convenience, one can use the BLS algorithm to find the individual transit- and anti-transit-features in segments of the detrended light curve's residuals. Because BLS is designed to find *periodic* box-like features, one option is to replicate N times the segment under study to form a periodic light curve. One can then use BLS to search for the most significant transit- and anti-transit features with that single period defined by the replication. The number N of replications is not particularly important. To find the anti-transits, we simply invert the sign of the residuals of the light curve and search a second time. Although it would be more efficient to extract the most-significant positive and negative features in one pass, the execution time is trivial and enormously smaller than in the traditional BLS

which must loop over thousands of trial periods, and smaller than the detrending also. Alternatively one can modify the original BLS computer code to analyze a single segment of unreplicated data; we have implemented each variant. The only potential difference is a tuning parameter within BLS, namely the minimum number of data points within an acceptable box-like feature, which must be adjusted commensurate with the number of replications N.

After the automated procedure identifies the M most-significant pairs of transit- and anti-transit-candidates from the M segments, we examine the ensemble for outlier transit-candidates in a manner similar to that described by Burke et al. (2006). Burke et al. validated transit-like features with an ensemble of features reported by BLS for hundreds of stars observed simultaneously. Because of the large number of observations in each star's Kepler light curve, we validate transit-like features in each light curve with the ensemble of transit- and anti-transit features from only that particular light curve.

For completeness, we briefly describe Burke's method here. Assuming dimming features (transits) and brightening features ("anti-transits") are due to systematic effects, it is reasonable to expect that there will not be a strong tendency for such effects to produce dips versus blips. In other words, typically $\delta_{(\chi^2)transit}$ will be similar to $\delta_{(\chi^2)anti-transit}$ for each segment. On the other hand, a highly significant transit signal is an outlier in a $\delta_{(\chi^2)transit}$ and $\delta_{(\chi^2)antitransit}$ diagram (Figure 2.2). The segments where noise dominates (black crosses) cluster in a cloud of points with similar values for $\delta_{(\chi^2)transit}$ and $\delta_{(\chi^2)anti-transit}$, but the segments containing the tertiary transits (red symbols) are well sep-

arated. As seen from the figure (and depending on the merit criterion) there can be a significant number of outliers, requiring a human eye to check the segments which triggered the routine. The number of triggers are highly dependent on the detrending of the baseline – quiet stars (like Kepler-16) have very few outlying points (planetary transits) where smaller transit signals in more variable binaries (Kepler-47) will be accompanied by a greater number of false positives. While non-trivial, the number of outliers that pass inspection is still much smaller than the total number of segments – typically not more than 10% of the entire light curve.

Figures 2.2, 2.3 and 2.4 show examples from the light curves for Kepler-64, Kepler-47 and Kepler-16 using data from Quarters 1 through 14. [3]

To evaluate the sensitivity of our method, we insert [[artificial]] transits in the light curves and study their recovery rate as a function of the transit depth. An example for Kepler-16 is shown on Figure 2.4 where the black crosses represents segments with no fake transits, red symbols are due to Kepler-16b and the blue diamonds correspond to segments in which [[injected]] transits with a depth of 200 ppm ($\sim 1.5 R_{Earth}$ signal) were superposed. The fake transits have variable depths, durations, and period to simulate those expected for a CB planet [[orbiting]] outside the critical semimajor axis for stability in the system. Not all of the fake transits are recovered: some fall into data gaps, others into noisier parts of the light curve. However, for the case of Kepler-16, simulations of

[3] Earlier versions of the three figures, based on only Quarters 1 to 6, were presented on February 8, 2012 to a committee of Johns Hopkins University as part of the graduate student matriculation procedures for one of us (V.B.K.).

super-Earth transits resulted in a 75% recovery rate. As seen from Figure 2.4, the majority of the inserted fakes occupy a clearly-defined cloud, well-separated from the transit-free segments.

Their recovery rate is used to adopt the target-specific merit criterion mentioned above, defined in terms of the ratio between $\chi^2_{transit}$ and $\chi^2_{anti-transit}$ (dotted blue line on Figures 2.2, 2.3 and 2.4). Only those segments that fall above an iteratively chosen ratio (2 in the three cases shown here) are inspected visually in the raw data for known systematic features, for centroid shifts, and for binary star period commensurability for those systems without well-defined secondary eclipses. As seen from Figure 2.2, one of the planetary transits falls short of the cut criterion with a ratio of 1.01 and another is very close (ratio of 1.1) – the detrending was not optimal and, due to the long duration of the two transits, significantly dampened them, mistaking them for baseline variability. The transits that do not fulfill the cut criteria for the case of Kepler-47 (Figure 2.3) do so for a different reason – they are very weak and are difficult to discern from the noise. The sheer number of tertiary events, however, promoted very careful visual examination of the light curves of both targets which ultimately revealed those missed by the automatic procedure as well. This shows that the described method works well for finding not only individual transits but, depending on circumstances, also for super-Earth transits of quiet stars and even for transits with durations as short as only three low-cadence Kepler samples, e.g. the quaternary eclipse of Kepler-16b.

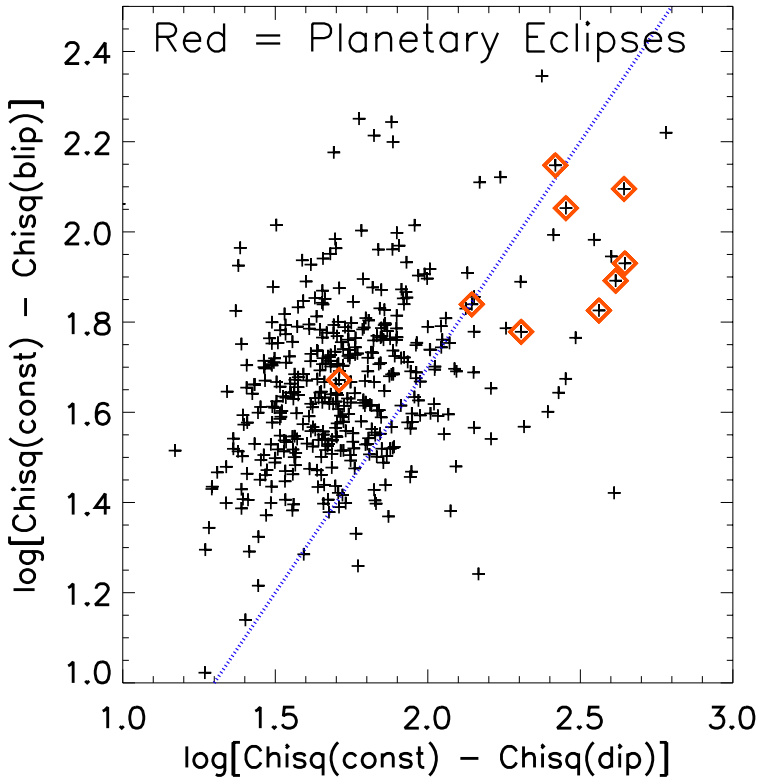

Figure 2.2 The transit/anti-transit diagram for Kepler-64b. The red symbols represent the planetary transits and the dotted blue line – the merit criterion used.

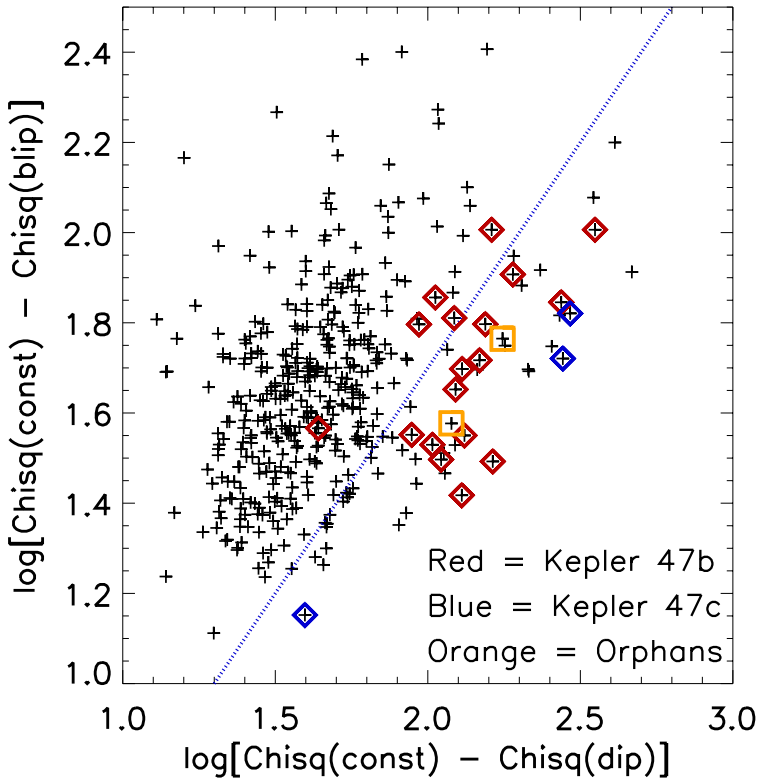

Figure 2.3 The transit/anti-transit diagram for KIC 10020423, a.k.a. Kepler-47. The different colors represent planets 47b (red) and 47c (blue) and two additional transits (orange) not associated with either of them.

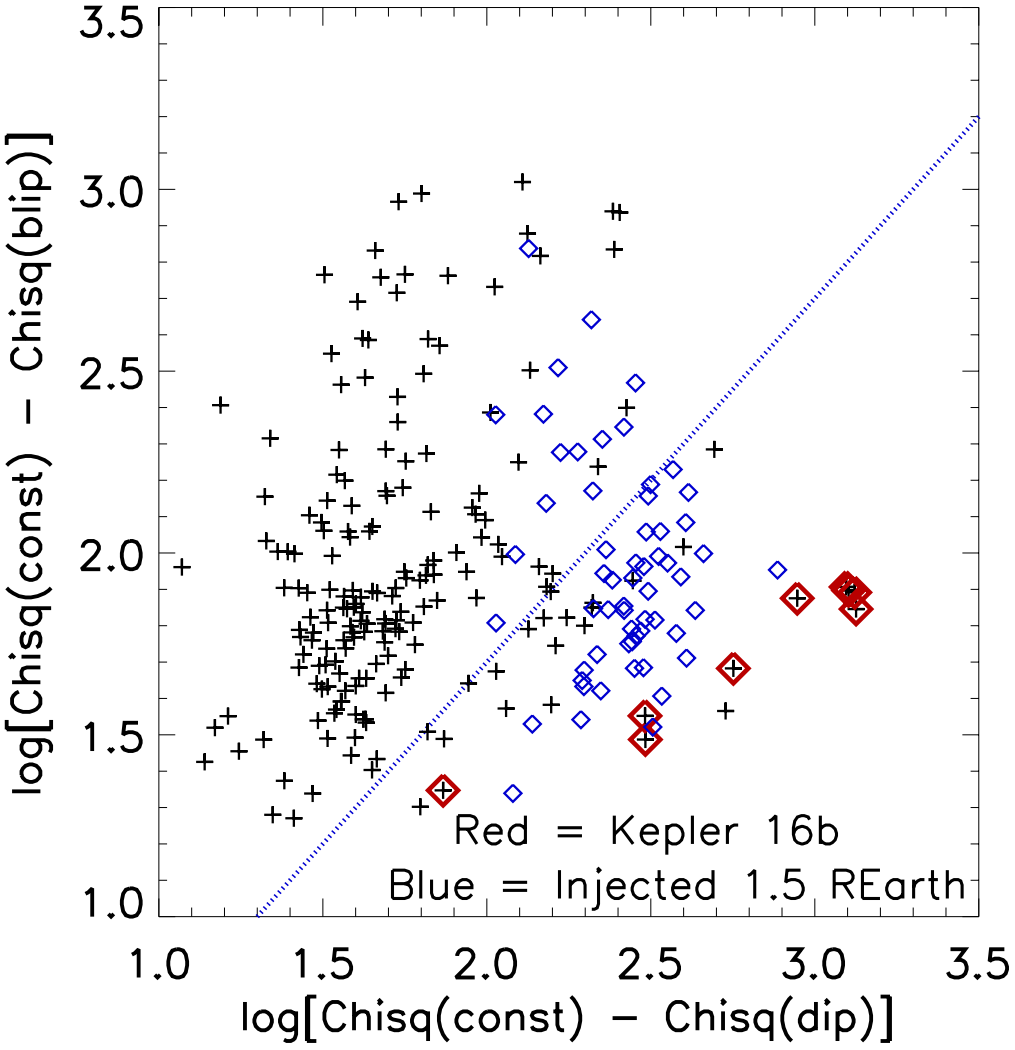

Figure 2.4 The transit/anti-transit diagram for Kepler-16 with simulated transits of an $1.5R_{Earth}$ planet superposed (blue). The red diamonds represent the transits of Kepler-16b.

2.3 Spectra

2.3.1 Apache Point Observatory Observations

Kepler-64 and Kepler-47 were observed with the 3.5 m telescope at the Apache Point Observatory on four occasions between April and July, 2012. Coincidentally, the spectroscopic observations of Kepler-47 by Orosz et al. (2012) and ourselves began within 48 hours of each other. We used the medium dispersion Dual Imaging Spectrograph (DIS) in its highest resolution spectroscopic mode. The pair of B1200/R1200 gratings in combination with the $1.5''$ slit delivers a spectrum with resolution R$\sim$3000 and covering simultaneously two 1200Å windows centered on 4500Åand 6500Å, respectively. The slit was oriented along the parallactic angle. Each night we obtained one or two exposures of each target supplemented by exposures of spectrophotometric and radial velocity standards. Nightly we also obtained several HeNeAr lamp spectra for wavelength calibration, and we used telluric lines in the observed spectra to correct for offsets due to flexure or other instrumental effects. Conditions of all four nights were not strictly photometric. Each target was observed for $\sim$900 seconds per night, yielding a peak signal to noise ratio in the continuum of 20 to 30 per resolution element.

The data reduction included bias and flat-field correction, aperture extraction, wavelength and flux calibration. We compared the APO long-slit spectrum of Kepler-64 with a library of stellar spectra (Pickles 1998). For the R$\sim$3000 APO spectra, the FWHM $\sim$45

km s^{-1} broadening evident in the SOPHIE spectra (Section 2.3.2) is unresolved. We estimate from the shape of the continuum and strengths of particular spectral lines that the best match is spectral type F8 IV. The subgiant classification is consistent with the density of star A determined later from the light curve and the mass function. The Kepler Input Catalog (KIC) tends to over estimate log(g) for subgiants, especially those hotter than about 5400 K, which can lead to underestimates of their radii in the KIC, typically by factors of 1.5 to 2 (Brown et al. 2011). For Kepler-64, the KIC radius estimate is 0.806 $R_{\odot}$, indeed approximately half the size that we estimate in this work.

2.3.2 SOPHIE observations and data reduction

The two targets were observed at the end of summer 2012 with the SOPHIE spectrograph at the 1.93-m telescope of Haute-Provence Observatory, France. The goal was to detect the reflex motion of the primary stars due to their secondary components through radial velocity variations. SOPHIE (Bouchy et al. 2009) is a fiber-fed, cross-dispersed, environmentally stabilized echelle spectrograph dedicated to high-precision radial velocity measurements. For such binary systems the amplitudes of variation are expected to be of the order of a few to a few tens km s^{-1}, which is well within the capabilities of SOPHIE despite the faintness of the targets. The data were secured in High-Efficiency mode (resolution power $R = 40\,000$) and slow read-out mode of the detector. In order to reach a signal-to-noise ratio per pixel of the order of 10 at 550 nm, exposure times ranged between 1200 and 2000 sec for Kepler-47, and between 500 and 900 sec for Kepler-64.

The spectra were extracted from the detector images with the SOPHIE pipeline, which includes localization of the spectral orders on the 2D-images, optimal order extraction, cosmic-ray rejection, wavelength calibration and corrections of flat-field. Then we performed a cross-correlation of the extracted spectra with a G2-type numerical mask including more than 3500 lines, and finally measured the radial velocities from Gaussian fits of the cross-correlation functions (CCFs) and the associated photon-noise errors, following the method described by Baranne et al. (1996) and Pepe et al. (2002). For Kepler-47 and Kepler-64 respectively, the full widths at half maximum of those Gaussians are 12 ± 1 km s^{-1} and 15 ± 2 km s^{-1}, and their contrasts are 17 ± 4 % and 4 ± 2 % of the continua. One of the observations of Kepler-64 was made at twilight: the pollution due to the bright sky background was corrected thanks to the reference fiber pointed on the sky (e.g. Hébrard et al. 2008). Other exposures were not polluted by sky background nor Moon light. In Table 2.1 the SOPHIE radial velocities are absolute in barycentric reference, whereas the APO radial velocities are absolute for Kepler-64 and relative for Kepler-47.

Simultaneously with the publication of our results, Schwamb et al. (2012) published their study of Kepler-64. The main difference in the two analyses is that we assumed there is only one star in the SOPHIE aperture, whereas Schwamb et al. (2012) have shown that there is a significant contaminant at 0.7 ″from the primary star, that contaminant being itself a binary. The contaminant is well within the 3 ″SOPHIE aperture. Whereas it is clearly detected in the broadening function of the HIRES spectra of Schwamb et al. (2012) (their Figure 7), it is not as clear in the SOPHIE CCFs.

With that in mind we reinspected the SOPHIE CCFs. By letting a second peak free to vary in each of the eight SOPHIE spectra, we did not significantly detect it. However, by assuming that second peak is not varying with time (the variations seen with HIRES are small), it is detected in the SOPHIE spectra at a radial velocity of -22.7 ± 0.7 km s^{-1}, FWHM $= 8.9^{+2.4}_{-1.6}$ km s^{-1} and a contrast of $= 0.53^{+0.14}_{-0.17}$ % of the continua. So there is a 3.8-σ detection of the second peak on the total data of the eight SOPHIE spectra. We revised the SOPHIE radial velocity measurements of Kepler-64 taking into account for that additional peak in the CCFs. The resulting radial velocities differ by at most 2σ from the radial velocities obtained without taking into account the second peak. The final radial velocities of both stars are reported in Table 2.1.

Radial velocity variations in phase with the Kepler ephemeris are clearly detected. Section 2.4.3 addresses the orbital parameters derived from the radial velocities in combination with the light curve. Section 2.4.2 addresses atmospheric parameters of star A derived from the spectra.

2.4 Data Analysis

2.4.1 Eclipsing Binary Light Curve

The light curve of the [[Kepler-64]] EB star constrains the *relative* orbit of the two stars: the orbital period P, the center times of primary eclipse T_t and secondary eclipse T_o, the

semi-major axis of the relative orbit in units of the radius of star A, a/r_A, and the orbital inclination, i. Also from the light curve, we derive the relative radii of the two stars, $k = r_B/r_A$, and the fraction of the flux in the Kepler bandpass[4] emitted by star B, f_B. Nominally, we assume zero "third light," so $f_A = 1 - f_B$; we examine that assumption later in this section. We adopt the period $P = 20.000214$ d from Prša et al. (2010), although the trend in the eclipse timing variations suggest a period $\sim$2 seconds longer. The free parameters of the fit to the light curve are $T_t, T_o, a/r_A, p, i,$ and f_B. We compute the fraction of light blocked by one star by the other using computer code of Mandel & Agol (2002). Because the latter code was designed for planetary transits and models the nearer body as an entirely dark and opaque circular disk, we account for the light from the nearer star appropriately by superposition. The phase-folded light curve is shown on Fig. 2.5

We estimate the limb darkening parameters $(u_{1,A}, u_{2,A}) = (0.243, 0.371)$ and $(u_{1,B}, u_{2,B}) = (0.112, 0.350)$ for stars A and B respectively, by interpolation of tables of R-band theoretical quadratic limb-darkening coefficients (Claret 2000) as appropriate for their effective temperatures, gravities, and metalicities (Table 2.2). For star A, those are estimated from spectroscopy (Section 2.4.2). For star B, we estimate its effective temperature $T_{eff} = 3390 \pm 50$ K, by interpolating a grid of model atmosphere spectra (Hauschildt et al. 1999[5]) to match the depth of the light curve at secondary eclipse; we integrate the spectra over the Kepler bandpass and compare to that of star A, accounting also for the relative solid angles, k^2. We estimate star B's gravity log(g) = 4.94 in cgs units from its mass

[4] http://keplergo.arc.nasa.gov/CalibrationResponse.shtml

[5] Machine-readable tables are available at http://svo.cab.inta-csic.es/theory/db2vo/index.php .

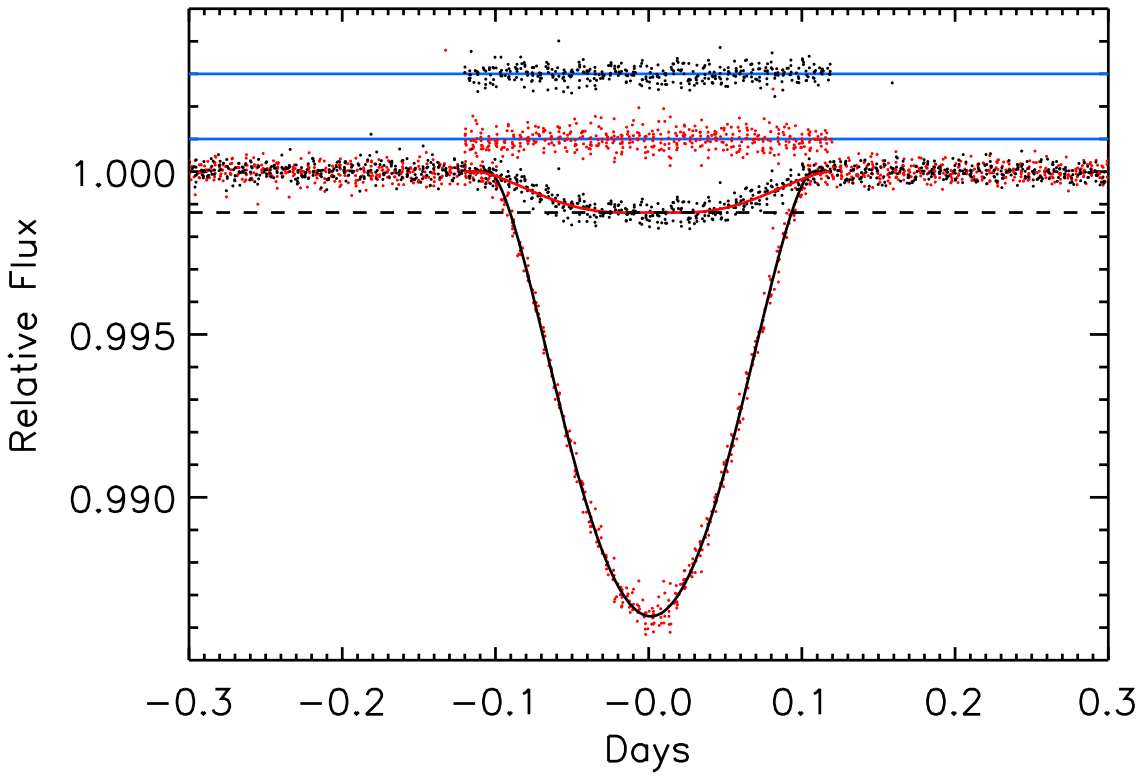

Figure 2.5 Kepler light curves of Kepler-64. The normalized and detrended flux of the primary and secondary eclipses are shown with respect to the orbital phase of the EB, along with the binary star model. The secondary eclipse data have been centered at zero phase for comparison with the primary eclipse data. The secondary eclipse data and the residuals (above) have been offset vertically for clarity.

$0.37 \pm 0.035\ M_\odot$ and radius $0.34\ \pm 0.015\ R_\odot$. We assume star B's metalicity is equal to that of star A.

We derive the quantity $e(\cos\omega)/\sqrt{1-e^2}$ from the phase of the center of the secondary eclipse relative to the center of primary eclipse. For the latter constraint, we used the analytic approximation for the case of inclination $i = 90^\circ$ (Hilditch 2001, Eq. 5.67), and verified that the difference between that approximation and the numerical estimate for $i > 87^\circ$ is negligible (Hilditch Eq. 5.63). Similarly, the quantity $esin\omega$ equals the ratio of the difference to the sum of the durations of secondary and primary eclipses (Hilditch Eq. 5.69). However, because the eclipse durations are much less precisely measured than the centers, we do not explictly constrain $esin\omega$, although it is weakly constrained implicitly in fitting the light curve. Instead, ω is measured better using the radial velocities (Section 2.4.3).[6]

Given the above constraints from the light curve, fitting the radial velocities depends on only three astrophysical free parameters: the systemic velocity γ, the velocity semi-amplitude k_1, and the longitude of periastron ω. In our analysis, once ω is measured using the radial velocities, the eccentricity e and the time of periastron passage t_{peri} are analytically constrained from the light curve (Hilditch Eqs. 4.10 and 5.67). Similarly, the uncertainties in the parameters e and t_{peri} flow down from the uncertainty in ω determined from the radial velocities.

[6]We have adopted the equations and viewing geometry of Hilditch's textbook, Figure 2.5. Apparently, prior publications of CB planets have adopted the opposite viewing geometry, e.g. Fig. 7 of Murray & Correia (2010). This affects ω by 180°.

The planetary transits of star B, if they occur, are undetectable in the Kepler photometry. Because star B contributes only $f_B = 0.00124$ of the flux of the system, and its relative solid angle $k^2 = 0.0426$, the mean surface brightness of star B is 0.029 that of star A, in the Kepler bandpass. Given that the planet blocks $\sim$0.1% of the system's light when transiting star A, we predict only a 30 ppm planetary transit of star B, i.e. undetectable with Kepler's per-cadence RMS noise of 222 ppm. Because CB transit durations can be no longer than half of the orbital period of the EB (Schneider & Chevreton 1990), or 10 days in this case, and even with an idealized 10-day upper-limit on the duration, the 30-ppm transit depth would correspond to $\sim 3\sigma$, and typically not even that, due to long-term intrinsic variations in the system's total light.

In the above analysis, we have assumed that the Kepler photometer records the sum of the light from the two stars. star A and star B, and nothing more, i.e. zero "third light". In our spectroscopic observing, we took care to inspect images from the acquisition cameras, and noted no stars of any significance within the range $1-2''$ of Kepler-64; 2MASS images support this, also. Because poor weather thwarted an attempt at adaptive optics imaging of the environs of Kepler-64, we were unable to inspect within the $\sim 1''$ seeing limit. In general, however, imaging can never prove there is zero third light, because any system could be a hierarchical triple star.

We investigated the effects of assuming a given third-light fraction, f_C = 0, 0.1, and 0.2, of the total light. For $f_C = 0$ the parameters are $k = r_B/r_A = 0.196$, $a/r_A = 21.6$, and $i = 87.53^\circ$, for $f_C = 0.1$ they are $k = r_B/r_A = 0.201$, $a/r_A = 22.08$, and $i = 87.59^\circ$,

and for $f_C = 0.2$ the parameters are $k = r_B/r_A = 0.227$, $a/r_A = 23.56$, and $i = 87.60°$. Thus, compared to the nominal $f_C = 0$ solution, non-zero third light implies larger stellar densities and a larger star B relative to star A. As pointed out by Schwamb et al. (2012), submitted simultaneously with our results, there indeed is a "third light" contamination to the light curve of Kepler-64 in the form of another binary system $0.7''$ away, with a flux contribution of $\sim 10\%$ in the *Kepler* bandpass. Thus, throughout the paper we use the solution for $f_C = 0.1$, listed in Table 2.2.

To estimate eclipse time variations, ETVs (Figure 2.6), we empirically determine the best-fitting center time of each primary eclipse individually by minimizing χ^2, while adjusting only the center time of the model curve. The model is the Mandel & Agol (2002) curve that best-fits the ensemble of primary eclipses, although simpler, non-physical models such as Gaussians or U-shaped curves produce very similar ETVs. We evaluated the statistical significance of the measured ETVs by simulation of model eclipses superposed on the detrended Kepler Light curve. We fit the simulated eclipses to produce simulated ETVs, which we found to have slightly smaller amplitude than the actual ETVs. We conclude that the measured ETVs may have a contribution from the mass of the gas-giant planet but are essentially consistent with noise (Figure 2.6). Also, we simulated ETVs for our best-fit model (Section 2.6) for tertiary masses of 1, 5 and 50 M_J and compared them to the measured values; the latter fall between those for 1 and 5 M_J, securing the planetary nature of the circumbinary body.

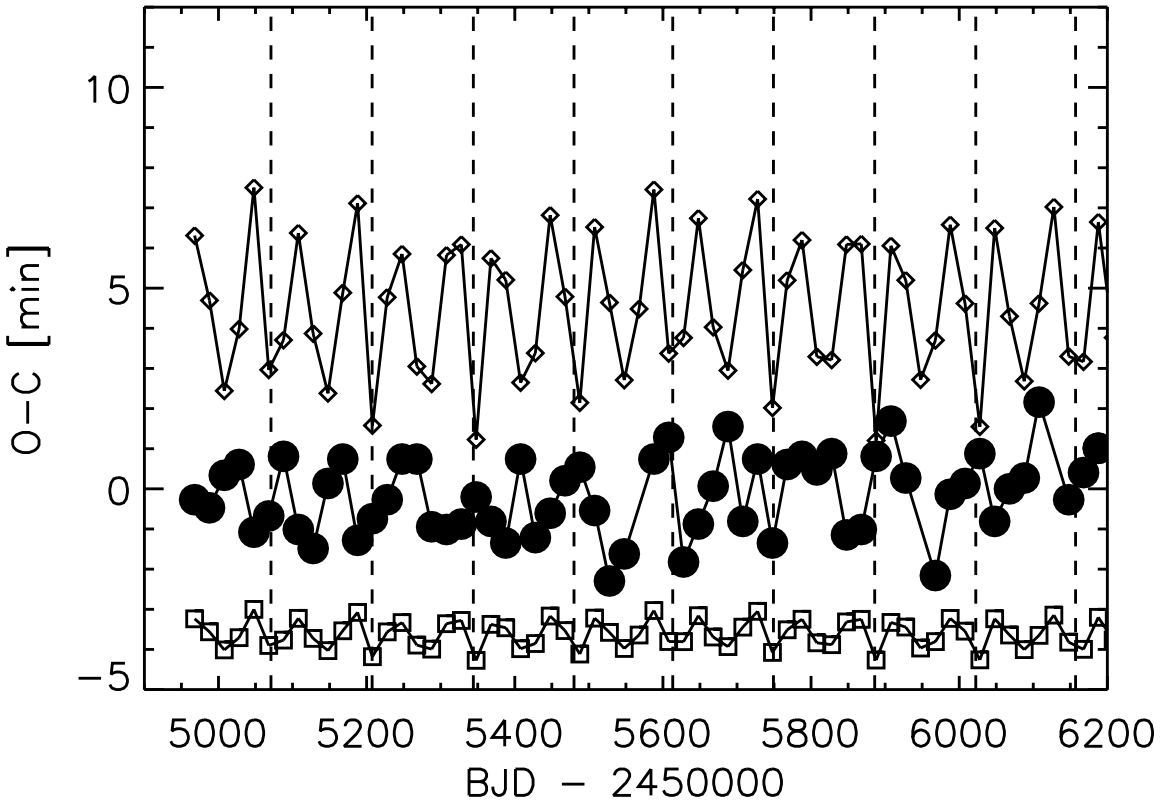

Figure 2.6 Eclipse timing variations of the primary eclipses of Kepler-64 (filled circles). The observed times of each primary eclipse minus the calculated times for a linear ephemeris are shown versus time (an "O-C" diagram). The nine planetary transit events are indicated by vertical dashed lines. A single primary eclipse is missing from the sequence at BJD = 2455567.8 and another, at BJD = 2455947.8, is incomplete. For comparison, two simulated "O-C" variations are also shown, one for a 1 $M_{\rm J}$ (squares) and the other for a 5 $M_{\rm J}$ (diamonds) respectively, and shifted vertically for clarity. Evidently, the circumbinary body's mass is less than 5 $M_{\rm J}$.

2.4.2 Spectral analysis

The SOPHIE spectra of Kepler-64 without background pollution were co-added for spectral analysis. The Hα and Hβ lines were used to determine the effective temperature $T_{\rm eff} = 6200 \pm 150$ K. This estimate was made on each line independently in order to check the consistency of the results. The spectrum lacks prominent spectral features due to its broad lines combined with the low signal-to-noise ratio. This prevents us from carrying out a detailed spectroscopic analysis. We could not derive accurate estimates of the surface gravity from the Mg I triplet and the Na I doublet. The estimation from these lines is $\log g \simeq 4.0 \pm 0.2$; it is a typical value for main sequence and subgiant stars in that $T_{\rm eff}$ range. We do not find any evidence of Lithium in the spectrum nor any sign of chromospheric activity in the Ca II H and K lines, but the Hα core shows some variable emission features. From the width of the CCF we derived $v \sin i_* = 31 \pm 2\,{\rm km\,s^{-1}}$ and [Fe/H] $\simeq -0.15$.

Using these values of $T_{\rm eff}$, $\log g$, and [Fe/H], we estimated the mass and radius of the star by comparison with a grid of STAREVOL stellar evolution models (A. Palacios, priv. com.; Lagarde et al. 2012). We generated a series of Gaussian random realizations of $T_{\rm eff}$, [Fe/H] and $\log g$, and for each realization we determined the best evolutionary track using a χ^2 minimization on these three parameters. We found $M_\star = 1.23 \pm 0.20\,{\rm M}_\odot$, $R_\star = 1.70 \pm 0.25\,{\rm R}_\odot$, and an isochronal age of $2.6^{+3.6}_{-0.3}$ Gyr.

2.4.3 Orbital solution of the binaries

For each of the targets, the APO and SOPHIE radial velocities were fit simultaneously with a Keplerian model. The fits are mainly constrained by the SOPHIE data, which are more numerous and accurate. The APO radial velocities are much less accurate, but agree with the orbital solution derived from the SOPHIE data.

In addition to the measured radial velocities, the fits take into account the three constraints derived from the Kepler photometry: specifically the orbital period P, and the mid-times of transit and occultation, T_t and T_o. The latter parameters strongly constrain $e(\cos\omega)/\sqrt{1-e^2}$ (Section 2.4.1). The radial velocities confirm the orbital eccentricities and allow e and ω to be measured individually. In comparison to the radial velocity uncertainties, the uncertainties in the three parameters derived from photometry have negligible effects on the final uncertainties of the derived orbit parameters.

The fits to the radial velocities were made using the Levenberg-Marquardt method, and the confidence intervals around the best solutions were determined both from χ^2 variations and Monte Carlo simulations. The histograms of the obtained parameters have a single peak and nice Gaussian-like appearance. The derived values and uncertainties are reported in Table 2.2; the best fits are over-plotted with the data in Fig. 2.7.

The semi-amplitude of the radial velocity variations of Kepler-64 is $K = 19.76 \pm 0.73$ km s^{-1}. This is $1.9\,\sigma$ larger than the K-value we obtained by assuming only one component in the SOPHIE CCF instead of two (see above in Section 2.4.2). This gives an order of

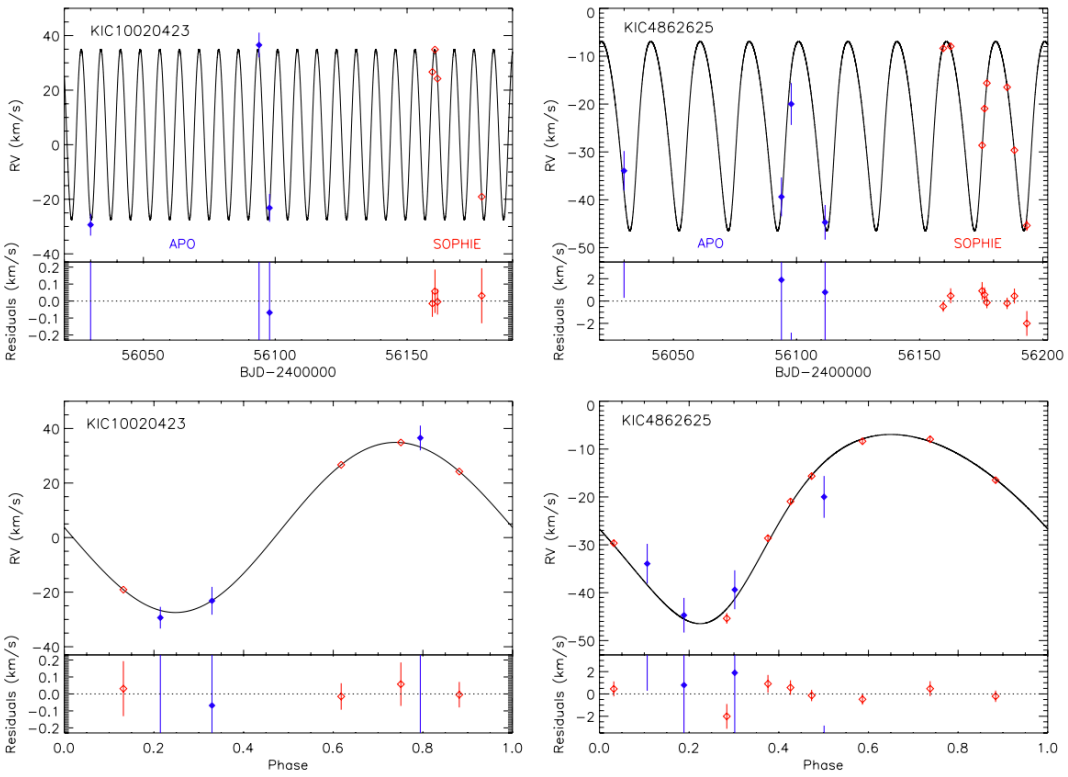

Figure 2.7 Radial velocity measurements of KIC 10020423 (Kepler-47, upper and lower left) and Kepler-64 (upper and lower right) with 1-σ error bars as a function of time (upper) or orbital phase (lower) together with their Keplerian fit and residuals of the fit. The data are from APO (blue, filled diamonds) and SOPHIE (red, empty diamonds).

magnitude of the small effect induced by the blend. Our result is smaller but agrees at $1.9\,\sigma$ with the K-value reported by Schwamb et al. (2012). With an adopted primary mass $m_A = 1.47 \pm 0.08\,\mathrm{M}_\odot$, this translates in a secondary mass of $m_B = 0.37 \pm 0.035\ \mathrm{M}_\odot$. Because Kepler-64 is single-lined spectroscopic binary, star B's mass depends on star A's and their uncertainties are similarly coupled. For Kepler-64 the dispersion of the residuals of the fits are $500\,\mathrm{m\,s^{-1}}$ and $4.3\,\mathrm{km\,s^{-1}}$ for the SOPHIE and APO data, respectively. The dispersion is similar or even smaller than the expected uncertainties on the measured radial velocities. Uncertainties on the SOPHIE radial velocities might be slightly overestimated. We did not reduce them however in order to be conservative. We cannot detect any significant drift in addition to the reflex motion due to the binaries. For Kepler-64 we estimate an upper limit $\pm 10\,\mathrm{km\,s^{-1}\,yr^{-1}}$ for any additional drift.

Our derived parameters for Kepler-47 agree with those derived by Orosz et al. (2012). The semi-amplitude of the radial velocity variations of Kepler-47 is $K = 31.18 \pm 0.12$ $\mathrm{km\,s^{-1}}$. With an adopted primary mass from Orosz et al. (2012), $m_A = 1.04 \pm 0.06\,\mathrm{M}_\odot$, this translates in a secondary mass of $m_B = 0.357 \pm 0.013\,\mathrm{M}_\odot$. Because there are so few RV measurements for Kepler-47, their dispersion is less than the expected measurement uncertainty. For Kepler-47 the dispersion of the residuals of the fits are $25\,\mathrm{m\,s^{-1}}$ and $2.6\,\mathrm{km\,s^{-1}}$ for SOPHIE and APO data, respectively.

2.4.4 Doppler Boosting

The oscillating radial velocity of the primary star of Kepler-64 is apparent in the Kepler photometry. Due to Doppler boosting, when the star is moving toward the Earth, its observed flux increases and when the star is moving away, its observed flux decreases. Figure 2.8 illustrates the modulation in observed flux as a function of the orbital phase of the EB star. To reduce the effect of the rotational modulation on the light curve, we used the mean flux level estimated at each point from the sin wave fit at each point (Section 2.2.1). We grouped the results in 100 uniformly spaced bins in orbital phase. Hence, each point in Figure 2.8 represents the median of ~ 350 Kepler measurements. With an RMS of 222 ppm per original Kepler observation, each median would have a formal uncertainty $\sqrt{350}$ less, or 12 ppm if there were no trends in the light curve. However, with the trends, the observed RMS deviation of the medians with respect to the best-fitting boosting curve is 19 ppm.

Due to Doppler boosting, the ratio of observed flux F_λ to emitted flux $F_{0,\lambda}$ is

$$\frac{F_\lambda}{F_{0,\lambda}} = 1 - B\frac{v_r}{c}, \tag{2.1}$$

where v_r is the stellar radial velocity, c is the speed of light, and the Doppler boosting factor $B = 5 + dlnF_\lambda/dln\lambda$ (Bloemen et al. 2010; Loeb & Gaudi 2003). For a T=6150 K blackbody approximation to the star A's spectrum, and a monochromatic approximation to the Kepler bandpass of $\lambda = 600$ nm, the boosting factor $B_{BB} = 3.99$ (Loeb & Gaudi 2003, Eqs. 2 and 3). At a finer level of approximation, using a template spectrum for an F8

IV star (Pickles 1998) and the Kepler bandpass, we estimate a photon weighted bandpass-integrated boosting factor $B_{F8IV} = 3.73$ (Bloemen et al. 2010, Eq. 3). Both estimates neglect reddening, but its effect is very small for interstellar reddening typical of Kepler stars (Bloemen et al. 2010). Figure 2.8 compares the Doppler boosting effect estimated with $B = B_{F8IV}$, to the Kepler photometry of Kepler-64. The boosting factor that best fits the Kepler photometry and the spectroscopic radial velocity curve is $B = 3.46 \pm 0.065$, i.e. or $93 \pm 1.7\%$ of the analytic estimate with $B = B_{F8IV}$. The boosted flux from star B is out of phase with that of star A, but for simplicity of this analysis we have neglected the tiny contribution from star B.

The capability to measure the radial velocity of an EB star using Kepler data alone could be useful and convenient. In principle, CB systems could be "solved" without spectroscopically determined radial velocities. The phase difference of the stellar eclipses constrains well the quantity $e\cos\omega/\sqrt{1-e^2}$; so the eccentricity e and the longitude of periastron, ω, are constrained by the Kepler photometry. Also, the ratio of the difference in durations (secondary eclipse minus primary eclipse) to the sum of the two durations equals $e\sin\omega$, to a good approximation when the orbital inclination is $\sim 90^\circ$. With Doppler boosting, the Kepler photometry provides the equivalent of a single-lined spectroscopic binary: the radial velocity of the brighter star as a function of orbital phase. The latter also constrains e and ω and the phase of periastron passage, along with a measure of the radial velocity semi-amplitude. For stars of similar brightness, the Doppler boosting effects of the two stars will tend to cancel. Of course, the traditional light-curve analysis of the eclipses provides an

estimate of the relative brightnesses of the two stars in an EB. For those eclipsing binaries with one star much brighter than the other, and if that brighter star is photometrically stable or at least predictable as in the case of Kepler-64's rotational modulation, Doppler boosting curves from Kepler photometry may provide radial velocities adequate for estimating the mass function of the system, and other parameters of the EB.

In this work, we have demonstrated that the stellar radial velocities can be measured either with a spectrometer or a photometer. We give priority to the spectroscopic technique because of its well-calibrated heritage. For comparison we measured $k_1 = 16.7 \pm 0.5$ and $\omega = 222^\circ \pm 2^\circ$ from Doppler boosting in the Kepler light curve. We estimated the maximum-likelihood values of k_1 and ω from all of the photometry. However, because correlations are apparent in the residuals of the Doppler boosting curve, induced by the 2.63-day averaging window during detrending, we estimated the uncertainties of k_1 and ω from subsets of points selected to be independent from each other, in steps of phase equal to 2.63 d / 20 d. The photometrically-determined value of ω is consistent with that determined from shifts of spectral lines, $\omega = 220.2^\circ \pm 3^\circ$. Formally, the photometrically-determined value for ω is more precisely determined than the spectroscopically-determined value. The value of k_1 is prone to systematic error; it is directly proportional to the boost factor B estimated from the overlap integral of the stellar spectrum and the Kepler bandpass. The systemic velocity γ is indeterminate from Doppler boosting.

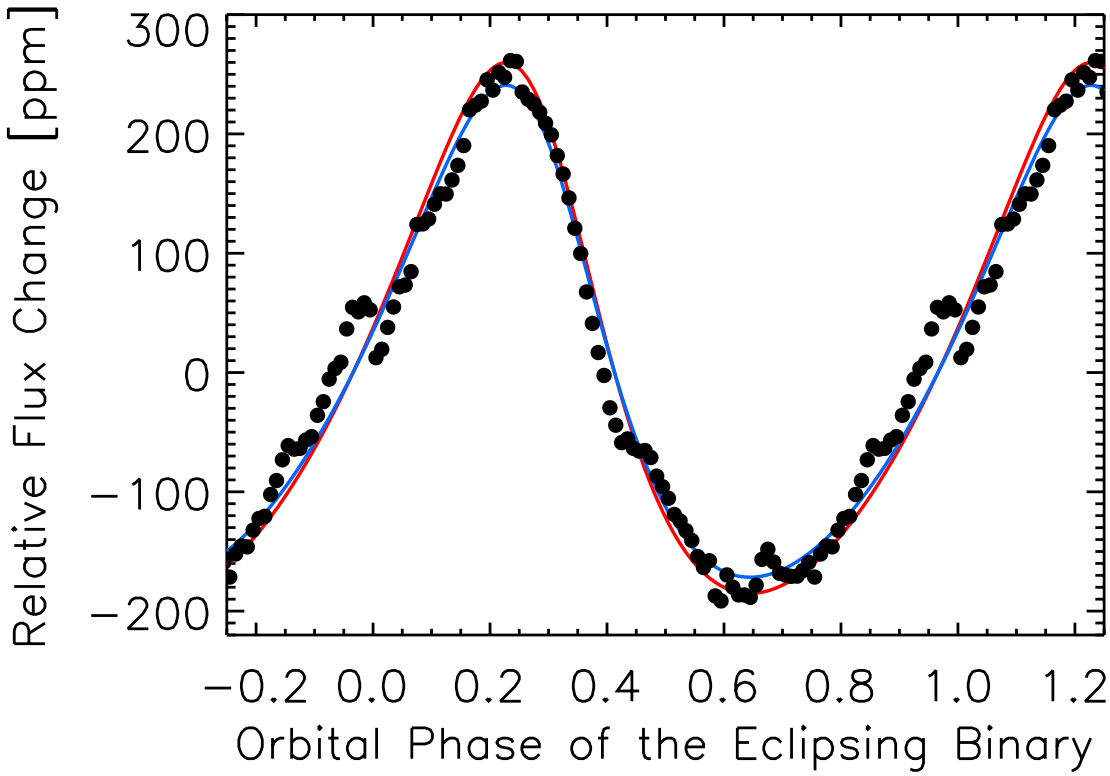

Figure 2.8 Doppler boosting of Kepler-64. The relative, normalized flux change (see text) is plotted with respect to the EB's orbital phase. The data binned in 0.01 intervals of phase (filled circles) approximately match the flux change estimated from Doppler boosting (red curve) based upon the spectrum of the primary star and its spectroscopically-determined radial velocity curve. The amplitude of the best-fitting curve (blue curve) is $93 \pm 1.7\%$ that of the estimate (red).

2.4.5 Stellar Rotation and Star Spots

From the broadening of the spectral lines and the period of amplitude modulations in the light curve, we infer rotation of star A and determine its radius,

$$R_A = \frac{p_{rot} v \sin i_*}{2\pi\phi}, \tag{2.2}$$

where ϕ is a factor of order unity that would account for differential rotation and any systematic errors in $v \sin i_*$, such as $\sin i_* < 1$. With $v \sin i_* = 31 \pm 2\,\mathrm{km\,s^{-1}}$, $\mathrm{p_{rot}} = 2.6382 \pm 0.0037$ d, and $\phi = 1$ the stellar radius $R_A = 1.62 \pm 0.1 R_\odot$, in agreement with the estimates from the spectral analysis (Section 2.4.2) and the photodynamical model (Section 2.6). With R_A determined from rotation, the density of star A implied from the light curve and the mass function from the radial velocity semiamplitude, we derive a mass $M_A = 1.2 \pm 0.2 M_\odot$, again in agreement with estimates from the other two methods. We also estimated M_A using the predicted velocities of the primary and the planet during the nine transits from the best-fit simulations. Each of the nine events is scaled for the respective velocities, such that they have approximately the same width. All nine are then fit together. The derived parameters of the primary star agree with the above mentioned values within their uncertainties. Because $M \propto R^3$, the fractional uncertainty in stellar mass is three times larger than the stellar radius' fractional uncertainty, which is dominated by the uncertainty in $v \sin i_*$ and any bias implicit in ϕ.

A curious situation is possible with Kepler-64. Star A's peak orbital velocity transverse to the line of sight is $\sim$19 km s^{-1} and its rotational velocity is 31 km s^{-1} (Section 2.4.2).

Assuming that star A's rotation is prograde with respect to the orbital motions of star B and the planet, and the axis is in the plane of the sky, i.e. sin i = 1, and that the transit is a central one, the transverse velocity of a star spot (or plage) could briefly match that of the planet ($\sim$46 km s^{-1})! Planetary transits could exhibit asymmetric shapes due to the nearly matched transverse speeds. Kepler-64's transit events 1, 3, and 5 in particular appear asymmetric, with egress being more abrupt than ingress. We are unsure whether the asymmetry is astrophysical or an artifact of the detrending. Because they are grazing, the primary eclipses of Kepler-64 may not exhibit similar asymmetries if spots (or plage) are not prevalent near the pole of star A, and in any case the projected rotational speeds will be small at the star's poles. Silva (2003, 2008) and Nutzman, Fabrycky, & Fortney (2011) have analyzed star-spot induced asymmetries in transit light curves but did not explicitly consider the possibility of a star spot over-taking a planet. More typically, e.g. for a 3-day period planet transiting a solar-type star rotating every 30 days, the transverse velocity ratio (planet/star) is $\sim$100. Gravity darkening is another mechanism for which very rapid stellar rotation can induce subtle asymmetries in transit light curves (e.g. Barnes, Linscott, and Shporer 2011).

2.5 Diagnosing a System

Initial diagnosis of a single transiting planet that orbits a stellar binary can be challenging, particularly if the orbital period is long and the planet transits only one star. There are many

system parameters and potentially only a few observational constraints. In some cases the existing data will not fully constrain the system. Given this potential complexity, it is useful to understand the sequence of analysis steps that build understanding of a newly discovered system. With this in mind, we describe the clues we used to diagnose the Kepler-64 system.

First, we worried that Kepler-64 could be an astrophysical false positive. The aperiodicity of the nine planetary transits disproves the hypothesis of a background eclipsing binary mimicking a transiting CB planet. Superficially, the false-positive of a dilute EB mimicking planetary transits of a single star (Brown 2003) has an analogy in CB planets, namely that a dilute eclipsing triple star in proximity to an EB star could in principle mimic some of the characteristics of a transiting CB planet. First, however, the chance proximity on the sky of a double star and a triple star will be much rarer than that of a single star and a double star (Lissauer et al. 2012). Second, while one could contrive a dilute triple star to mimic the aperiodic centers of a few transit-like events, the durations in general would not match also, because for a CB planet, the transit durations depend critically on the characteristics of the EB (Eq. 2.4). We conclude that a third body orbits the EB star Kepler-64.

We next analyzed the stellar binary, which has the best observational constraints. The Kepler light curve folded on the 20 day period of the stellar binary (Figure 2.5) has a primary eclipse that is 1.3% deep and a secondary eclipse that is 0.1% deep. Primary eclipses are more V-shaped than U-shaped, suggesting that a smaller secondary grazes a larger primary. Secondary eclipses have a flat bottom with gradual ingress and egress,

suggesting that the limb of the primary fully occults the secondary. The phase difference between primary and secondary eclipses indicates an orbit with significant eccentricity.

Next we examine high-resolution spectra of the system. Spectral features are roughly similar to the Sun, except that the lines are shallow and broad. Cross-correlation with a template yields radial velocity shifts consistent with the light curve period of 20 days. Line widths imply $v \sin i_* = 31$ km s^{-1}, which is typical for spectral types slightly earlier than the Sun. As expected, lines of the low-mass secondary are not detected in the optical spectra.

Next we examine the nine planetary transits that exist in publicly available Kepler data. First we checked the data quality flags to verify that all data are valid during the transits. Using the PyKE software[7] with custom apertures to analyze Kepler target Pixel files, we confirmed that the nine transit events come from the central target pixels. We measured no significant centroid shifts during the transits, which rules out certain astrophysical blending scenarios. We measured transit start and end times by fitting U-shaped functions. We then calculated transit midpoint times and durations.

The cadence and duration of the transits suggest that all involve the primary star. The cadence of the planetary transits yields an apparent orbital period of approximately 136 days. The time differences between successive transits is 136.6, 136.7, 135.9, 133.2, 135.9, 136.7, 136.4 and 134.7 days. Such regularity is not anticipated for a circumbinary system, where a single object transits or eclipses a "moving target" (Orosz et al. 2012). The regular cadence of transits is not caused by simple commensurability, given the 20 and 136 day

[7] http://keplergo.arc.nasa.gov/PyKE.shtml

periods in the system.

We use the durations of the transits to constrain the parameters of the stellar binary. Transit duration depends on chord length and on transverse velocity of the stellar primary relative to the circumbinary object (Schneider & Chevreton (1990). During transits, transverse velocity of the planet is always fairly similar, but transverse velocity of the occulted primary (dependent of the mass ratio of the two stars) changes direction and amplitude throughout its orbit. The amplitude of the transverse velocity of the primary decreases to a minimum at orbital turning points. For eccentric stellar binaries, amplitude also decreases with increasing binary separation. Finally, transit durations are longer when the primary is in the portion of its orbit where transverse velocity of the primary and planet are aligned, and shorter when the two velocities have opposite signs.

With these factors in mind, we now interpret the nine observed transits, ordered by increasing duration. Transit 2 has the shortest duration because the transverse velocities are oppositely directed and the primary is far from a turning point. Transit 1 has a slightly longer duration because the primary is slowing as it approaches a turning point. Transit 3 is near the other turning point, where binary separation is larger, further reducing relative velocity. Transit 4 has a relatively long duration because the transverse velocities are now aligned, though the primary is near the turning point where the binary separation is large. Transit 5 has a very long duration because the velocities are still aligned and the primary is near the turning point where the binary separation is small. Transit 9 has a very long duration because the star and the planet travel “side by side”. Because transit durations are

shortest near primary eclipse, the planetary orbit must be prograde relative to the stellar binary.

To quantify constraints provided by observed transit times and durations, we calculated the locations of all bodies in the system as a function of time. Figure 2.9 and 2.10 are schematic scale drawings of the EB system. Figure 2.10 illustrates the sizes of the three objects (star A, star B, and the planet) relative to each other and to the barycentric orbit of star A, which stretches only a few stellar radii across. The schematics also illustrate the positions of the stars at the epochs of each of the nine planetary transit events. Because we have approximated the transit chord as the diameter of star A for all nine planetary transit events, we have not illustrated the orbit of the planet in the schematic diagrams. The primary has a very similar projected position during transits 1 and 5 and, half a binary period later, during transits 4 and 8. Because of this near coincidence, the time difference between transit 1 and 5 is almost exactly four times the 135.59 day orbital period of the planet.

Next, we inspect event 4, also a relatively long duration event. At the phase of event 4, the primary star is near the opposite turning point of its orbit from events 1 and 5. Note event 2 is near primary eclipse, when the two star's relative motions are relatively fast, and the primary star is traveling right to left, i.e. in the opposite direction to the planet, if in our scenario the planet is traveling in a prograde orbit (left to right in this model). Again, event 2 is deeper than secondary eclipse, and event 2's shape is not a square wave, so we consider event 2 is again a transit of the planet across the primary star.

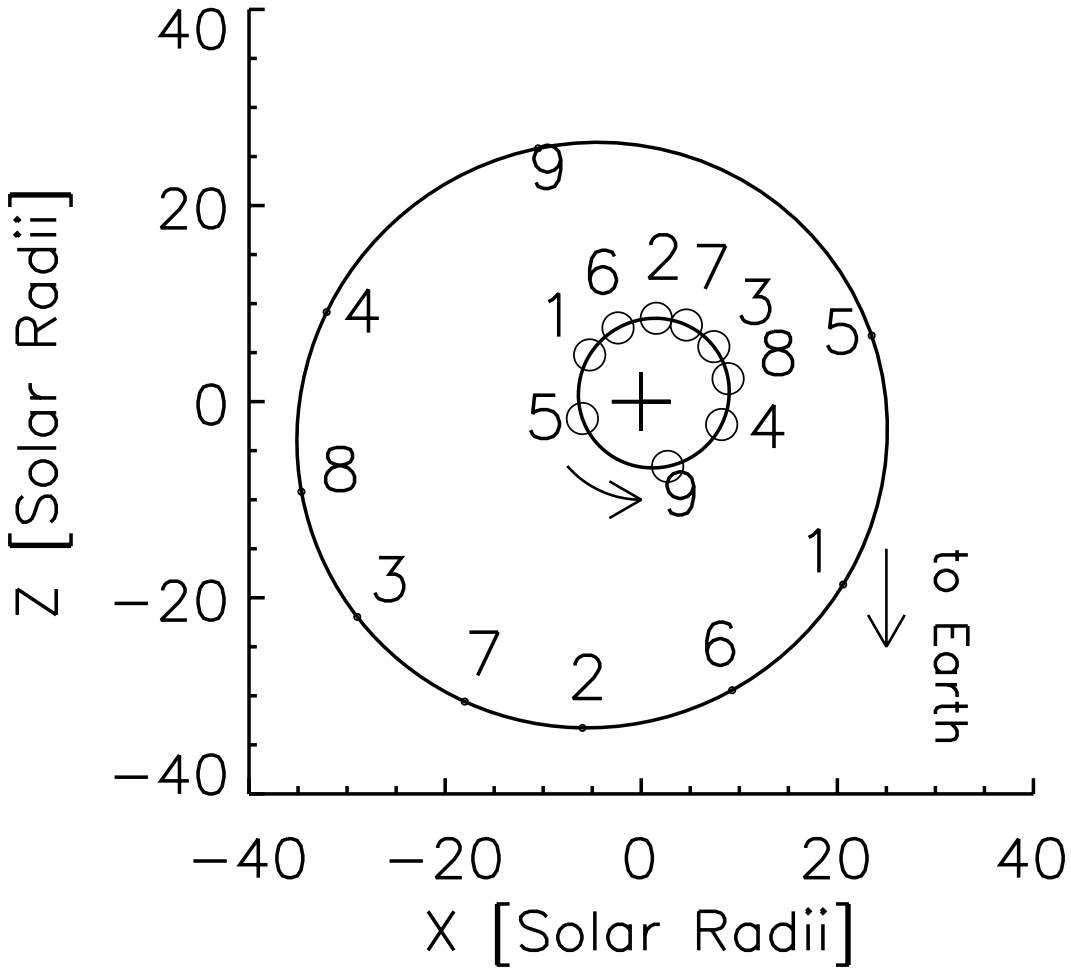

Figure 2.9 Scaled view of the binary system of Kepler-64 viewed perpendicular the orbital plane. The inner ellipse shows motion of the primary, while the outer ellipse shows the secondary. The two stars orbit the barycenter of the system (cross symbol) in a counter-clockwise direction. Numbers along the orbits indicate the configuration of the binary system at the times of the planetary transits. At these times, the planet and the primary star align along the y-axis. The planetary orbit is outside the scale of the figure. The diagram is to scale.

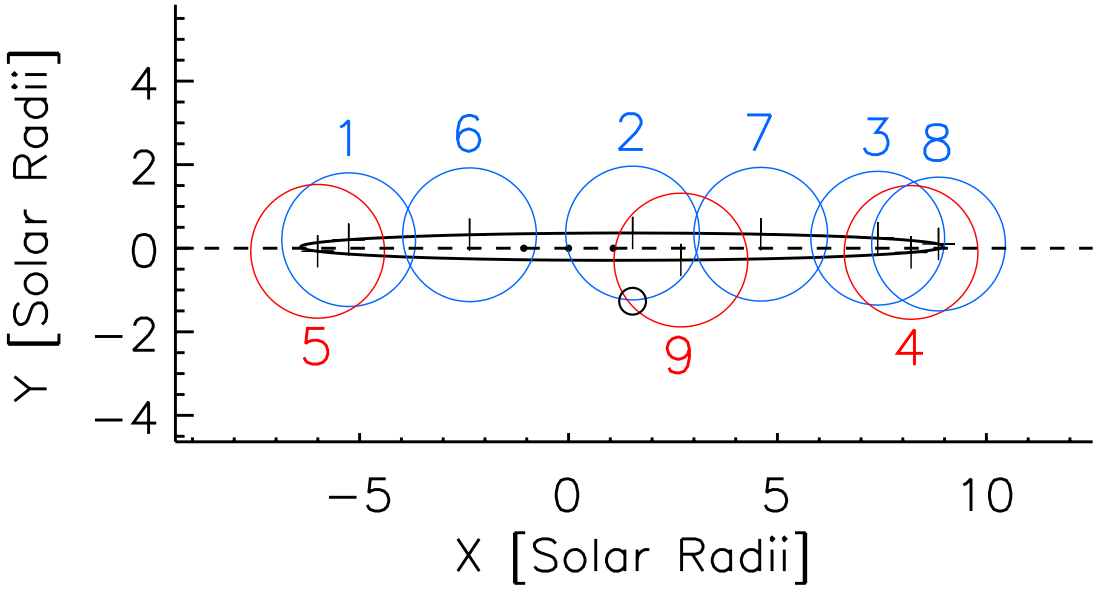

Figure 2.10 Schematic scale diagram of Kepler-64. The diagram is to scale, with solar radii indicated on the axes. The positions of star A in its orbit (large circles) are plotted at the times of the nine planetary transits (labeled, large circles centered on black + symbols). Red color indicates the position of the primary star on the near side of its orbit and blue color – on the far side. Star B is shown to scale (small circle, arbitrarily positioned below star A at event 2). The planet also is shown to scale (smallest circles); the outer two corresponding to positions −0.25-d and +0.25-d with respect to the center position, which, has been arbitrarily centered at the origin.

Transverse velocity of the primary is a function of true anomaly, argument of periastron, and eccentricity. Using the nomenclature of Hilditch (2001), transverse velocity V_x is given by

$$V_x = -(\frac{M_2}{M_{bin}})(\frac{2\pi G M_{bin}}{P_{bin}})^{1/3}\frac{(e\sin\omega+\sin(\theta+\omega))}{(1-e^2)^{1/2}}, \tag{2.3}$$

where $M_{bin} = M_{\rm pri} + M_{\rm sec}$, θ is true anomaly, ω is the argument of pericenter and e is the eccentricity of the binary star.

Using the formalism of Schneider & Chevreton (1990), and assuming a circular orbit for the planet, we obtain the following expression for transit duration $t_{\rm dur}$:

$$t_{dur} = \frac{AB}{1+ACx} \tag{2.4}$$

where

$$\begin{aligned} A &= (M_{bin})^{-1/3} \\ B &= 2R_c(\frac{P_p}{2\pi G})^{1/3} \\ C &= -f(m)^{1/3}(\frac{P_p}{P_{bin}})^{1/3}(1-e^2)^{-1/2} \\ x &= (e\sin\omega+\sin(\theta+\omega)) \end{aligned} \tag{2.5}$$

In Eq. 2.4, we use the mass function $f(m)$ obtained from radial velocities to substitute secondary mass (M_2) for binary mass ($M_{\rm bin}$); x is calculated from the known θ of the binary star at the time of each planetary transit and t_{dur} is measured for each of the nine events. The mean period of the planet (P_p) is known from the cadence of transit times. Assuming

transit chord ($R_c = R_{\rm pri} + R_{planet}$) is the same for every transit, we fit for the coefficients A and B (C is known to the precision of P_p). The inferred value of parameter B in Eq. 3.1 constrains stellar radius. Long duration transits will deviate slightly from Eq. 3.1, if velocity of the stellar primary changes significantly during the transit. We caution that very small changes in observed transit durations can have significant effects on parameters derived from A and B.

To validate Eq. 3.1, we fitted observed transit durations for Kepler-47b, using transit parameters in Orosz et al. (2012). The fit shown in Figure 2.11 yields $M_{bin} = 1.35\ M_{\odot}$and $R_{\rm pri} = 0.87\ R_{\odot}$, approximately equal to the $1.4 \pm 0.05\ M_{\odot}$ and $0.96 \pm 0.017\ R_{\odot}$ deduced by Orosz et al. (2012). Figure 2.12 shows an analogous fit for Kepler-64b. We obtain an $M_{bin} = 1.74\ M_{\odot}$ and $R_{\rm pri} = 1.7\ R_{\odot}$. The analytic curve indicates that future transits may be as long as 30 hours! To assess uncertainties, we created simulated observations for a mock system like Kepler-64 (Model 1 in Section 2.6). We integrated the mock system for 9 planetary orbits, using a time-step of 14.4 min, to calculate durations and times of the planetary transits and then fit for A and B in Eq. 3.1. As with Kepler-47b, the inferred binary mass of $1.76\ M_{\odot}$ is $\sim 5\%$ smaller than the expected value of $1.85\ M_{\odot}$. The chord length calculated from A is $1.68\ R_{\odot}$, compared to the input value of $1.7\ R_{\odot}$. The fits to the planetary transit durations using the analytic functions provide a good starting point for the more refined fits presented in Section 2.6.

In the existing data, depths of the nine observed transits appear to change with time. Perhaps this is simply an artifact of our detrending procedure. Alternatively, star spots that

perturb the light curve may also affect apparent transit depth. Finally, changes in transit depth could be a manifestation of a planetary orbit with an inclination different than 90 degrees.

Numerically integrating an inclined planetary orbit forward in time, the transits fade away, cease for a period, and then return after a large number of orbits. The larger the inclination, the faster the evolution. Given that we have observed 9 transits so far, we assume that the chord lengths, transit depths, and planetary inclination are constant.

For completeness, we note that the observed dependence of the durations of the nine transits on the phase of the binary rule out a retrograde orbit for the planet. Such an orbit should exhibit an opposite trend in a duration versus phase diagram, namely short durations near secondary eclipse and longer ones close to primary eclipses.

2.6 Planetary Transits

2.6.1 Methodology

Combined light curve and radial velocity measurements of a circumbinary planet can be characterized by 17 parameters: five orbital elements of the binary (a_{bin}, e_{bin}, ω, Ω, i), six osculating orbital elements of the planet (a_3, e_3, i_3, ω_3, Ω_3, ϕ_0), three masses ($M_{\rm pri}$, $M_{\rm sec}$, m_3), and three radii ($R_{\rm pri}$, $R_{\rm sec}$, r_3). Exhaustively searching a space with 17 dimensions and nonlinear parameters is impractical, so we make simplifying assumptions that allow us

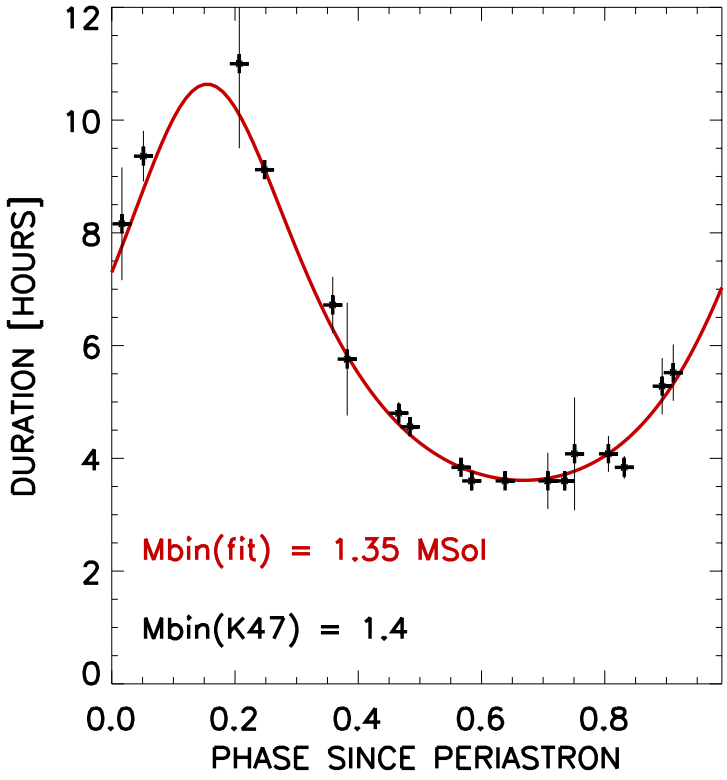

Figure 2.11 Duration versus phase for the Kepler-47b transits. The red curve represents a fit from Eq. 2.4. The analytic expression recovers the parameters of the binary star very well – $M_{bin,calc} = 1.35 M_{\odot}$ vs $1.4 M_{\odot}$ and $R_{prim} = 0.87 R_{\odot}$ vs $0.96 R_{\odot}$ respectively, provided by Orosz et al. 2012.

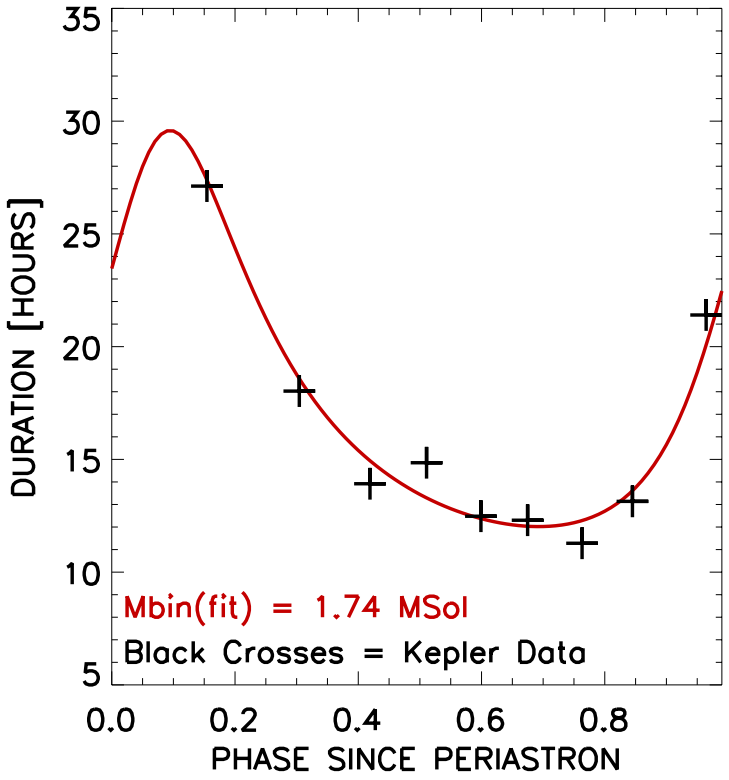

Figure 2.12 Similar to the previous figure but for Kepler-64b. The uncertainties in the measured durations are smaller than the size of the symbols.

to obtain a reasonable solution. As discussed in Section RV, radial velocity measurements yield e, ω, and the stellar mass ratio. The precise Kepler light curve yields the ratio of stellar radii, which depends on derived impact parameters for eclipses that may be grazing. We assume the nine observed transits all occult the primary star, so radius of the secondary star drops out of the system. For simplicity, we assume that the planet has negligible mass and orbits in the plane of the sky ($i_3 = 90$ deg). The former assumption is based on the measured ETVs, discussed in Section ETV and expanded below. The latter relies on the hypothesis that the inclination of the planet should be certainly larger than that of the binary for otherwise it would not be seen in transit.

With these approximations, the four remaining free parameters are $M_{\rm pri}$, a_3, e_3, and ω_3. Finding optimal values for these four parameters still requires a very fine numerical grid. For example, a 1% change in mass of the primary star, or in the semi-major axis of the planet can dramatically change the dynamical evolution of the planet, affecting arrival times of observed transits by hours or even days. Arrival times would also be affected if the planet is massive, rather than a massless test particle.

Transit durations (shown in Table 2.4) have formal uncertainties that do not necessarily account for astrophysical variations in the light curve. To assess how sensitive binary mass is to individual transit durations, we generated and analyzed a set of perturbed observations. We scrambled the nine observed transit durations and added a normally distributed perturbation with a standard deviation of 1 hour (2 long-cadence data points). We then used Eq. 2.4 to evaluate the binary mass, obtaining the results shown in Figure 2.13, where we

plot the normalized distribution of best-fit models as a function of the mass of the binary. The binary mass distribution has 68% of the values in the range 1.4 to 2 $M_{\odot}$. In subsequent analysis, we constrain the binary mass to be in this range.

A simple Keplerian solution cannot reproduce observed planetary transit times because the central potential varies as stars in the binary orbit each other. Instead we use a three-body numerical integrator with hierarchical Jacobian coordinates, as will be further described in Section 2.7. We specify initial conditions (and reference epoch) with respect to the midpoint of the first transit, an arbitrary yet convenient definition. The coordinates of the three bodies are defined with respect to the barycenter of system, which is the barycenter of the stellar binary when planet mass is negligible. We use time-dependent, osculating Keplerian elements to calculate a_3, e_3, i_3, and ω_3 (Doyle et al. (2011)). We use the numerical integrator to compute spatial coordinates for the two stars and the planet. Transits intervals occur when the projected distance between the primary star and planet centers is less than the sum of their radii. Note that parameters cited in this section are instantaneous values for the reference epoch.

First, we used a coarse time step (one third the shortest transit time) to calculate dynamical solutions and corresponding transit midpoint times for a grid of parameter values. The grid step sizes were 0.01 $M_{\odot}$ for $M_{\rm pri}$, 1 $R_{\odot}$ for a_3, and 5 deg for ω_3. Changes of 1 $R_{\odot}$ in a_3 cause significant changes in transit midpoint times. Parameter ranges in the coarse grid were 1.4 to 2.0 $M_{\odot}$ for $M_{\rm pri}$, 0 to 0.2 for e_3, and 0 to 360 deg for ω_3. Next, we used a fine time step (0.01 days) to calculate dynamical solutions for a much finer grid of parameters

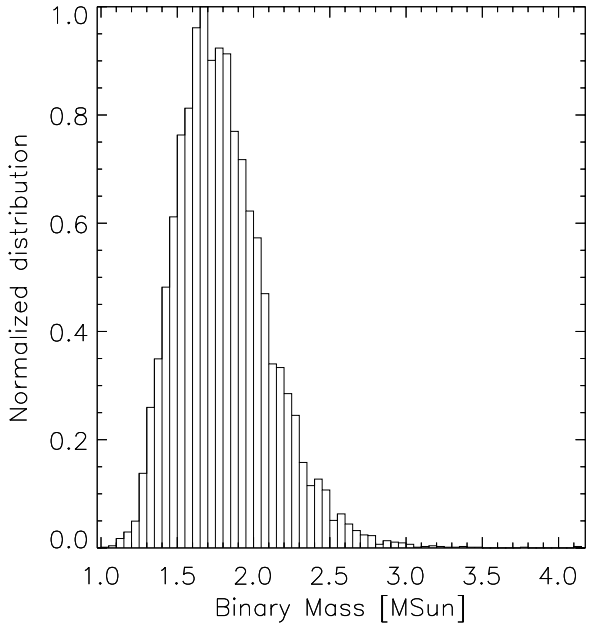

Figure 2.13 Mass of the binary ($M_A + M_B$) derived using the results from the RV measurements and applying Eq. 2.4 to ten thousand iterations of the nine planetary transit durations, scrambled and with added normalized noise with σ = 1 hour. We used this distribution to set the limits of our search space for the primary mass in our dynamical model of Kepler-64.

around the best solutions in the coarse grid. The fine grid includes r_1 as a fifth parameter and calculates transit durations in addition to transit midpoint times. Comparing computed and observed midpoint times and durations for the nine transits yields a set of plausible models.

2.6.2 Results

Even searching in a restricted parameter space, we found multiple solutions that are consistent with the nine planetary transit observations. We adopted a goodness of fit metric that is the root mean square (RMS) of the sum of observed minus calculated (O−C) midpoint times for transits 2 through 9. The midpoint time for transit 1 always has zero residual because it defines the zero point of time in our calculations. Figure 2.14 shows goodness of fit for every dynamical model in the grid that matches observed transit midpoint times to better than a RMS of $\sim$ 10 hours. Each point in the figure represents a unique combination of $M_{\rm pri}$, a_3, e_3, and ω_3. Despite a uniformly sampled grid, the number of solutions better than RMS of $\sim$ 10 hours decreases with increasing $M_{\rm pri}$, suggesting that lower $M_{\rm pri}$ is more likely. We note, however, that even though almost half of all solutions fall within $M_{\rm pri}$between 1.1 $M_\odot$and 1.3 $M_\odot$, most of them have high RMS and are not very likely.

Within the limitations of our grid space search, two solutions stand out from the rest as having an RMS O−C to within 3 hours. The two models, labeled M1 and M2 in Figure 2.14, reproduce the observed planetary transits equivalently well. Further supporting the existence of *a* solution near these two models stems from them having very similar

parameters – both indicate a primary star of $M_{\rm pri} = 1.47 M_{\odot}$ and a planetary orbit with a semi-major axis $a_3 = 0.64$ AU, and $e_3 \sim 0.1$. Combined with observational constraints described in previous sections, this implies $M_{\rm sec} = 0.37 M_{\odot}$, $R_{\rm pri} = 1.7 R_{\odot}$ (consistent with our estimates from the spectra and the stellar rotation), $R_{\rm sec} = 0.34 R_{\odot}$, and $P_3 = 138.5$ days. After global minimization, individual transits are inspected for significant inconsistencies between observed and model light curves. Agreement is very good for the two models, but there are subtle differences – the model transits oscillate around the observed ones to within a few data points. Further examination shows that M1 clearly stands out as M2 consistently under predicts the mid transit times of events 5 through 9 by up to an hour.

Table 2.3 lists the best-fit parameters for model M1; the photodynamical solutions to the planetary transits are shown on Fig. 2.15. The model reproduces well the observed phase-dependance of the durations, with event 2 predicted to be shortest and event 9 – longest. We caution that the nine observed transits are not sufficient to completely rule out any plausible solutions. Other equivalent or even better solutions may exist, given the coarseness of our initial grid search. We were unable to match observations with a circular orbit ($e_3 = 0$), which is not surprising given that orbital elements evolve continuously. An orbit that is initially circular will change with time, especially when the planet is relatively close to the stellar binary (e.g., Kepler-64).

To estimate the uncertainty of the derived $M_{\rm pri}$, we examined the distribution of solutions as a function of $M_{\rm pri}$ that have an RMS of less than 6 hours ($\sim 2\sigma$ above the best-fit value). Nearly half of the solutions shown on Figure 2.14 comply with this merit criteria,

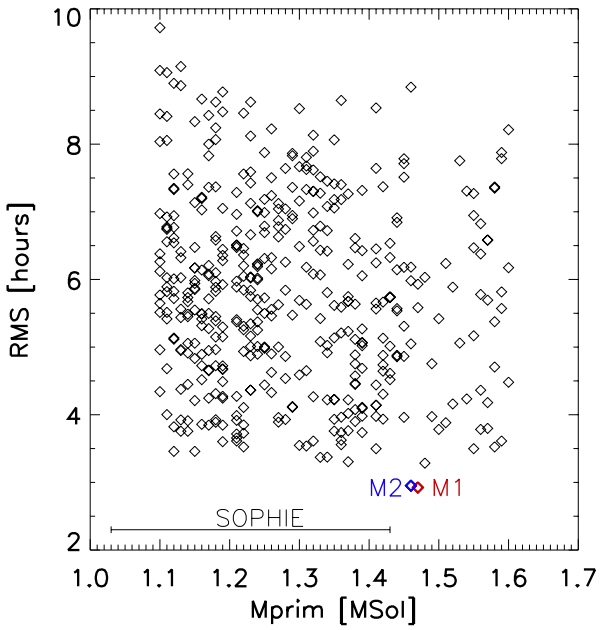

Figure 2.14 Best-fit dynamical models of Kepler-64 predicting the midpoint times of transits 2 through 9 within an RMS of ~ 7 hours. Models with different parameters produce similar solutions, all predicting planetary transits that deviate by only a few data points from the observed values, a small error margin on the orbital scale of the planet. The decrease in the number of "hits" as the mass of the primary increases from 1.1 to 1.6 $M_{\odot}$is not a systematic effect but is in fact real – there are many more good "hits" for smaller M_{prim}.

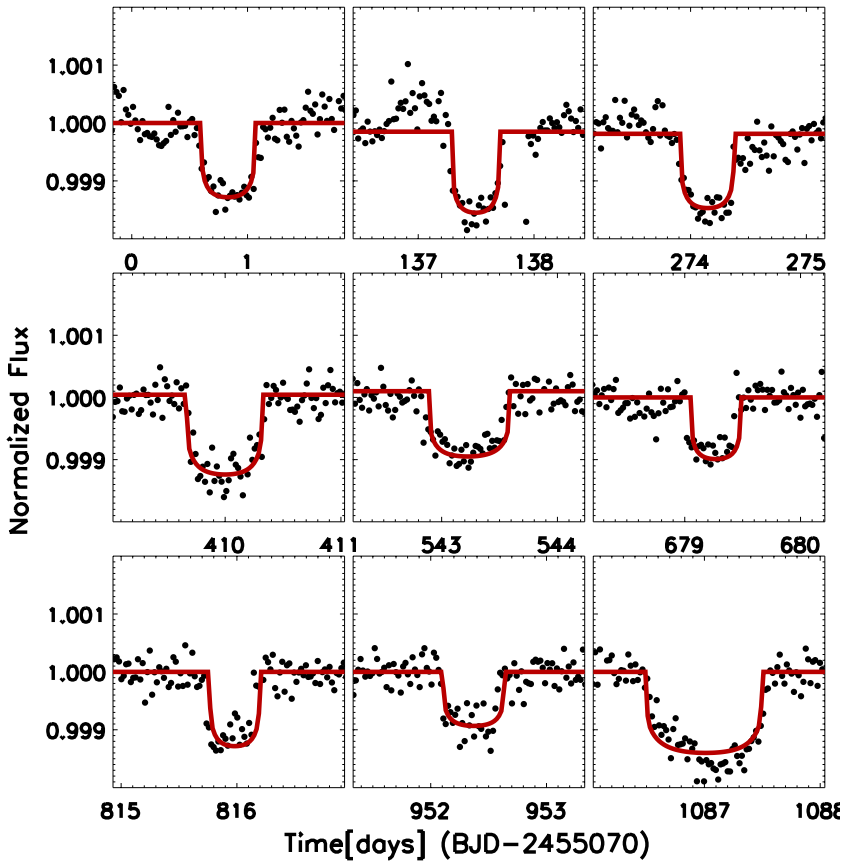

Figure 2.15 The best-fit photodynamical model of Kepler-64 predicting the center times for transits 2 through 9 to within RMS of three hours. The model supports a primary star of $1.47M_{\odot}$ and $1.7R_{\odot}$ radius. All simulated planetary transits fit to within 2 data points of the measured values of both the durations and the mid transit times. Future events will allow us to further constrain the characteristics of the system. The orbital and physical parameters of the system are outlined in Table 2.3.

of which 92 fall within $M_{\rm pri}$ between $1.3M_{\odot}$ and $1.5M_{\odot}$. The distribution is double-peaked with a taller one centered on $M_{\rm pri} \sim 1.15M_{\odot}$ and another, smaller peak near $M_{\rm pri} \sim 1.4M_{\odot}$. The low-mass solutions, however, while producing a good overall RMS, consistently result in larger O$-$C deviations for individual events compared to the higher-mass solutions. Thus, we focus on the $M_{\rm pri} \sim 1.4M_{\odot}$ peak, where half of the solutions fall within a range of $M_{\rm pri}$ between $1.32M_{\odot}$ and $1.48M_{\odot}$ with an average of $1.4M_{\odot}$. Similarly, we constrain the semi-major axis of the planet and the argument of periastron but not the eccentricity of the orbit where the best-fit values were uniformly spread. We report the values in Table 2.3. At the time of submission, we predicted durations of planetary transits that would follow the first five. Transit 9 we predicted to have a very long duration, and indeed it does (nearly 30 hours), allowing us to significantly improve the constraints on the stellar masses. Transits 6, 7, and 8 we predicted to have short durations similar to many other transits, providing only limited additional information about the mass of the binary star.

We also investigated how non-zero planet mass (1 to 10 $M_{\rm J}$) affects transit midpoint time and the precise cadence of stellar eclipses by perturbing Model 1. Using the formalism of Borkovits et al. (2012), we estimate that light travel time effects due to a 10 $M_{\rm J}$ planet would produce timing changes with an amplitude of only a few seconds. On the other hand, dominant three-body dynamical interactions would produce O$-$C variations with an amplitude of $\sim$ 3.5 minutes, which is approximately twice the measured value (Figure 2.6). Thus, the mass of a coplanar planet should not exceed $\sim$ 5 $M_{\rm J}$. Figure 2.16 shows how predicted transit midpoint times change as planet mass increases from 0 to 1.4 $M_{\rm J}$.

A more massive planet tends to arrive earlier for events 4, 5 and 9 and late for 6 and 7, where the deviations are most pronounced for event 9. We tested several other models and found they all show similar behavior, indicating that while Saturn-mass planets and smaller can be safely approximated as test particles for dynamical purposes, a more massive planet would need to be properly accounted for in numerical integrations of Kepler-64.

2.6.3 Search for additional transits

We visually examined the light curve of Kepler-64 for evidence of additional transits. Despite significant variability, there are a few features that are reminiscent of shallow planetary transits. For these features, data flags are normal and centroids have no significant shifts. Some of these extra features occur close in time to the nine main transits, most notably around day 5615 (BJD-2450000) when the dynamical model predicts the planet is near the secondary star, but also near days 5045 and 5069, where the two are distinctly apart. The small size and faintness of the secondary, however, means we do not expect to see a quaternary transit (see Section 2.4.1). Others (near days 5258, 5269, 5298, 5312, 5415; BJD-2450000) cannot be easily associated with the circumbinary planet Kepler-64b.

2.7 Dynamical analysis and orbit stability

We have carried out a dynamical analysis of the Kepler-64 system within the framework of the three-body problem. Such a dynamical system is well known to possibly exhibit

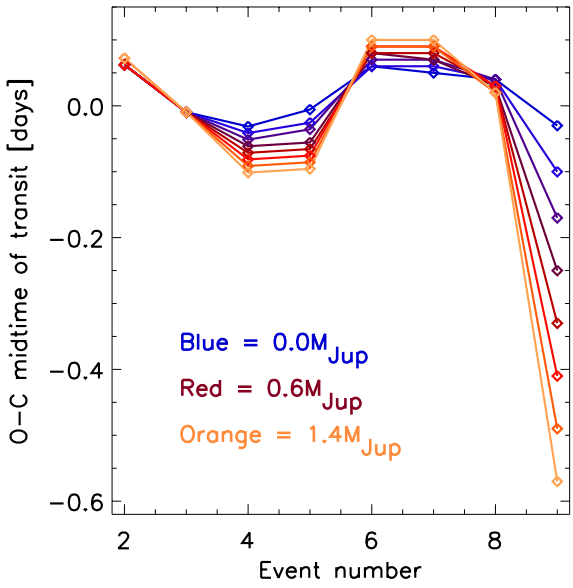

Figure 2.16 The effect of a non-zero planetary mass on the predicted times of transit of Kepler-64. Keeping the best-fit parameters of the circumbinary system constant, an increasingly more massive planet introduces significant deviations relative to the best solutions for a massless planet. While it is unlikely that the mass of the planet is larger than a few $M_{\rm J}$, it adds a significant complication to the best-fit models, again indicating the non-unique nature of the solutions.

complex dynamical behavior. In particular we have carried out a dynamical analysis of the planet around the binary pair in order to detect chaotic regions, often associated with mean-motion resonances (MMRs), in the orbital parameter space of the planet.

We have applied the MEGNO[8] factor (Cincotta & Simó, 2000a,b; Cincotta et al., 2003). This numerical technique is efficient in distinguishing between chaotic and quasi-periodic and has found widespread application within dynamical astronomy and the dynamics of multi-body extrasolar planets (Goździewski et al., 2001, 2008; Hinse et al., 2010).

Chaotic orbits are usually (but not always) attributed to unstable orbits. For a quasi-periodic time evolution of the system the dynamics is regular and characterized by only a few fundamental frequencies often associated with stable orbits. However, in order to be precise, quasi-periodic/stable orbits can only be quoted as stable up to the considered integration time. Knowledge on the subsequent dynamical evolution of the system is still hidden to the experimenter. In this work we have experimented with various integration length and found an integration time scale that is long enough to detect the most important mean-motion resonances close to the osculating orbital elements of the transiting planet Kepler-64b.

For reasons of optimization and execution speed we applied the most recent implementation of the MEGNO technique using Poincaré variables (Goździewski, 2003; Goździewski et al., 2008). In this reference frame the coordinates of each body are expressed in an astrocentric frame with the most massive object at rest and velocities are relative to the systems

[8]Mean Exponential Growth of Nearby Orbits

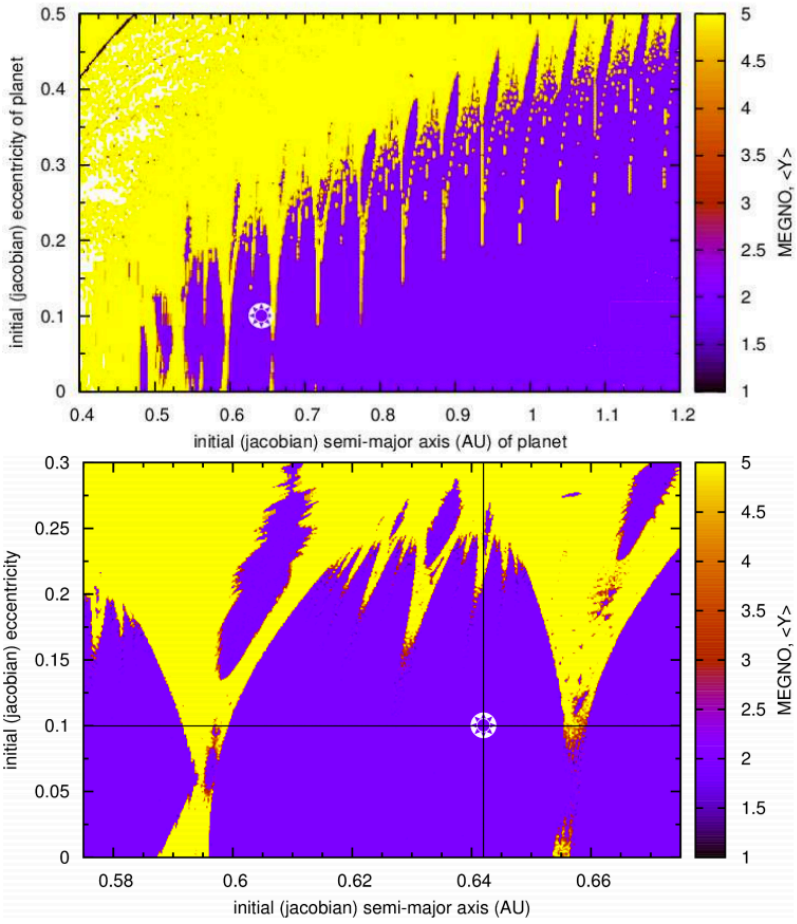

Figure 2.17 Upper panel: MEGNO map of Kepler-64b. The mass of primary and secondary component were set to 1.47 $M_{\odot}$ and 0.37 $M_{\odot}$, respectively. The binary semi-major axis and eccentricity was set to 0.177 AU and 0.2. The planet was treated as a test particle. The cross-hair marks the best-fit osculating elements $(a,e) = (0.64\ \text{AU}, 0.1)$ of the planet. [[The narrow yellow valleys]] indicate the location of mean-motion resonances. Yellow (or light) color denotes chaotic (possibly unstable) orbits and blue (dark) color denotes quasi-periodic orbits with $|\langle Y \rangle - 2.0| \simeq 0.001$. Lower panel: Same as the upper panel but now zooming into a narrower region of (a,e)-space of the planet.

barycenter. We use geometric Jacobian coordinates as our initial conditions where the planets orbital elements are relative to the barycenter of the binary system. The Jacobian cartesian coordinates are then transformed to Poincare elements. The numerical integration of the equations of motion and the corresponding variational equations (Mikkola & Innanen, 1999) are based on the ODEX[9] integration algorithm (Hairer et al., 1993).

To compute MEGNO maps we used the MECHANIC[10] software (Słonina et al., 2012) which utilizes a Message Passing Interface (MPI) based framework that implements massive single serial dynamical problems for parallel execution in a multi-processor computing environment. Usually we allocated 60 CPUs to compute a single dynamical MEGNO map with typical resolution of 500 x 350 initial conditions. Typical integration time of a single orbit covered about 5×10^4 binary orbits ($\simeq$ 2700 years).

When investigating a dynamical system the MEGNO factor (usually denoted as $\langle Y \rangle$) has the following mathematical properties. In general, MEGNO has the parameterization $\langle Y \rangle(t) = \alpha t + \beta$ (see references above). For a quasi-periodic chaotic initial condition, we have $\alpha \simeq 0$ and $\beta \simeq 2.0$ for $t \to \infty$ asymptotically. If the orbit is chaotic, then $\langle Y \rangle \to \lambda t/2$ for $t \to \infty$. Here λ is the maximum Lyapunov exponent of the considered initial condition. In practice, we terminate a given numerical integration of a chaotic orbit when $\langle Y \rangle > 12$. In our MEGNO maps we color code chaotic initial conditions with yellow and quasi-periodic with blue color.

In Fig. 2.17 we show a MEGNO map displaying the dynamics of a planet in semi-major

[9] http://www.unige.ch/math/folks/hairer/
[10] http://git.astri.umk.pl/projects/mechanic.

axis (a) and eccentricity (e) space. The planet was assumed (justified by the planet displaying transit-like signals) to be co-planar with the binary orbit and all planetary orbital angles were set initially to zero. We remind the reader that the shown elements are referred to a Jacobian reference system with the planets semi-major axis being measured relative to the binary barycenter. The secondary binary component was also started with all orbital angles initially set to zero. The mass of the two binary components were set to 1.47 and 0.37 $M_{\odot}$ for the primary and secondary component respectively. Referring to Fig. 2.17 we identify the location of several mean-motion resonances in the system appearing as vertical chaotic columns at constant semi-major axis. The derived orbital elements of the circumbinary planet have $(a,e) = (0.64, 0.1)$ placing the planet in a quasi-periodic region between the 6:1 and 7:1 mean-motion resonance. We show a zoom-in plot in the lower panel of Fig. 2.17. For planetary eccentricities larger than $e \simeq 0.25$ the planets orbital pericenter distance $(q = a(1-e))$ starts to become comparable to the binary separation resulting in close encounters and hence strongly chaotic and most possibly unstable behavior. We detected collisions of the test mass with one of the binary components and/or ejection of the planet from the system by carrying out single orbit integrations of the planetary orbit for eccentricities around 0.25 and higher.

We investigated the significance of the mass parameter of all involved objects on the overall dynamics. We recomputed the map shown in Fig. 2.17 for various masses of the planet by considering 1 $M_{earth}, 10\ M_{earth}, 1\ M_{jup}, 10\ M_{jup}$ and 50 M_{jup} masses and found no significant qualitative difference in the global dynamics of Fig. 2.17. From comparison

we found that all maps resemble each other more or less qualitatively. In a similar mass parameter survey study we also considered different mass combinations of the binary components that seemed most plausible (see previous sections) and conclude that only small qualitative changes were observed for small changes in the components mass. However, the most significant changes were detected to be close to the location of mean-motion resonances. We note that the timescales of precession frequencies of some of the orbital elements might change significantly for different mass parameters. In addition, we also note that the ETVs can also change significantly for different masses as discussed earlier.

We conclude this section by noting that the best-fit orbital parameters locates the transiting planet Kepler-64b in a quasi-periodic region in (a, e)-space rendering our solution to be plausible from a dynamical point of view. We point out that our work suggest that the planet is relatively close to the 7:1 mean-motion resonance with the binary. We speculate that future observations will reveal whether the planet is or is not part of a resonant configuration.

2.8 Discussion

A single transit event indicates the presence of a third body in an eclipsing binary system. Two transits can define an approximate orbital period for the third body, albeit with uncertainties associated with aliasing and data gaps, or orbital inclination that can prevent a planet from transiting the moving targets of the two stars on each passage of the planet.

Even with a few planetary transits observed, unraveling the system configuration can be challenging.

In general order of increasing challenge, the system configurations for circumbinary planets can be solved for double-lined, double-dipped circumbinaries (planet transits are detected across both stars, e.g. Kepler 34 and 35), followed by double-lined, single-dipped circumbinaries (planetary transits are detected across only one of the stars) and the single-lined circumbinaries, double-dipped and single-dipped. For double-lined eclipsing binary stars, spectra provide the individual stars' masses; for single-lined eclipsing binaries, spectra provide only the mass function that relates the two masses to each other, not the two masses individually. Transits of a third body can break the latter degeneracy inherent to single-lined systems. Single-lined, double-dipped systems wherein transits across both stars occur during a single binary orbit, allow excellent constraints on the masses of the binary stars, as anticipated by Schneider & Chevreton (1990) and demonstrated for Kepler-16 by Doyle et al. (2011). Whether a binary is single- or double-lined depends on observational capabilities; for example, Kepler-16 was originally a single-lined double-dipped system; it has since changed its category to a double-lined system due to very high sensitivity spectra (Bender et al. 2012). Likewise, whether a system is single- or double-dipped also depends on the observational capabilities: even if a planet transits both stars, we may not be able to discern the transits of the fainter star, e.g. Kepler-64. More challenging than the systems that are either double-lined or double-dipped are the single-lined and single-dipped circumbinary systems such as Kepler-38, Kepler-47 and Kepler-64. A large number

of planetary transits, as in the case of Kepler-47b, helps photodynamical modeling to constrain system parameters via Eq. 2.4 (cf. Figure 2.11). However, if only a few transits occur, e.g. Kepler-38 and Kepler-64, there may be doubt as to the uniqueness of a solution with a large number of system parameters.

From the broadening of the spectral lines and the period of amplitude modulations in the light curve, we infer rotation of star A and determine its radius, which in combination with $log(g)$ from stellar spectra or the density of star A from the stellar eclipses, either one indicates a Solar-mass primary star. Small- or undetectable deviations from a linear ephemeris in the primary eclipse times prove the planet is of planetary, not stellar, mass.

The nine planetary transits further constrain the parameters of the two stars, as their center times and durations depend on the ratio of the stellar masses and on the transiting chord length (Eq. 2.4). The latter breaks the degeneracy inherent to the mass function of the single-lined spectra. Thereby we constrain the individual stellar masses of of Kepler-64 and Star A's radius, assuming central planetary transits. Similarly, we confirm the parameters of the Kepler-47 system reported by Orosz et al. (2012).

To solve the dynamical nature of the Kepler-64 system we did a minimization search over a grid space defined by m_1, a_3, e_3, and ω_3, using a three-body numerical integrator in Jacobian coordinates. Taking the first event as a reference point, we found a set of best-fit solutions, defined by the system parameters of the four-dimensional grid space listed above, that predict the midtransit times and durations of the subsequent four events to within an hour. The simulations match the observed events well but we caution that the

combination of fixed grid resolution, triaged parameters space, and the small number of transits limit our ability to choose one of the best fit models over another. Observations of a few additional transits will differentiate our models, because the optimal solutions diverge in their predictions for the center times of the planetary transits.

To detect chaotic solutions in the parameter space, we studied the long term stability of the system using an extensive set of numerical simulations, applying the MEGNO factor. We tested systems with different planetary masses, between 1 M_{earth} and 50 M_{jup}, to evaluate the changes in the dynamical behavior of the three bodies. We do not detect significant difference outside mean motion resonances; a planet starting near a mean-motion resonance, however, exhibits erratic behavior. The ratio of binary star period to the period of the giant planet is, however, not an integer value, giving us confidence that the planet is not on a chaotic orbit. Its orbit is near but beyond the instability region; the ratio of planetary to binary semi-major axis is ~ 3.6, compared to ~ 2.8 of Holman & Wiegert (1999), which is similar to the other Kepler planets and in agreement with theoretical predictions that such configurations should be common.

2.9 Conclusions

We report the discovery and characterization of a gas giant $r = 0.52 \pm 0.018$ $r_{Jupiter}$ circumbinary planet transiting the Kepler-64 eclipsing binary system. The planet revolves around the two stars every $\sim$138 days and transits the 1.47 ± 0.08 $M_{\odot}$ and 1.7 ± 0.06 $R_{\odot}$

F8 primary on a 0.64 AU, $e = 0.1$ orbit. We describe a simple, semi-automatic procedure specifically designed to search for aperiodic transits in the light curves of binary stars. After identifying the transiting signals, we obtained spectra of the two pairs of binary stars, from which we determined the mass function, eccentricity and argument of periapsis for each pair.

We also describe the independent discovery of the Kepler-47bc circumbinary planets by the same method. We discontinued our characterization of that system soon after it was reported by Orosz et al. (2012). Our truncated characterization confirms the parameters they reported.

We coin a phrase to describe circumbinary planetary systems: if planetary transits are detected for only one star, the system is "single-dipped," and for both stars, "double-dipped." We discuss the relative merits of single- or double-lined and single- or double-dipped circumbinary systems.

Periodic variations in the radial velocity of star A measured by Doppler boosting compare favorably with those obtained by the traditional spectroscopic methods (Figure 2.8). The example of Kepler-64 demonstrates the potential of the Doppler-boosting technique for reconnaissance of eclipsing binary stars prior to, or in lieu of, obtaining high-resolution spectra of them.

The family portrait of circumbinary planets discovered by the Kepler mission is filling up quickly, with now seven planets reported in less than a year since the first was reported by Doyle et al. (2011). Kepler-64 joins its peers Kepler 16b, 34b and 35b in the category

of gas giant planets and, like Kepler 38b, orbits a binary system that includes an evolved primary star. With the continued operation of the Kepler mission and its exquisite-quality data, we expect the discovery of circumbinary planets to continue and give us a deeper insight into these exciting systems.

The authors gratefully acknowledge everyone who has contributed to the Kepler Mission, which is funded by NASA's Science Mission Directorate. The Kepler-64 system has been identified and studied independently by Schwamb et al. (2012); we especially acknowledge the collegiality of Meg Schwamb and Debra Fischer. We acknowledge conversations with Josh Carter, Nicolas Crouzet, Selma De Mink, Holland Ford, Danny Lennon, Douglas Long, David Neufeld, Colin Norman, Jerome Orosz, Rachel Osten, M. Słonina, and K. Goździewski.

This research used observations made with 1) the SOPHIE instrument on the 1.93-m telescope at Observatoire de Haute-Provence (CNRS), France, as part of program 12B.PNP.MOUT and 2) the Dual-Imaging Spectrograph on 3.5-m Apache Point Telescope, as part of programs Q2JH01 and Q2JH07. This research made use of the the SIMBAD database, operated at CDS, Strasbourg, France; data products from the Two Micron All Sky Survey (2MASS), the Digitized Sky Survey (DSS), the NASA exoplanet archive NexSci[11]; the Exoplanet Data Explorer[12] of Wright et al. (2011); source code for transit light curves (Mandel & Agol 2002); an eclipsing binary simulator[13] ; the theoretical models[14] of

[11] http://exoplanetarchive.ipac.caltech.edu
[12] http://exoplanets.org
[13] http://astro.unl.edu/naap/ebs/animations/ebs.html
[14] http://svo.cab.inta-csic.es/theory/db2vo/index.php

Hauschildt et al. (1999); a library[15] of stellar spectra of Pickles (1998); SFI/HEA Irish Centre for High-End Computing (ICHEC); PLUTO computing cluster at KASI. V.B.K. and P.R.M. received funding from NASA Origins of Solar Systems grant NNX10AG30G and from HST DD grant 11945. T.C.H acknowledges support by the Korea Research Council for Science and Technology (KRCF) through the Young Scientist Research Fellowship Program grant number 2012-1-410-02 and the SFI/HEA Irish Centre for High-End Computing (ICHEC) for the provision of computational facilities and support. This research was performed in partial fulfillment of the requirements of the PhD of V.B.K. at Johns Hopkins University.

[15] http://www.eso.org/sci/observing/tools/standards/IR_spectral_library.html

Table 2.1 Measured radial velocities.

BJD_{UTC} $-2\,400\,000$	RV ($km\,s^{-1}$)	$\pm1\sigma$ ($km\,s^{-1}$)	Telescope/ Instrument
Kepler-64			
56 029.9593	−30.3	4.1	APO
56 093.8661	−35.7	4.1	APO
56 097.8526	−16.3	4.4	APO
56 111.6009	−41.0	3.6	APO
56 159.5657	−8.36	0.45	OHP193/SOPHIE
56 162.5848	−7.95	0.64	OHP193/SOPHIE
56 175.3481	−28.62	0.76	OHP193/SOPHIE
56 176.3531	−20.94	0.62	OHP193/SOPHIE
56 177.2970†	−15.64	0.50	OHP193/SOPHIE
56 185.5063	−16.49	0.49	OHP193/SOPHIE
56 188.4707	−29.65	0.64	OHP193/SOPHIE
56 193.5113	−45.37	1.03	OHP193/SOPHIE
KIC 10020423 (Kepler-47)			
56 029.9593	−65.9	4.0	APO††
56 093.8661	0.0	4.5	APO
56 097.8526	−59.7	5.1	APO
56 159.5866	26.67	0.08	OHP193/SOPHIE
56 160.5787	34.88	0.13	OHP193/SOPHIE
56 161.5490	24.22	0.08	OHP193/SOPHIE
56 178.3126	−19.07	0.16	OHP193/SOPHIE

†: measurement corrected for sky background pollution.
††: not absolute to barycentric reference

Table 2.2 Parameters of the Binary Star Systems.

Kepler-64					
Parameter	Symbol	Value	Uncertainty (1σ)	Unit	Note
Orbital Period	P	20.000214	-	d	Prša et al. (2011)
Epoch of primary eclipse	$T_{transit}$	2454967.81963	-	BJD	Prša et al. (2011)
Epoch of secondary eclipse	$T_{occultation}$	2454975.6738	0.001	BJD	
Epoch of Periastron passage	T_0	2454973.862	0.15	BJD	
Velocity semi-amplitude	K_1	19.76	0.73	km s^{-1}	
Velocity offset	$\gamma(SOPHIE)$	-23.38	0.38	km s^{-1}	
Velocity offset	$\gamma(APO)$	-20.7	1.8	km s^{-1}	
Argument of Periapsis	ω	214.3	5.4	°	
Eccentricity	e	0.204	0.012		
Semimajor Axis	a	0.1769	0.005	AU	
Orbital Inclination	i	87.59	0.006	°	
Normalized Semimajor Axis	a/r_A	22.08	0.15		
Radius of Star A	r_A	1.7	0.06	$R_\odot$	
Radius of Star B	r_B	0.34	0.015	$R_\odot$	
Ratio of radii	k	0.201	0.015		$k = r_B/r_A$
Mass of Star A	m_A	1.47	0.08	$M_\odot$	
Mass of Star B	m_B	0.37	0.035	$M_\odot$	
Temperature of Star A	T_A	6200	150	K	
Temperature of Star B	T_B	3390	50	K	
V sin i of Star A	$vsini$	31	2	km s^{-1}	
Fe/H of Star A	$[Fe/H]$	-0.15			
Gravity of Star A	log(g)	4.0	0.2		Spectroscopic
Isochronal age of Star A		2.6	$+3.6/-0.3$	Gyr	
KIC 10020423 (Kepler-47)					
Orbital Period	P	7.44837695	0.00000021	d	Orosz et al. (2012)
Epoch of primary eclipse	$T_{transit}$	2454963.24539	0.000041	BJD	Orosz et al. (2012)
Epoch of secondary eclipse	$T_{occultation}$	2454959.426986	0.000277	BJD	Orosz et al. (2012)
Epoch of Periastron passage	T_0	2454965.792	0.076	BJD	
Velocity semi-amplitude	K_1	31.18	0.12	km s^{-1}	
Velocity offset	$\gamma(SOPHIE)$	4.34	0.09	km s^{-1}	
Velocity offset	$\gamma(APO)$	-32.2	2.8	km s^{-1}	
Argument of Periapsis	ω	215.4	3.7	°	
Eccentricity	e	0.0244	0.001		

Table 2.3 Best-fit Parameters for the Dynamical Model.

Binary Stars	Model 1
Mass of Primary Star [$M_{\odot}$]	1.47
Mass of Secondary Star [$M_{\odot}$]	0.37
Radius of Primary Star [$R_{\odot}$]	1.7
Radius of Secondary Star [$R_{\odot}$]	0.34
Gravity of Star A [log(g)]	4.14
Gravity of Star B [log(g)]	4.94
Semimajor Axis [AU]	0.1769
Circumbinary Planet	
Orbital Period [days]	138.51
Semimajor Axis [AU]	0.642
Eccentricity	0.1
Argument of Periastron [degrees]	105
Orbital Inclination [degrees]	90

Table 2.4 Parameters of observed and predicted planetary transits.

Event #	Center (BJD-2450000)	σ (Center)	Depth† [ppm]	σ (Depth)	Duration [days]	σ (Duration)	Center [BJD-2450000]	Duration (days)
Observed							**Model** 1	
1	5070.8267	0.019	870	90	0.5485	0.0378	—	0.56
2	5207.4077	0.011	631	90	0.5125	0.021	5207.43	0.51
3	5344.1308	0.012	914	83	0.6184	0.023	5344.14	0.55
4	5480.004	0.015	1042	78	0.7513	0.029	5479.99	0.76
5	5613.2329	0.013	1043	67	0.891	0.032	5613.22	0.84
6	5749.1914	0.013	939	95	0.4680	0.043	5749.25	0.5
7	5885.9215	0.035	1192	98	0.5235	0.074	5885.97	0.54
8	6022.3334	0.037	974	46	0.5787	0.036	6022.36	0.57
9	6157.0322	0.02	1559	87	1.1353	0.034	6157.00	1.14
Future								
10	—	—	—	—	—	—	6291.04	0.61
11	—	—	—	—	—	—	6427.60	0.54

†: in terms of $(\frac{r_p}{r_A})^2$

Chapter 3

Kepler-413b: a slightly misaligned, Neptune-size transiting circumbinary planet

Kostov, V. B.; McCullough, P. R.; Carter, J. A.; Deleuil, M.; Díaz, R. F.; Fabrycky, D. C.; Hébrard, G.; Hinse, T. C.; Mazeh, T.; Orosz, J. A.; Tsvetanov, Z. I.; Welsh, W. F., 2014, *The Astrophysical Journal*, **784**, 1

Prior to the publication of the paper presented here (but after the submission of the proofs) we have noticed a numerical error in our calculations regarding the Cassini States of the circumbinary planet Kepler-413b. Due to miscommunication between the lead author and the journal, the paper was published before we could correct the error. We have addressed this issue in an erratum (Kostov et al. 2014b), and in the abstract and sections 3.5.2 and 3.6 of this chapter. Additionally, the correct mutual inclination between the planet and the eclipsing binary, Δi, is $\sim 4^\circ$ (as reported in Table 3.4) instead of $\sim 2.5^\circ$ (used in the text of the printed paper). The differences between this chapter and the printed paper are annotated here in the text with [[ ]].

Abstract

We report the discovery of a transiting, $R_p = 4.347 \pm 0.099 R_\oplus$, circumbinary planet (CBP) orbiting the *Kepler* $K + M$ Eclipsing Binary (EB) system KIC 12351927 (Kepler-413) every ~ 66 days on an eccentric orbit with $a_p = 0.355 \pm 0.002 AU$, $e_p = 0.118 \pm 0.002$. The two stars, with $M_A = 0.820 \pm 0.015 M_\odot, R_A = 0.776 \pm 0.009 R_\odot$ and $M_B = 0.542 \pm 0.008 M_\odot, R_B = 0.484 \pm 0.024 R_\odot$ respectively revolve around each other every 10.11615 ± 0.00001 days on a nearly circular ($e_{EB} = 0.037 \pm 0.002$) orbit. The orbital plane of the EB is slightly inclined to the line of sight ($i_{EB} = 87.33 \pm 0.06^\circ$) while that of the planet is inclined by [[$\sim 4^\circ$]] to the binary plane at the reference epoch. Orbital precession with a period of ~ 11 years causes the inclination of the latter to the sky plane to continuously change. As a result, the planet often fails to transit the primary star at inferior conjunction, causing stretches of hundreds of days with no transits (corresponding to multiple planetary orbital periods). We predict that the next transit will not occur until 2020. The orbital configuration of the system places the planet slightly closer to its host stars than the inner edge of the extended habitable zone. [[Additionally, the orbital configuration of the system is such that the CBP may experience Cassini-States dynamics under the influence of the EB,

in which the planet's obliquity precesses with a rate comparable to its orbital precession.]]

3.1 Introduction

A mere two years ago, Doyle et al. (2011) announced the discovery of the first transiting circumbinary planet (CBP), Kepler-16b. Six more transiting CBPs, including a multi-planet system, a CBP in the habitable zone, and a quadruple host stellar system, have been reported since (Welsh et al., 2012; Orosz et al., 2012a,b; Kostov et al., 2013; Schwamb et al., 2013). In comparison, the number of planetary candidates orbiting single stars is significantly larger – three thousand and counting (Burke et al., 2013).

Extensive theoretical efforts spanning more than two decades have argued that planets can form around binary stars (Alexander, 2012; Paardekooper et al., 2012; Pierens & Nelson, 2007, 2008a,b,c, 2013; Martin et al., 2013; Marzari et al., 2013; Meschiari, 2012a,b, 2013; Rafikov, 2013). Simulations have shown that sub-Jupiter gas [[giants]] should be common, and due to their formation and migration history should be located near the edge of the CB protoplanetary disk cavity. Indeed that is where most of the CBPs discovered by *Kepler* reside! Once formed, it has been shown that CBPs can have dynamically stable orbits beyond certain critical distance (Holman & Wiegert, 1999). This distance depends on the binary mass fraction and eccentricity and is typically a few binary separations. All discovered CBP are indeed close to the critical limit – their orbits are only a few tens of percent longer than the critical separation necessary for stability (Welsh et al., 2014). Additionally, models of terrestrial planet formation in close binary systems ($a_{bin} < 0.4AU$) indicate that accretion around eccentric binaries typically produces more diverse and less

populated planetary systems compared to those around circular binaries (Quintana & Lissauer, 2006). In contrast, the location of the ice line in CB protoplanetary disks is expected to be interior to the critical stability limit for 80% of wide, low-mass binary systems ($M_{bin} < 4M_{\odot}$) with $a_{bin} \sim 1AU$ (Clanton, 2013). Thus, Clanton argues, formation of rocky planets in such systems may be problematic. The theoretical framework of formation and evolution of planets in multiple stellar systems demands additional observational support, to which our latest CBP discovery Kepler-413 contributes an important new insight.

The configurations of six of the confirmed CBPs are such that they currently transit their parent stars every planetary orbit. Doyle et al. (2011) note, however, that the tertiary (planet transits across the primary star) of Kepler-16b will cease after 2018, and the quaternary (planet transits across the secondary star) after 2014. The last transit of Kepler-35b was at BJD 2455965 (Welsh et al., 2012); it will start transiting again in a decade. As pointed out by Schneider (1994), some CBP orbits may be sufficiently misaligned with respect to their host EB and hence precessing such that the above behavior may not be an exception. Additionally, Foucart & Lai (2013) argue that circumbinary disks around sub-AU stellar binaries should be strongly aligned (mutual inclination $\theta \leq 2^{\circ}$), in the absence of external perturbations by additional bodies (either during or after formation), whereas the disks and planets around wider binaries can potentially be misaligned ($\theta \geq 5^{\circ}$). Foucart & Lai (2013) note that due to the turbulent environment of star formation, the rotational direction of the gas accreting onto the central proto-binary is in general not in the same direction as that of the central core. Their calculations show that the CB disk is twisted and warped

under the gravitational influence of the binary. These features introduce a back-reaction torque onto the binary which, together with an additional torque from mass accretion, will likely align the CB protoplanetary disks and the host binary for close binaries but allow for misalignment in wider binaries.

The observational consequence of slightly misaligned CBPs is that they may often fail to transit their host stars, resulting in a light curve exhibiting one or more consecutive tertiary transits followed by prolonged periods of time where no transits occur. This effect can be further amplified if the size of the semi-minor axis of the transited star projected upon the plane of the sky is large compared the star's radius.

Such is the case of Kepler-413 (KIC 12351927), a 10.116146-day Eclipsing Binary (EB) system. Its *Kepler* light curve exhibits a set of three planetary transits (separated by $\sim$ 66 days) followed by $\sim$ 800 days with no transits, followed by another group of five transits (again $\sim$ 66 days apart). We do not detect additional events $\sim$ 66 days (or integer multiples of) after the last transit. Our analysis shows that such peculiar behavior is indeed caused by a small misalignment and precession of the planetary orbit with respect to that of the binary star.

Here we present our discovery and characterization of the CBP orbiting the EB Kepler-413 . This paper is organized as an iterative set of steps that we followed for the complete description of the circumbinary system. In Section 3.2 we describe our analysis of the *Kepler* data, followed by our observations in Section 3.3. We present our analysis and results in Section 3.4, discuss them in Section 3.5 and draw conclusions in Section 3.6.

3.2 *Kepler* Data

3.2.1 *Kepler* Light Curve

We extract the center times of the primary (T_{prim}) and secondary (T_{sec}) stellar eclipses, the normalized EB semi major axes (a/R_A), (a/R_B), the ratio of the stellar radii (R_B/R_A), and inclination (i_b) of the binary and the flux contribution of star B from the *Kepler* light curve. Throughout this work, we refer to the primary star with a subscript *"A"*, to the secondary with a subscript *"B"*, and to the planet with a subscript *"p"*. We model the EB light curve of Kepler-413 with ELC (Orosz et al., 2012a).

The *Kepler* data analysis pipeline (Jenkins et al., 2010a) uses a cosmic-ray detection procedure which introduces artificial brightening near the middle of the stellar eclipses of Kepler-413 (see also Welsh et al. 2012). The procedure flags and corrects for positive and negative spikes in the light curves. The rapidly changing stellar brightness during the eclipse and the comparable width between the detrending window used by the pipeline and the duration of the stellar eclipse misleads the procedure into erroneously interpreting the mid-eclipse data points as negative spikes. This leads to the unnecessary application of the cosmic ray correction to the mid-eclipse data points prior to the extraction of the light curve. The target pixel files, however, contain a column that stores the fluxes, aperture positions and times of each flagged cosmic ray event. To account for the anomalous cosmic ray rejection introduced by the pipeline, we add this column back to the flux column using

fv (downloaded from the *Kepler Guest Observer* website) and then re-extract the corrected light curve using the *kepextract* package from PyKE [1] (Still & Barclay, 2012; Kinemuchi et al., 2012). We note that our custom light curve extraction from the target pixel files for Quarters 1 through 14 introduces a known timing error of ~ 67 sec in the reported times which we account for.

Next, we detrend the normalized, raw *Kepler* data (SAPFLUX with a SAPQUALITY flag of 0) of Kepler-413 by an iterative fit with a high-order (50+) Legendre polynomial on a Quarter-by-Quarter basis. A representative section of the light curve, spanning Quarter 15 is shown in Figure 3.1. We use a simple σ-clipping criteria, where points that are 3-σ above and below the fit are removed and the fit is recalculated. Next, the stellar eclipses are clipped out. We note that for our search for transiting CBP we do this for the entire EB catalog listed in Slawson et al. (2011); Kirk et al. (2014). The order of execution of the two steps (detrending and removal of stellar eclipses) generally depends on the baseline variability of the particular target. For quiet stars (like Kepler-413) we first remove the eclipses and then detrend.

Next, we phase-fold the light curve of Kepler-413 on our best-fit binary star period of $P = 10.116146$ days. For fitting purposes, we allow the limb-darkening coefficients of the primary star to vary freely. We note that star B is not completely occulted during the secondary stellar eclipse, and it's contribution to the total light during secondary eclipse needs to be taken into account. The best-fit models to the folded primary and secondary

[1] http://keplergo.arc.nasa.gov/ContributedSoftwarePyKEP.shtml

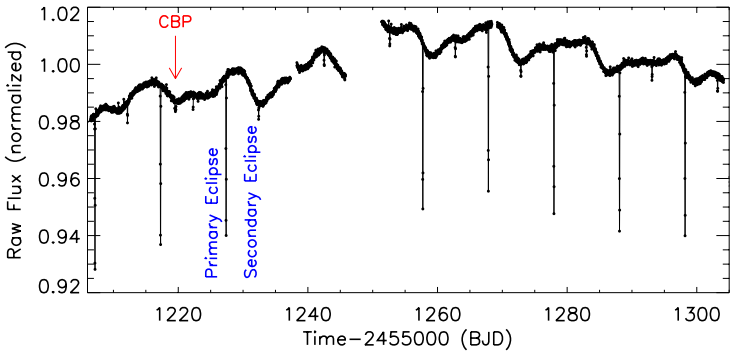

Figure 3.1 A section of the raw (SAPFLUX), normalized *Kepler* light curve of Kepler-413 spanning Quarter 15. The prominent stellar eclipses are clearly seen, with a depth of $\sim 6\%$ and $\sim 0.5\%$ for primary and secondary respectively. The last detected transit of the CBP is indicated with an arrow near day 1219. The gap near day 1250 is due to missing data.

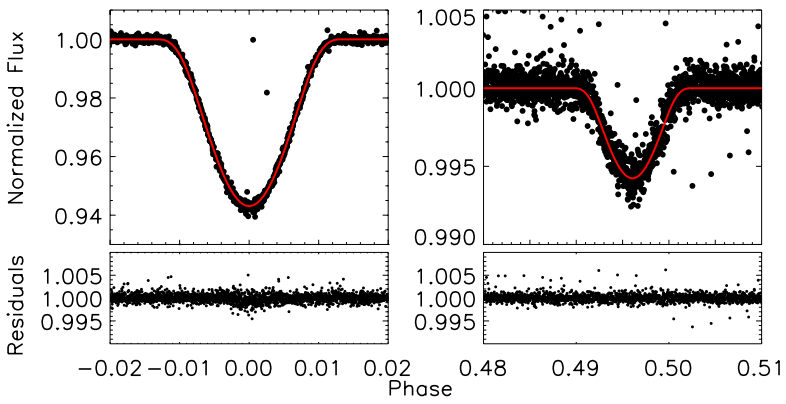

Figure 3.2 ELC model fits (solid lines) to the phase-folded primary (left) and secondary (right) stellar eclipses of Kepler-413 (black symbols); the lower panels show the best-fit residuals. The excess noise near the center of the transit is likely due to star spots.

eclipses, based on the fast analytic mode of ELC (using Mandel & Agol 2002) are shown in Figure 3.2. The best-fit parameters for the ELC model of the *Kepler* light curve of Kepler-413 are listed in Table 3.1. Including a "third-light" contamination of 8% due to the nearby star (see Kostov et al. in prep.), we obtain $k = R_B/R_A = 0.5832 \pm 0.0695$, $a/R_A = 27.5438 \pm 0.0003$, $i_b = 87.3258^\circ \pm 0.0987^\circ$, and $T_B/T_A = 0.7369 \pm 0.0153$.

We measure the stellar eclipse times using the methodology of Orosz et al. (2012a). For completeness, we briefly describe it here. We extract the data around each eclipse and detrend the light curve. Starting with the ephemeris given by our best-fit model, we phase-fold the light curve on the given period. Thus folded, the data were next used to create

an eclipse template based on a cubic Hermite polynomial. Next, adjusting only the center time of the eclipse template, we iteratively fit it to each individual eclipse and measure the mid-eclipse times. To calculate eclipse time variations (ETVs), we fit a linear ephemeris to the measured primary and secondary eclipse times. The Observed minus Calculated (*"O-C"*) residuals, shown in Figure 3.3, have r.m.s. amplitudes of $A_{prim} \sim 0.57$ min and $A_{sec} \sim 8.6$ min respectively. Primary eclipses near days (BJD-2455000) 63, 155, 185, 246, 276, 337, 559, 640, 802, 842, 903, 994, 1015, 1035, 1105, 1126, 1237, and 1247 have been removed due to bad (with a flag of SAPQUALITY$\neq 0$) or missing data. A_{sec} is much larger than A_{prim} because the secondary eclipses are much shallower than the primary eclipses and therefore is much noisier.

The high precision of the measured primary ETVs allow us to constrain the mass of the CBP. The planet contributes to non-zero ETVs through the geometric light travel-time and the dynamical perturbations it exerts on the EB (Borkovits et al., 2013). A CBP of $10M_{Jup}$ and with the orbital configuration of Kepler-413 would cause primary ETVs with amplitudes of $A_{geometric} \sim 1.2$ sec and $A_{dynamic} \sim 2.7$ min respectively. The latter is $\sim 3\sigma$ larger than the measured amplitude of the primary ETVs, indicating an upper limit for the mass of the CBP of $\sim 10M_{Jup}$, and thereby confirming its planetary nature.

[2] $http://archive.stsci.edu/kepler/release\_notes/release\_notes21/DataRelease\_21\_20130508.pdf$

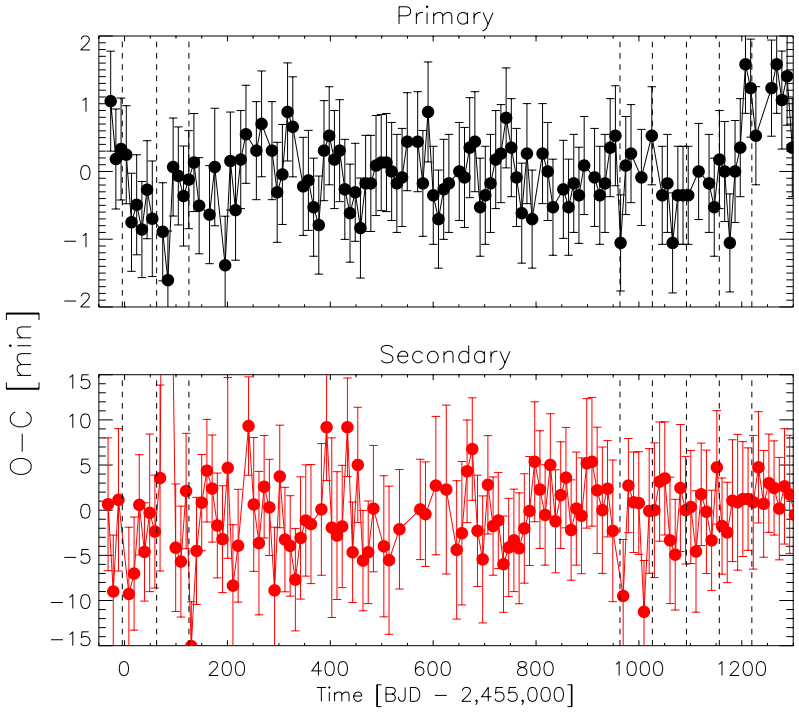

Figure 3.3 Eclipse timing variations of the primary (upper panel, black) and secondary (lower panel, red, or grey color) eclipses of Kepler-413 , in terms of observed versus calculated ("O-C") deviations from linear ephemeris in minutes. The vertical dashed lines indicate the times of the planetary transits. The "O-C" deviations are consistent with noise, there are no discernible trends or periodicities. The last 8 points of the primary ETVs are excluded from our ETV analysis, as their anomalous shift by $\sim$ 1 min after day BJD 1200 is caused by a known[2] absolute timing error of $\sim$ 67 sec for target pixel files from Quarters 1 through 14.

3.2.2 Discovering the transits of Kepler-413b

We discovered the planetary transits of Kepler-413b using the method described in Kostov et al. (2013). For completeness, we briefly outline it here.

Due to the aperiodic nature of the transits of a CBP, traditional methods used to search for periodic signals are not adequate. The amplitude of the transit timing variations between consecutive transits of Kepler-413b , for example, are up to two days ($\sim 3\%$ of one orbital period) compared to an average transit duration of less than 0.5 days. To account for this, we developed an algorithm tailored for finding individual box-shaped features in a light curve (Kostov et al., 2013), based on the widely-used Box-fitting Least-Squares (BLS) method (Kovács et al., 2002). To distinguish between systematic effects and genuine transits, we incorporated the methodology of Burke et al. (2006).

Our procedure is as follows. Each detrended light curve is segmented into smaller sections of equal lengths (dependent on the period of the EB and on the quality of the detrending). Next, each section is replicated N times (the number is arbitrary) to create a periodic photometric time-series. We apply BLS to each and search for the most significant positive (transit) and negative (anti-transit, in the inverted time-series flux) box-shaped features. We compare the goodness-of-fit of the two in terms of the Δ_{χ^2} difference between the box-shaped model and a straight line model. Systematic effects (positive or negative) present in a particular segment will have similar values for $\Delta_{(\chi^2)transit}$ and $\Delta_{(\chi^2)anti-transit}$. On the contrary, a segment with a dominant transit (or anti-transit) feature will be clearly

separated from the rest on a $\Delta_{(\chi^2)transit}$ versus $\Delta_{(\chi^2)anti-transit}$ diagram.

The (transit) – (anti-transit) diagram for Kepler-413 is shown on Fig. 3.4. The segments of the light curve where no preferable signal (transit or anti-transit) is detected form a well-defined cloud, symmetrically distributed along the $\frac{\Delta_{(\chi^2)transit}}{\Delta_{(\chi^2)anti-transit}} = 1$ line. The segments containing the transits of the CBP marked in red (or grey color) diamonds, along with a few other segments where systematic features dominate (black circles), exhibit a preferred $\Delta_{(\chi^2)transit}$ signal. The blue line represents the merit criterion adopted for this target, defined in terms of an iteratively chosen ratio of $\frac{\Delta_{(\chi^2)transit}}{\Delta_{(\chi^2)anti-transit}} = 2$.

The signal for all but one (transit 7) of the Kepler-413b transits is very strong. That transit 7 falls short of the criterion is not surprising. This event is the shortest and also the shallowest and can be easily missed even when scrutinized by eye. For Kepler-413 we had a preliminary dynamical model of the system based on events 1 through 6, prior to the release of Quarter 14 data. The observed events 7 and 8 were very near the predicted times, providing additional constraints to our model.

3.2.3 Stellar Rotation

Flux modulations of up to $\sim 1\%$ on a timescale of ~ 13 days are apparent in the light curve of Kepler-413 . We assume the source of this variation is star spots carried along with the rotation of the stellar surface of the primary, the dominant flux contributor ($\sim 85\%$) in the *Kepler* bandpass. To calculate the rotation period of star A, we compute Lomb-Scargle (L-S) periodograms and perform wavelet analysis (using a Morlet wavelet of order

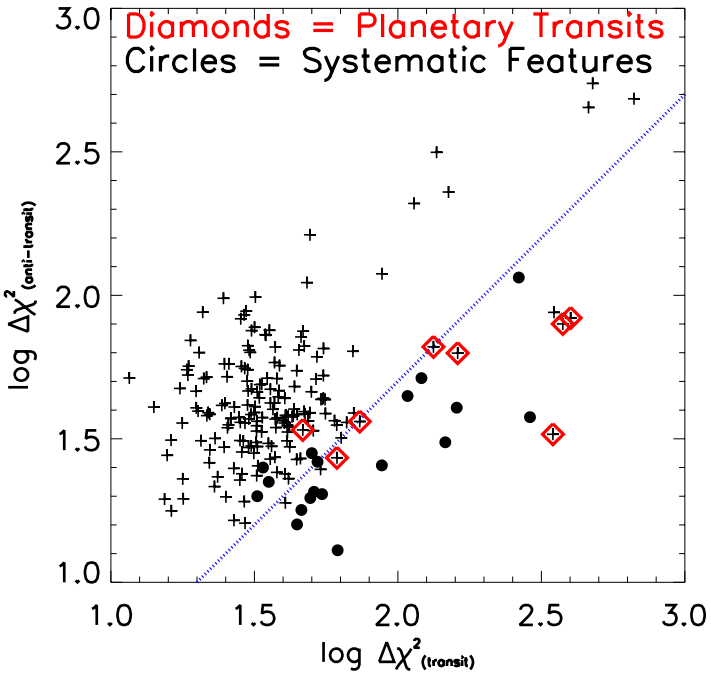

Figure 3.4 The (transit) – (anti-transit) diagram for Kepler-413 . Each symbol represents the logarithmic ratio between the best transit and anti-transit signals detected in individual segments. The planetary transits are marked as red (or grey color) diamonds and the merit criterion line – in blue. Black circles indicate segments where known systemic features mimic transits.

6, Torrence & Compo, 1998) for each Quarter separately. No single period matches all Quarters because of spot evolution as spots emerge/disappear (the most dramatic change, for example, being during Quarter 10). We estimate an average rotation period across all Quarters of $P_{rot,A} = 13.1 \pm 0.3$ days and $P_{rot,A} = 12.9 \pm 0.4$ days from Lomb-Scargle and wavelet analysis respectively.

In addition, we measured the degree of self-similarity of the light curve over a range of different time lags by performing an autocorrelation function (ACF) analysis. In the case of rotational modulation, repeated spot-crossing signatures produce ACF peaks at lags corresponding to the rotation period and its integer multiples (McQuillan, Aigrain and Mazeh 2013). Figure 3.5 depicts the autocorrelation function (ACF) of the cleaned and detrended light curve, after the primary and secondary eclipses were removed and replaced by the value of the mean light curve with a typical random noise. The autocorrelation reveals clear stable modulation with a period of about 13 days. To obtain a more precise value of the stellar rotation we measured the lags of the first 25 peaks of the autocorrelation and fitted them with a straight line, as shown in the lower panel of Figure 3.5 (McQuillan, Mazeh and Aigrain 2013). From the slope of the fitted line we derived a value of $P_{rot,A} = 13.15 \pm 0.15$ days as our best value for the stellar rotation period, consistent with the rotation period derived from the L-S analysis.

We carefully inspected the light curve to verify the period and to ensure that it did not correspond to any harmonic of the spin period. A 13.1-day period matches the spot modulation well. Using the stellar rotation velocity measured from our spectral analysis

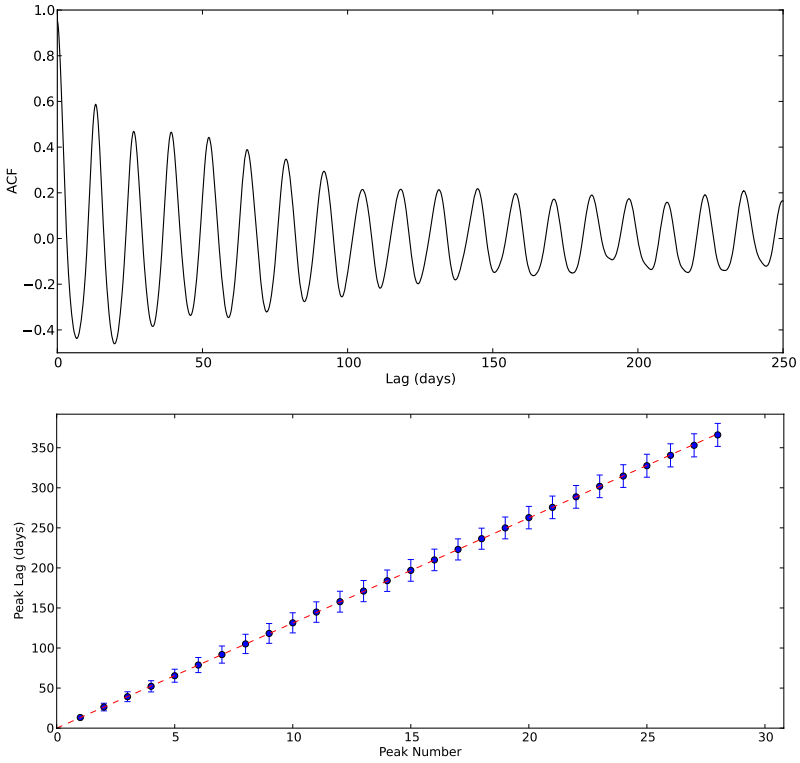

Figure 3.5 Upper panel: The autocorrelation function (ACF) of the cleaned and detrended light curve after the removal of the stellar eclipses. Lower panel: The measured lag of the ACF peaks (solid symbols), fitted with a straight line (dashed line).

we derive an upper limit to star A's radius of $R_A \leq 1.29\ R_\odot$. The surface gravity of star A, $\log g_A = 4.67$, provided by the NASA Exoplanet Archive[3], in combination with the upper limit on R_A indicate $M_A \leq 2.82\ M_\odot$.

3.2.4 Doppler Beaming

A radiation source emitting isotropically and moving at nonrelativistic speed with respect to the observer is subject to a Doppler beaming effect (Rybicki & Lightman, 1979). The apparent brightness of the source increases or decreases as it moves towards or away from the observer. To calculate the Doppler beaming factor for star A, we approximate its spectrum as that of a blackbody with $T_{eff} = 4700$K (see next Section) and the *Kepler* data as monochromatic observations centered at $\lambda = 600$nm. Using Equations 2 and 3 from Loeb & Gaudi (2003), we estimate the boost factor $3 - \alpha = 5.13$. For the value of $K_1 = 43.49$ km s^{-1} derived from the radial velocity, we expect a Doppler beaming effect due to star A with an amplitude of ~ 750 ppm, on par with the intrinsic r.m.s. of the individual *Kepler* measurements. The Doppler beaming contribution due to star B is much smaller (amplitude of ~ 50 ppm) because of its small contribution to the total brightness of the system.

To search for the signal due to star A, we do a custom data detrending of the *Kepler* light curve tailored to the rotational modulations. To each data point t_i, we fit either one or more sine waves with the same mean and period (but different phases and amplitudes) centered on the $[-0.5P_{rot,A} + t_i, t_i + 0.5P_{rot,A}]$ interval. The mean values of the best-fit

[3] http://exoplanetarchive.ipac.caltech.edu

sine waves at each point represent a rotation-free light curve. Few sections of the light curve are consistent with a single spot (or group of) rotating in and out of view, and can be modeled with one sinusoid; most need two, or more. The continuously evolving spot pattern, the faintness of the source and the fact that the binary period is close to the rotation period of the primary star make detection of the otherwise strong expected signal ($\sim$ 750 ppm) challenging. Despite the custom detrending, the modulations in the processed data is consistent with noise and we could not detect the Doppler beaming oscillations caused by the motion of star A. We note that we successfully detected the Doppler beaming effect for Kepler-64 (Kostov et al., 2013), where the amplitude is smaller but the target is brighter and the r.m.s. scatter per 30-min cadence smaller.

3.3 Follow-up Observations

3.3.1 SOPHIE

Kepler-413 was observed in September-October 2012 and in March-April 2013 with the SOPHIE spectrograph at the 1.93-m telescope of Haute-Provence Observatory, France. The goal was to detect the reflex motion of the primary star due to its secondary component through radial velocity variations. SOPHIE (Bouchy et al., 2009) is a fiber-fed, cross-dispersed, environmentally stabilized échelle spectrograph dedicated to high-precision radial velocity measurements. The data were secured in High-Efficiency mode (resolution

power $R = 40\,000$) and slow read-out mode of the detector. The exposure times ranged between 1200 and 1800 sec, allowing a signal-to-noise ratio per pixel in the range $4-8$ to be reached at 550 nm. The particularly low signal-to-noise ratio is due to the faintness of the target ($K_p = 15.52$mag).

The spectra were extracted from the detector images with the SOPHIE pipeline, which includes localization of the spectral orders on the 2D-images, optimal order extraction, cosmic-ray rejection, wavelength calibration and corrections of flat-field. Then we performed a cross-correlation of the extracted spectra with a G2-type numerical mask including more than 3500 lines. Significant cross-correlation functions (CCFs) were detected despite the low signal-to-noise ratio. Their Gaussian fits allow radial velocities to be measured as well as associated uncertainties, following the method described by Baranne et al. (1996) and Pepe et al. (2002a). The full width at half maximum (FWHM) of those Gaussians is 11 ± 1 km s^{-1}, and the contrast is 12 ± 4 % of the continuum. One of the observations (BJD$= 2\,456\,195.40345$) was corrected from the 230 ± 30 m/s blue shift due to Moon light pollution and measured thanks to the reference fiber pointed on the sky (e.g. Hébrard et al., 2008). The other exposures were not significantly polluted by sky background or by light from the Moon. The measured radial velocities are reported in Table 3.2 and plotted in Figure 3.6. Radial velocities show significant variations in phase with the *Kepler* ephemeris.

The radial velocities were fitted with a Keplerian model, taking into account the three constraints derived from the *Kepler* photometry: the orbital period P, and the mid-times of

the primary and secondary stellar eclipses, T_{prim} and T_{sec} respectively. The fits were made using the PASTIS code (Díaz et al., 2013), previously used e.g. by Santerne et al. (2011) and Hébrard et al. (2013). Confidence intervals around the best solutions were determined by Monte Carlo simulations. The histograms of the obtained parameters have a single-peak. We fitted them by Gaussians, whose centers and widths are the derived values and uncertainties reported in Table 3.1. The best fits are over-plotted with the data in Figure 3.6. The dispersion of the residuals of the fit is $106\,\mathrm{m\,s^{-1}}$, in agreement with the error bars of the radial velocity measurements. We did not detect any significant drift of the radial velocities in addition to the reflex motion due to the binary. The small difference between the stellar eclipses, $T_{prim} - T_{sec}$, and $P/2$ measured from *Kepler* photometry indicates that the orbit is not circular. Together with the radial velocities, it allows the detection of a small but significant eccentricity $e = 0.037 \pm 0.002$, and longitude of the periastron $\omega = 279.54 \pm 0.86^{\circ}$. We note that our spectroscopic observations determined Kepler-413 as a single-lined spectroscopic binary, and allowed us to evaluate the binary mass function $f(m)$ from the derived radial velocity semi-amplitude of the primary star $K_1 = 43.485 \pm 0.085\ km\ s^{-1}$.

The signal-to-noise ratio of the final co-added spectrum is too low to allow a good spectral analysis of the star. The profile of the H-α line suggests an effective temperature $T_{\rm eff} \simeq 4700$ K. The width of the CCF implies $v \sin i_* = 5 \pm 2\,\mathrm{km\,s^{-1}}$.

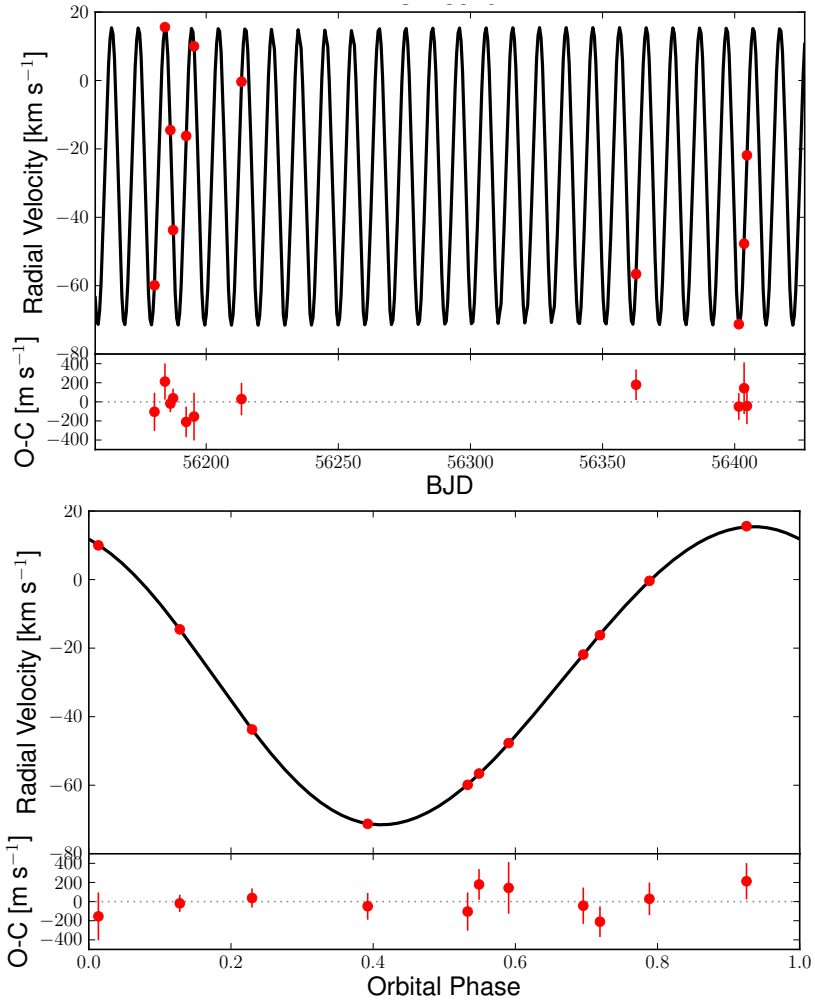

Figure 3.6 SOPHIE radial velocity measurements of Kepler-413 with 1-σ error bars as a function of time (upper) or orbital phase (lower) together with their Keplerian fit and residuals of the fit. Note the scale is km s^{-1} for the radial velocities and m s^{-1} for the O-C residuals.

3.3.2 Third-light companion

The large *Kepler* pixel, $4'' \times 4''$ (Jenkins et al., 2010b), is prone to photometric contamination due to background sources. Unaccounted extra light inside the target's aperture can contribute to an erroneous interpretation of eclipse and transit depths, resulting in incorrect estimation of the relative sizes of the occulting objects. Proper characterization of such contamination is particularly important for the analysis of CBPs (e.g. Schwamb et al., 2013; Kostov et al., 2013).

We note that there is a visible companion ("third light") inside the central pixel of Kepler-413 at a separation of $\sim 1.6''$ from the target, with a magnitude difference of $\Delta K_p \sim 2.8$ (Kostov et al., in prep.). The presence of the companion can be deduced from 2MASS (Skrutskie et al. 2006) and UKIRT (Lawrence et al., 2007) images, and from the full frame *Kepler* image. A marked asymmetry in the target's point spread function, exhibited as a side bump with a position angle of $\sim 218°$, hints at the presence of an object close to Kepler-413 .

During our reconnaissance spectroscopy with the 3.5-m Apache Point Observatory telescope we noticed the companion as a clearly separated star $\sim 1.6''$ away from Kepler-413 . The companion was physically resolved using adaptive-optics-assisted photometry from Robo-AO (Baranec et al., 2013) and seeing-limited infrared photometry from WIYN/WHIRC (Meixner et al., 2010). The measured flux contribution from the companion to the aperture of Kepler-413 is $\sim 8\%, \sim 15\%, \sim 19\%$ and $\sim 21\%$ in the *Kepler*,

J-, H- and Ks-bands respectively (Kostov et al., in prep.); we correct for the contamination in our analysis. A detailed discussion of the companion's properties will be presented in future work (Kostov et al., in prep.).

The presence of such contamination is not unusual: adaptive-optics observations of 90 *Kepler* planetary candidates show that $\sim 20\%$ of them have one visual companion within $2''$ (Adams et al., 2012); lucky imaging observations by Lillo-Box et al. (2012) find that $\sim 17\%$ of 98 *Kepler* Objects of Interest have at least one visual companion within $3''$. As more than 40% of spectroscopic binaries with $P < 10$ days are members of triple systems according to Tokovinin (1993), it is reasonable to consider the visible companion to be gravitationally bound to Kepler-413 . Using Table 3 of Gilliland et al. (2011), for a contaminating star of $K_p \leq 18.5$ mag (i.e. $\Delta K_p \leq 3$ mag), and interpolating for the galactic latitude of Kepler-413 of $b = 17.47^{\circ}$, we estimate the probability of a random alignment between a background source and Kepler-413 within an area of radius $1.6''$ to be ~ 0.002. That despite the odds there is a star within this area indicates that the "third light" source is gravitationally bound to the EB, and could provide a natural mechanism for the observed misalignment of Kepler-413b . Based on this statistical estimate, we argue that Kepler-413b is a CBP in a triple stellar system.

3.4 Analysis of the system

A complete description of a CBP system requires 18 parameters – three masses (M_A, M_B and M_p), three radii (R_A, R_B, R_P), six orbital elements for the binary system ($a_{bin}, e_{bin}, \omega_{bin}, i_{bin}$, Ω_{bin} and phase $\phi_{0,bin}$) and six osculating orbital elements for the CBP ($a_p, e_p, \omega_p, i_p, \Omega_p$ and $\phi_{0,p}$). As described in Sections 3.2 and 3.3, some of these parameters can be evaluated from either the *Kepler* data, or from follow-up photometric and spectroscopic observations. Measurements of the stellar radial velocities provide $e_{bin}, \omega_{bin}, i_{bin}$ and the binary mass function $f(m)$ (but not the individual stellar masses, as we observed Kepler-413 as a single-lined spectroscopic binary). The relative sizes of the two stars and the inclination of the binary system are derived from the *Kepler* light curve. Based on the measured ETVs, we approximate the planet as a test particle ($M_p = 0$) for our preliminary solution of the system, and solve for its mass with the comprehensive photodynamical model. The value of Ω_{bin} is undetermined (see Doyle et al. 2011; Welsh et al. 2012), unimportant to our analysis, and is set equal to zero.

Here we derive the mass of the eclipsing binary (thus the masses of the primary and secondary stars) and the radius of the primary star from the planetary transits. Next, we produce a preliminary numerical solution of the system – a necessary input for the comprehensive photometric dynamical analysis we present in Section 3.4.2. We study the dynamical stability of Kepler-413b in Section 3.4.3.

3.4.1 Initial Approach: Planetary transits and preliminary solutions

The mid-transit times, durations, and depths of consecutive transits of a CBP are neither constant nor easy to predict when the number of observed events is low. However, while strictly periodic transit signals can be mimicked by a background contamination (either an EB or a planet), the variable behavior of CBP transits provide a unique signature without common false positives.

Different outcomes can be observed depending on the phase of the binary system. While the CBP travels in one direction on the celestial sphere when at inferior conjunction, the projected velocities of each of the two stars can be in either direction. When the star and the planet move in the same direction, the duration of the transit will be longer than when the star is moving in the opposite direction with respect to the planet. As shown by Kostov et al. (2013), the transit durations as a function of binary phase can be used to constrain the a priori unknown mass of the binary and the radius of the primary star (both critical parameters for the photodynamical model described below), assuming the planet transits across the same chord on the star. Typically, the more transits observed and the wider their EB phase coverage, the better the constraints are.

While useful for favorable conditions, the approximation of Kostov et al. (2013) is not applicable in general, and we extend it here. Depending on the relative positions of the CBP and the star on the sky, the CBP will transit across different chord lengths with associ-

ated impact parameters, such that different transits will have different durations and depths. A particular situation may be favorable, such as the cases of Kepler-64b and Kepler-47b where the CBPs transit across approximately constant chords. While the chord lengths do change from one transit to another, the variations are small as the stellar radii are sufficiently large, the mutual inclination between the orbits of the CBP and the EB is small, and the approximation in Kostov et al. (2013) applies. The situation for Kepler-413 , however, is quite the opposite – due to the misalignment between the two orbits and the small stellar radius, the chord length changes so much from one transit to another that the impact parameter is often larger than $R_A + R_p$, i.e. the planet misses a transit. To properly account for this novel behavior of a CBP, we modify our analytic approach accordingly to allow for variable impact parameter. Expanding on Equation (2.4) of Kostov et al. (2013), we add another term (D) to the numerator:

$$t_{dur,i} = \frac{ABD_i}{1 + ACx_i} \tag{3.1}$$

$$\begin{aligned} A &= (M_{bin})^{-1/3} \\ B &= 2R_c(\frac{P_p}{2\pi G})^{1/3} \\ C &= -f(m)^{1/3}(\frac{P_p}{P_{bin}})^{1/3}(1-e^2)^{-1/2} \\ D_i &= \sqrt{1-{b_i}^2} \\ x_i &= (e\sin\omega + \sin(\theta_i + \omega)) \end{aligned} \tag{3.2}$$

where $t_{dur,i}$, b_i and θ_i are the duration, impact parameter and binary phase of the i_{th} transit

respectively, M_{bin} is the sum of the masses of the two stars of the EB, P_p is the average period of the CBP, $R_c = R_A + R_p$ is the transited chord length (where R_A and R_p are the radius of the primary star and the planet respectively), $f(m)$ is the binary mass function (Eqn. 2.53, Hilditch, 2001), and e and ω are the binary eccentricity and argument of periastron respectively. Applying Equation 3.1 to transits with $b>0$ results in smaller derived M_{bin} compared to transits across a maximum chord, $b=0$.

The generally used method to derive b from the measured transit durations and depths for a planet orbiting a single star (Seager & Mallen-Ornellas, 2003) is not applicable for a CBP. The CBP impact parameter cannot be easily derived from the observables. From geometric considerations, b is:

$$b = \sqrt{(x_s - x_p)^2 + (y_s - y_p)^2} \tag{3.3}$$

where (x_s, y_s) and (x_p,y_p) are the sky x and y - coordinates of the star and the planet respectively. The former depend on the binary parameters only and can be calculated from Hilditch (2001)[4]:

$$\begin{aligned} x_s &= r_s \cos(\theta_{bin} + \omega_{bin}) \\ y_s &= r_s \sin(\theta_{bin} + \omega_{bin}) \cos i_{bin} \end{aligned} \tag{3.4}$$

where $r_s, \omega_{bin}, \theta_{bin}$ and i_{bin} can be directly estimated from the radial velocity measurements and from the *Kepler* light curve. The CBP coordinates, however, depend on the unknown

[4]Generally, Ω_{bin} (the EB longitude of ascending node) is undetermined and assumed to be zero

mass of the binary and on the instantaneous orbital elements of the CBP Ω_p, θ_p and i_p. Assuming a circular orbit for the CBP:

$$\begin{aligned} x_p &= a_p[cos(\Omega_p)cos(\theta_p) - sin(\Omega_p)sin(\theta_p)cos(i_p)] \\ y_p &= a_p[sin(\Omega_p)cos(\theta_p) + cos(\Omega_p)sin(\theta_p)cos(i_p)] \end{aligned} \tag{3.5}$$

where a_p is the semi-major axis of the CBP. For a mis-aligned CBP like Kepler-413b , however, $\Omega_p \neq 0.0$ and equations 3.5 cannot be simplified any further. In addition, due to 3-body dynamics, all three CBP orbital parameters vary with time. As a result, incorporating Equation 3.3 into Equation 3.1 will significantly complicate the solution.

However, we note that Equation 3.1 uses only part of the information contained in the *Kepler* light curve, i.e. transit durations and centers; it does not capitalize on the depth or shape of each transit. To fully exploit the available data, we evaluate the impact parameters of the eight transits directly from the light curve by fitting a limb-darkened transit model Mandel & Agol (2002) to each transit individually. The procedure is as follows. First, we scale the CB system to a reference frame of a mock, stationary primary star with a mass equal to the total binary mass of Kepler-413 . The scaling is done by adjusting for the relative velocities of the primary star Kepler-413 A ($V_{x,A}$), and of the CBP ($V_{x,p}$). The impact parameters are not modified by the scaling, as it does not change the distance between the planet and the star or their mutual inclination during each transit. We approximate $V_{x,p}$ as a single value for all transits:

$$V_{x,p} = (\frac{2\pi G M_{bin}}{P_p})^{1/3} = const \tag{3.6}$$

A mock planet orbits the star on a circular, $P_p = 66$ day orbit (the period of Kepler-413b). The relative velocity of the observed CBP at the time of each transit ($V_{x,obs,i}$) is calculated as the absolute difference between the instantaneous $V_{x,p}$ and $V_{x,A}$:

$$V_{x,obs,i} = |V_{x,p} - V_{x,A,i}| \tag{3.7}$$

where $V_{x,A,i}$ can be calculated from the fit to the RV measurements. The scaled time of the i_{th} mock transit $t_{mock,i}$, referred to the time of minimum light, is then:

$$t_{mock,i} = \frac{|V_{x,p} - V_{x,A,i}|}{V_{x,p}} t_{obs,i} \tag{3.8}$$

where $t_{obs,i}$ is the observed time during the i_{th} transit. The mock transits are "stretched" with respect to the observed ones when $V_{x,A} < 0$ and "compressed" when $V_{x,A} > 0$.

While $V_{x,p}$ depends on the unknown binary mass, it does so by only its third root (Equation 3.6). For the low-mass binary we expect from the *Kepler* Input Catalog, $V_{x,p}$ varies only by $\sim 26\%$ for M_{bin} between $1.0 M_\odot$ and $2.0 M_\odot$. Thus, the dominant factor in Eqn. 3.8 is $V_{x,A,i}$.

The eight scaled, mock transits are next fit individually, sharing the same binary mass M_{bin}, size of the primary star R_A, and of the CBP radius R_p. The normalized semi-major axis of the mock planet, a_{mock}/R_A, depends on the binary phase of each transit and is different for different transits – for fitting purposes it ranges from $(a_p - a_A)/R_A$ for transits

near secondary stellar eclipse to $(a_p + a_A)/R_A$ for those near primary eclipse. Here a_p is the mean semi-major axis of the CBP Kepler-413b and a_A is the semi-major axis of the primary star Kepler-413 -A. For light curve modeling, we use the limb-darkening coefficients from Section 3.2.

To estimate R_p/R_A, we first fit a limb-darkened light curve model to the scaled transit 8. The binary star is near a quadrature during the transit, $|V_{x,A,i}|$ is near zero, $a_{mock} \approx a_p$, M_{bin} does not significantly affect Equation 3.8 and the scaling is minimal ($t_{mock,i} \approx t_{obs,i}$). To confirm that the scaling is negligible, we fit transit 8 for all M_{bin} between 1.0 and 2.0. The differences between the derived values for $R_{p,8}/R_A$ are indistinguishable – $R_{p,8}/R_A = 0.053$ for all M_{bin}, where $R_{p,8}$ is the radius of the planet deduced from the fit to scaled transit 8. We next use $R_{p,8}$ for light curve fitting of the other seven scaled transits. Also, the best-fit $a_{mock,8}$ from transit 8 is used in combination with a_A to constrain the allowed range for $a_{mock,1-7}$ for the other seven transits, as described above. We note that while transit 1 also occurs near quadrature, the transit duration and depth are both much smaller than than those of transit 8, making the latter a better scaling ruler. The derived impact parameters for transits 1 through 8 are $0.85, 0.71, 0.17, 0.61, 0.84, 0.67, 0.78$ and 0.05 respectively. We note that these are used to estimate M_{bin} in Equation 3.1 only and not as exact inputs to the photodynamical analysis described below.

To evaluate the applicability of our approach, we test it on synthetic light curves designed to mimic Kepler-413b (8 transits, 10-11 misses, CBP on a $\sim$ 66-day orbit). For a noise-less light curve, we recover the simulated impact parameters of the 8 transits to

within 0.01, the semi-major axis to within 1% and the size of the planet to within 10%. Allowing the (known) mass of the simulated binary star to vary by $\pm 0.5 M_{\odot}$ modifies the derived impact parameters by not more than 0.02. For a simulated set of light curves with normally distributed random noise of $\sim$ 700 ppm r.m.s. per 30-min cadence (similar to that of Kepler-413) we recover the impact parameters to within 0.15, the semi-major axis, and the size of the planet each to within 10%. The good agreement between the derived and simulated model values validates the method. The observed (black) and scaled (green, or light color) transits of Kepler-413b and the best-fit models (red, or grey color) to the latter are shown on Figure 3.7.

We note that there are secondary effects not taken into account by Equation 3.8. $V_{x,A}$, assumed to be constant in the equation, in reality varies throughout the duration of the transit. In principle, the longer the CBP transit, the more the stellar velocity and acceleration deviate from constancy. Longer transits (like Transit 6, see Figure 3.7) have asymmetric shape and the circular orbit approximation for the CBP in Equation 3.8 is not optimal. Depending on the phase of the binary star at the time of transit, both the magnitude and the sign of $V_{x,A}$ may change – near quadrature, for example, the star changes direction.

Next, we apply Equation 3.1 to the eight transits of Kepler-413b for constant and for variable chords and compare the results. The best-fit models for the two cases are shown on Figure 3.8 as the blue and red curve respectively. The derived values for M_{bin} and R_A are 1.41 $M_{\odot}$ and 0.70 $R_{\odot}$ for constant b and 1.33 $M_{\odot}$ and 0.91 $R_{\odot}$ for varying b. Not accounting for different impact parameters overestimates M_{bin} and underestimates R_A.

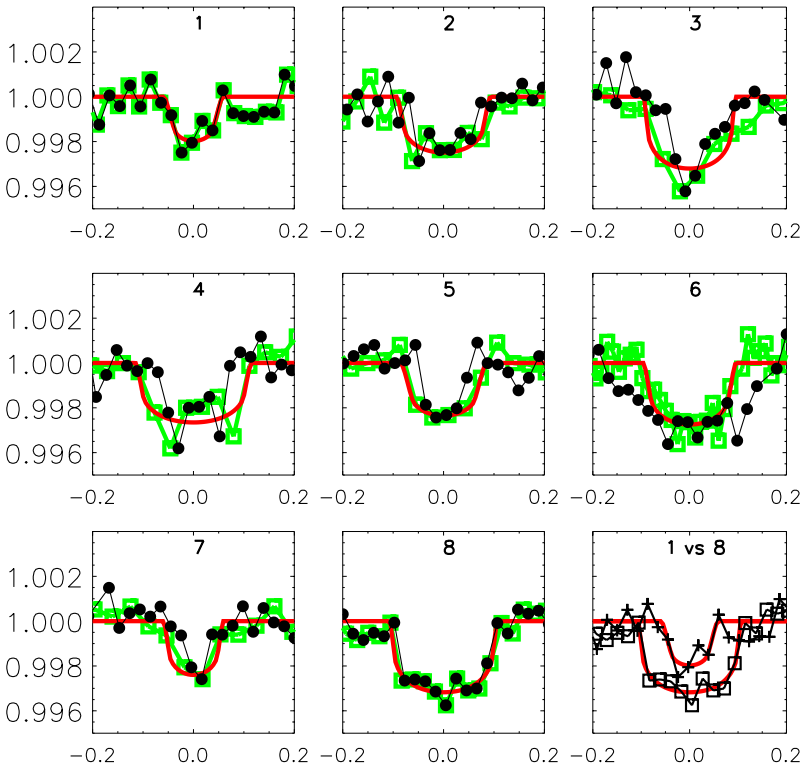

Figure 3.7 Quadratic limb-darkened light curve model fits to the eight scaled transits of Kepler-413b . Black symbols represents observed data, green (or light color) square symbols – scaled data according to Eqn. 3.8 and red (or grey color) curve – model fit to the scaled transits. We use the last transit (number 8) as a template for light curve fitting to estimate R_p/R_A and a_p. The binary is near quadrature during transit 8, $V_{x,A}$ is at its lowest and the scaling used in Equation 3.8 is minimal. The result of orbital misalignment is represented in the last panel ("1 vs 8"), where we compare the two transits (square and cross symbols for Transits 8 and 1 respectively) that occur near the same EB phase, but have different impact parameters.

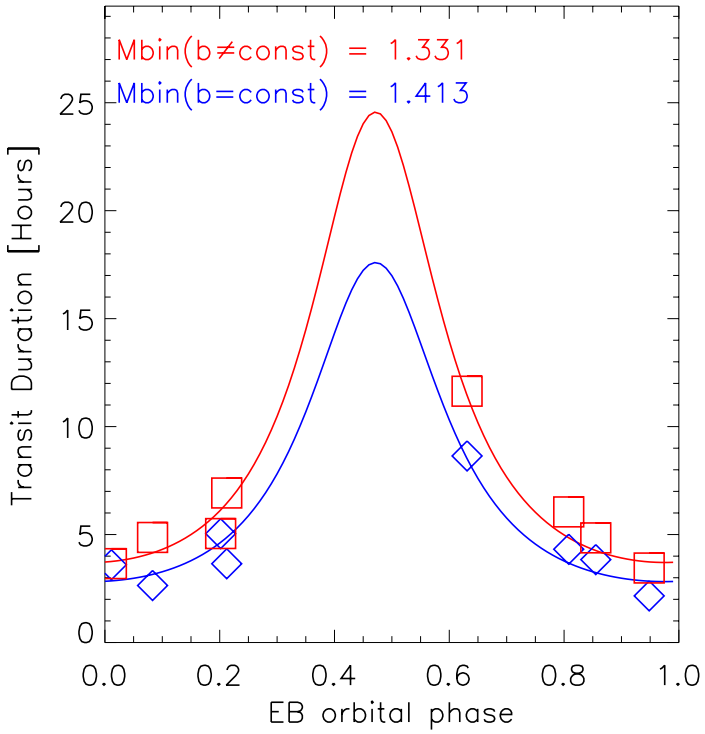

Figure 3.8 CBP transit duration vs EB phase fits for Kepler-413b using Equation 3.1. The blue and red curves represent the best fit for constant and for varying impact parameters respectively. The derived binary mass is 1.41 $M_{\odot}$ and 1.33 $M_{\odot}$ for the two cases respectively. The derived primary radius is 0.70 $R_{\odot}$ for the blue curve and 0.91 $R_{\odot}$ for the red curve. Allowing for variable impact parameter results in a lower and higher estimates of M_{bin} and R_A respectively compared to the the case of constant impact parameter.

We use the measured transit duration uncertainties to constrain the derived binary mass as follows. We simulate a set of 10,000 scrambled observations, each consisting of the eight measured transit durations individually perturbed by adding a normally distributed noise with a standard deviation of 20 min. Next, we apply Equation 3.1 to each realization. The distribution of the derived M_{bin} for the entire set of scrambled observation is shown in Figure 3.9. The blue histogram represents the solutions accounting for constant chord length and the red histogram – for variable chord length. The median values for binary mass and their 1-sigma deviations are $1.41 \pm 0.19\ M_{\odot}$ and $1.33 \pm 0.17\ M_{\odot}$ for the former and latter case respectively. Based on these results, for our preliminary photodynamical search over the parameter space of the Kepler-413 system (described next) we adopt the latter case, and allow the binary mass to vary from 1.16 to 1.5 $M_{\odot}$.

For our initial photodynamical solutions we use a numerical N-body integrator (described in Kostov et al., 2013) to solve the equations of motion. For completeness, we briefly outline it here and discuss the modifications we added for diagnosing Kepler-413 . The integrator is an implementation of the SWIFT code[5] adapted for IDL. Due to the particular behavior of the CBP transits of Kepler-413b , we can neither fix the planetary inclination i_p to 90 degrees, or the ascending node Ω_p and the initial phase $\phi_{0,p}$ to zero. Unlike the case of Kepler-64b described in Kostov et al. (2013), here we solve numerically for these three parameters. Furthermore, it is not optimal to choose the time of the first transit as the starting point of the numerical integration as Kostov et al. (2013) did. Doing so

[5]http://www.boulder.swri.edu/ hal/swift.html

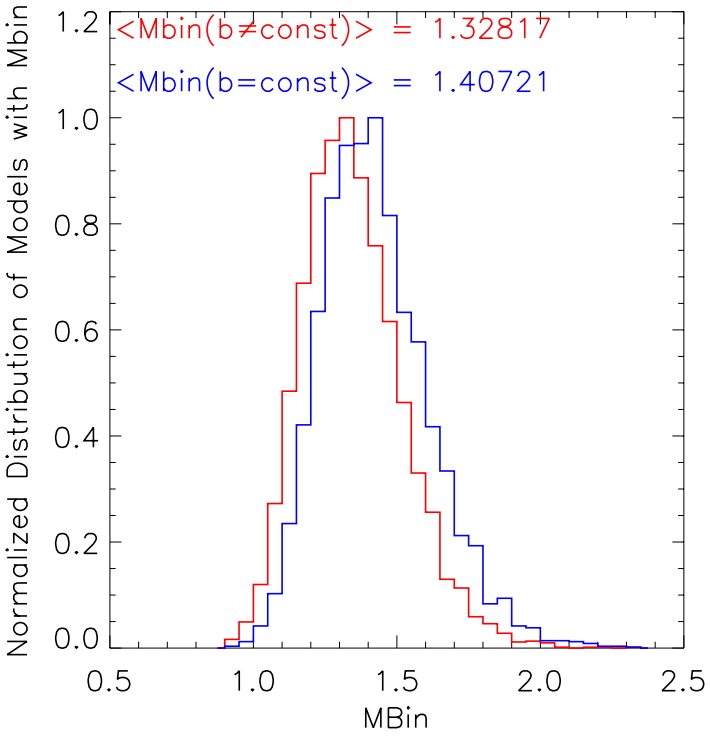

Figure 3.9 Distribution of derived binary masses from Eqn. 3.1 for a set of 10,000 scrambled observations. The blue histogram represents the distribution for constant impact parameters for all eight transits, and the red histogram – for different impact parameters.

would introduce an additional parameter – the impact parameter b_0 of the chosen transit; the estimated impact parameters of the individual transits indicated above are too coarse to be used in the photodynamical model. Instead, here we specify initial conditions with respect to the time when the planet is crossing the x-y plane ($z_p = 0$), approximately 3/4 of a planetary period prior to transit 2, i.e. at $t_0 = 2,455,014.465430$ (BJD). This allows us to find the true anomaly of the planet ($\theta_p = 2\pi - \omega_p$), and the planet's eccentric and mean anomalies at the reference time. The number of free parameters we solve for is 9: $[M_A, a_p, e_p, \omega_p, i_p, \Omega_p, \phi_{0,p}, R_A$ and $R_p]$.

Restricting the binary mass to the 1σ range indicated by the scrambled durations, we fit preliminary photodynamical models to the eight transits of Kepler-413b by performing a grid search over the 8 parameters. The quality of the fit is defined as the chi-square value of the observed minus calculated (O-C) mid-transit times of all 8 events. Starting with an initial, coarse time step of 0.1 days, we select the models that reproduce the mid-transit times of each of the observed eight transits to within 0.05 days and also correctly "miss" all other events by more than $R_A + R_p$. Next, we refine the grid search by reducing the time step to 0.02 days, and minimize again. The best-fit model is further promoted for a detailed MCMC exploration as described in the next section.

3.4.2 Comprehensive photometric-dynamical analysis

The *Kepler* light curve and radial velocity data for Kepler-413 were further modeled using a comprehensive photometric-dynamical model. This model uses a dynamical simulation,

assuming only Newton's equations of motion and the finite speed of light, to predict the positions of the stars and planet at the observed times (e.g., Doyle et al., 2011; Welsh et al., 2012). The parameters of this simulation are functions of the initial conditions and masses of the three bodies, and are provided by the preliminary simulations described above. These positions are used as inputs – along with radii, limb darkening parameters, fluxes and "third-light" contamination – to a code (Carter et al., 2011; Pál, 2012) that produces the modeled total flux (appropriately integrated to the *Kepler* 'long cadence' exposure). This flux is compared directly to a subset of the full *Kepler* data. The radial velocity data of the larger star are compared to the velocities determined by the dynamical simulation at the observed times.

We isolate only the *Kepler* data within a day of the stellar eclipses or suspected planetary transit crossing events (data involving 'missing' events are included as well). Those data, excluding the eclipse features, are divided by a linear function in time in order to detrend the light curve for local astrophysical or systematic features that are unrelated to the eclipses.

The model described in this section has 23 adjustable parameters. Three parameters are associated with the radial velocity data: the RV semi-amplitude of star A, K_A, the RV offset, γ_A, and a 'jitter' term, $\sigma_{\rm RV}$, that is added in quadrature to the individual RV errors, correcting for unaccounted systematic error sources. The initial conditions are provided as instantaneous Keplerian elements of the stellar (subscript *"bin"*) and planetary (subscript *"p"*) orbits, defined in the Jacobian scheme: the periods, $P_{bin,p}$, the sky-plane inclinations

$i_{bin,p}$, vectorial eccentricities $e_{bin,p}\cos(\omega_{bin,p})$, $e_{bin,p}\sin(\omega_{bin,p})$, the relative nodal longitude $\Delta\Omega = \Omega_p - \Omega_{bin}$ and the times of barycenter passage $T_{bin,p}$. The latter parameters are more precisely constrained by the data than the mean anomalies; however, they may be related to the mean anomalies, $\eta_{bin,p}$, via

$$\frac{P_{bin,p}}{2\pi}\eta_{bin,p} = t_0 - T_{bin,p} + \frac{P_{bin,p}}{2\pi}\left[E_{bin,p} - e_{bin,p}\sin(E_{bin,p})\right] \quad (3.9)$$

where $E_{bin,p}$ are the eccentric anomalies at barycenter passage, defined by

$$\tan\left(\frac{E_{bin,p}}{2}\right) = \sqrt{\frac{1-e_{bin,p}}{1+e_{bin,p}}}\tan\left(\frac{\pi}{4} - \omega_{bin,p}\right) \quad (3.10)$$

Two parameters are the mass ratios between stars and planet, M_A/M_B and M_p/M_A. The remaining 7 parameters are related to the photometric model: the density of star A, ρ_A, the two radii ratios, R_B/R_A and R_b/R_A, the *Kepler*-band flux ratio F_B/F_A, the linear limb darkening parameter of star A, u_1, and the additional flux from contaminating sources F_X/F_A. A final parameter parameterizes the Gaussian distribution of the photometric residuals, $\sigma_{\rm LC}$.

We adopted uniform priors in all the parameters excluding the vectorial eccentricities and F_X/F_A. For those parameters we enforced uniform priors in $e_{bin,p}$ and $\omega_{1,2}$ and a Gaussian prior in F_X/F_A with mean 0.08 and variance 0.0001. The likelihood of a given set of parameters was defined as

$$\begin{aligned} L \propto & \prod^{N_{\rm LC}} \sigma_{\rm LC}^{-1}\exp\left[-\frac{\Delta F_i^2}{2\sigma_{\rm LC}^2}\right] \\ & \times \prod^{N_{\rm RV}} \left(\sigma_{\rm RV}^2 + \sigma_i^2\right)^{-1/2}\exp\left[-\frac{\Delta {\rm RV}_i^2}{2\left(\sigma_i^2 + \sigma_{\rm RV}^2\right)}\right] \end{aligned} \quad (3.11)$$

where $\Delta{\rm LC}_i$ is the residual of the ith photometric measurement and $\Delta{\rm RV}_i$ is the residual of the ith radial velocity measurement with formal error σ_i.

We explored the parameter space with a Differential Evolution Markov Chain Monte Carlo (DE-MCMC) algorithm ter Braak and Vrugt (2008). In detail, we generated a population of 60 chains and evolved through approximately 100,000 generations. The initial parameter states of the 60 chains were randomly selected from an over-dispersed region in parameter space bounding the final posterior distribution. The first 10% of the links in each individual Markov chain were clipped, and the resulting chains were concatenated to form a single Markov chain, after having confirmed that each chain had converged according to the standard criteria including the Gelman-Rubin convergence statistics and the observation of a long effective chain length in each parameter (as determined from the chain autocorrelation).

The photodynamical fits to the 8 observed transits of the CBP are shown in Figure 3.10. We note that our model predicts a ninth, very shallow and buried in the noise transit, labeled as "A" in Figure 3.10. For clarity, we label the observed transits with a number, and those either missed or not detected with a letter. We tabulate the results of this analysis in Tables 3.3 and 3.4, reporting the median and 68% confidence interval for the marginalized distributions in the model parameters and some derived parameters of interest. The parameters we adopt throughout this paper are the "best-fit" values reported in Tables 3.3 and 3.4. The orbital configuration of the system is shown on Figure 3.11. The orbit of the CBP evolves continuously and, due to precession, is not closed. We note that our best-fit mass for the planet is large for its radius. The expected mass is $M_p \sim 16 M_\oplus$, using the mass-radius relation of Weiss et al. (2013) for $1 M_\oplus < M < 150 M_\oplus$, whereas our model provides

$M_p \sim 67 M_\oplus \pm 21 M_\oplus$. This suggests that either Kepler-413b is a much denser planet (mix of rock, metal, gas), or that the mass is even more uncertain than stated, and a factor of 2-3 times likely smaller.

We note that the binary orbit reacts to the gravitational perturbation of the planet. As a result, the EB orbital parameters and eclipse times are not constant. The effect, however, is difficult to measure with the available data. Also, the planetary orbit does not complete one full precession period between transits 1 and 8. The precession period for our best-fit model is $\sim$ 4000 days, in line with the analytic estimate of $\sim$ 4300 days (for equal mass stars) based on Schneider (1994) . After transit 8, the transits cease as the planetary orbit precesses away from the favorable transit configuration. The transits will reappear after BJD 2458999 (2020 May 29).

3.4.3 Orbital Stability

The minimum critical semi-major axis (Holman & Wiegert (1999), Eq. 3) for the best-fit parameters of the Kepler-413 system is $a_{crit} = 2.55\ a_{bin} = 0.26$ AU. With a semi-major axis that is $\approx 37\%$ larger than the critical limit ($a_p = 0.3553$ AU), the orbit of the planet Kepler-413b is in a gravitationally stable region. We note that due to the planet's non-zero eccentricity, its closest approach to the binary is reduced by $(1-e)$ and the stability criterion is more tight – $r_{p,min} = a_p \times (1-e_p) = 0.3168$ AU, closer compared to a zero-eccentricity orbit but still beyond a_{crit}.

Three-body systems are notorious for exhibiting complex dynamical behavior spurred

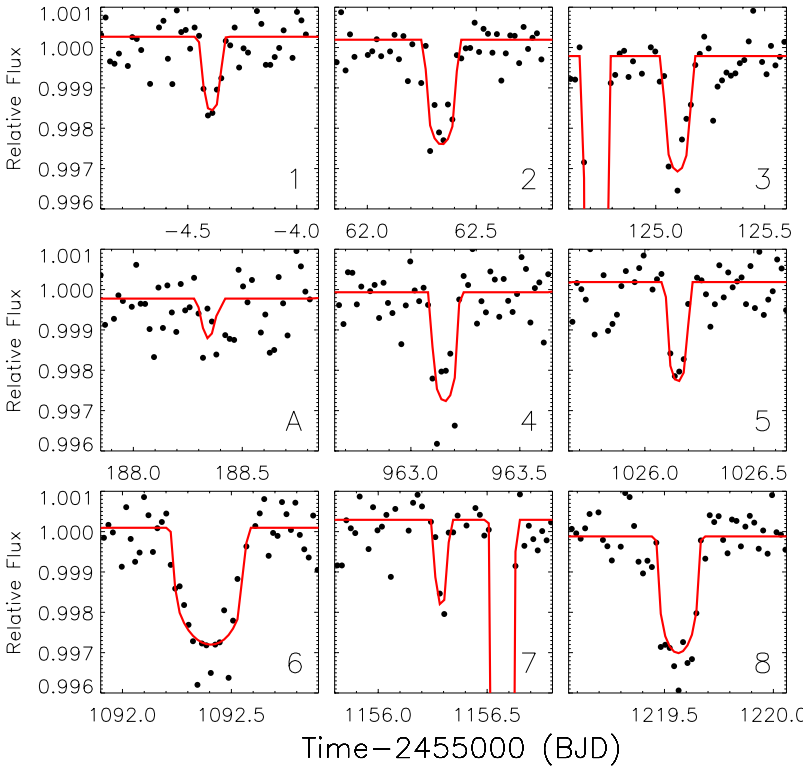

Figure 3.10 Photodynamical fits (red, or grey color) to the 8 observed (and to a predicted ninth, labeled as "A" near time 188.35 (BJD - 2,455,000), very shallow and buried in the noise) transits (black symbols) for the best-fit model in Tables 3.3 and 3.4. Stellar eclipses are also shown at times 124.7 and 1156.5 (BJD - 2,455,000). We note the timescale between transits 3 and 4.

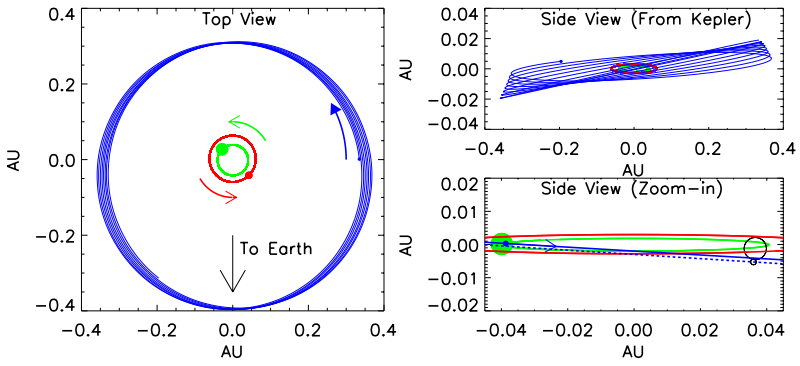

Figure 3.11 Orbital configuration of Kepler-413b over the course of $1/8$ precession period ($1/8$ of ~ 11 years). The orbits of the primary (green, or light color) and secondary (red, or grey color) stars, and of the CBP (blue, or dark color), are to scale on the left and lower right panels. The EB symbols in the left panel, the CBP symbols and the vertical axis in the upper right panel are exaggerated by a factor of 5, 5, and 10 respectively. The EB symbols in the lower right panel are to scale. The precession of the argument of periastron of the CBP (ω_p) as it increases by [[$\sim 45^\circ$]] is clearly seen in the left panel. Two consecutive passages of the CBP at inferior conjunction are shown in the lower right panel, demonstrating a missed transit: the solid overlapping symbols (and blue, or dark color line for the sky path of the CBP) illustrate the configuration of the system at the last observed transit (transit 8) and, one planetary period later, one missed transit (open symbols for the primary star and the CBP respectively).

by mean-motion resonances (MMR). To explore the long-term stability of the Kepler-413 system we have studied its dynamical behavior by utilizing the MEGNO[6] factor $\langle Y \rangle$ (Cincotta & Simó, 2000a,b; Cincotta et al., 2003), a widely used method for dynamical analysis of mutliplanet systems (Goździewski et al., 2008; Hinse et al., 2010). We note that by a stable orbit here we refer to an orbit that is stable only up to the duration of the numerical integration, i.e. a quasi-periodic orbit. The time scale we use is sufficient to detect the most important mean-motion resonances. However, the dynamical behavior of the system past the last integration time-step is unknown.

We utilized the MECHANIC software[7] (Słonina et al., 2012; Słonina, Goździewski & Migaszewski, 2014) to calculate MEGNO maps for Kepler-413 , applying the latest MEGNO implementation (Goździewski et al., 2001; Goździewski, 2003; Goździewski et al., 2008). The maps have a resolution of 350 x 500 initial conditions in planetary semi-major axis (a_p) and eccentricity (e_p) space, each integrated for 200,000 days (corresponding to $\sim 20,000$ binary periods). Quasi-periodic orbits are defined as $|\langle Y \rangle - 2.0| \simeq 0.001$; for chaotic orbits $\langle Y \rangle \to \infty$ as $t \to \infty$. The MEGNO map computed for the best-fit parameters of Table 3.4 is shown in Figure 3.12. The cross-hair mark represents the instantaneous osculating Jacobian coordinates of Kepler-413b . Purple (or dark) color indicates a region of quasi-periodic orbits, whereas yellow (or light) color denotes chaotic (and possibly unstable) orbits. The CBP sits comfortably in the quasi-periodic (purple) region of (a,e)-space between the 6:1 and 7:1 MMR (not unlike Kepler-64b, see Kostov et al., 2013),

[6]Mean Exponential Growth of Nearby Orbits
[7]https://github.com/mslonina/Mechanic

confirming the plausibility of our solution from a dynamical perspective.

3.5 Discussion

"*Why Does Nature Form Exoplanets Easily?*", ponders Heng (2012). Both planetary formation scenarios of core accretion and gravitational collapse require complex processes at work and even more so for the violent environments of CBPs. Yet the plethora of discovered planets (Burke et al., 2013) indicates that planetary formation is ubiquitous. Martin et al. (2013) argue that it may be in fact easier to form planetary systems around close binary stars than around single stars, if there is a quiescent, low-turbulence layer present in the mid plane of the CB disks. Unlike disks around single stars, the surface density in a CB disk peaks in such a "dead zone" and, being close to the snow line, provides an ideal site for planetary formation. In addition, Alexander (2012) has shown that circumbinary disks around binary stars with $a_{bin} < 1$ AU persist longer than disks around single stars, suggesting that formation of CBPs should be commonplace.

The [[$\Delta i \sim 4^\circ$]] misalignment of Kepler-413b is notably larger than that of the other *Kepler*-discovered CBPs (with an average of $\sim 0.3^\circ$). It is, however, comparable to the mutual inclination between Kepler-64b and its host EB, the only known quadruple stellar system with a CBP. It is comparable to the mutual orbital inclinations of $1^\circ - 2.3^\circ$ reported for the *Kepler* and *HARPS* multiplanet systems orbiting single stars, and of the Solar System value of $2.1^\circ - 3.1^\circ$, including Mercury (Fabrycky et al. 2012; Fang and Margot, 2012;

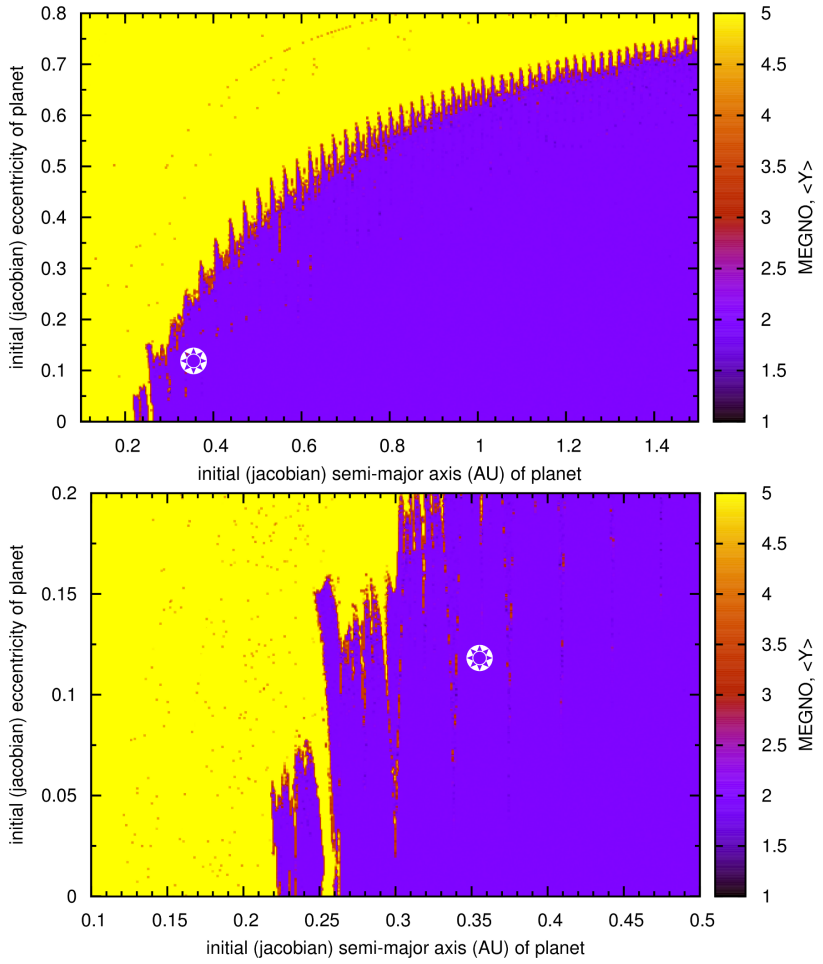

Figure 3.12 Upper panel: MEGNO map of Kepler-413b , using the best-fit parameters from Table 3.4. Purple (or dark) color outlines quasi-periodic regions in the (a,e)-space, and yellow (or light) color – chaotic (and possibly unstable) regions (see text for details). The cross-hair mark denotes the instantaneous Jacobian coordinates of the planet, placing it firmly in a quasi-periodic orbit, and confirming our solution from a dynamical perspective. Lower panel: Same as the upper panel, but zoomed-in on a smaller region around the (a,e) of the planet, conforming its location in the quasi-stable region.

Figueira et al., 2012; Lissauer et al., 2011).

Quillen et al. (2013) argue that one plausible scenario responsible for the excitation of planetary inclinations is collisions with embryos. The authors note that measured correlations between planetary mass and inclination can provide strong clues for this scenario. While planetary masses are difficult to measure, photodynamical models of slightly misaligned CBP like Kepler-413b can provide an important venue to test this hypothesis by providing constraints on masses and inclinations. Additionally, according to Rappaport et al. (2013) up to 20% of close binaries have a tertiary stellar companion, based on extrapolation from eclipse time variations (ETVs) measured for the entire *Kepler* EB catalog. Eggleton & Tokovinin (2008) find that $\sim 25\%$ of all multiple systems with a solar-type star are triples and higher order. A tertiary companion on a wide orbit can be responsible for complex dynamical history of the binary system involving Kozai cycles with tidal friction (Kozai, 1962; Fabrycky & Tremaine, 2007b; Kiseleva et al., 1998; Eggleton & Kiseleva-Eggleton, 2001; Pejcha et al., 2013).

A robust correlation between the occurrence rate of planets and (single) host star metallicities has been established over the past 10 years (Mayor et al., 2011; Howard, 2013). While it is equally likely to detect small planets around stars of wide metallicity range, giant planets ($R{>}4R_{Earth}$, Howard, 2013) are preferentially found in orbits around metal-rich stars. Such dichotomy naturally originates from the core-accretion scenario for planet formation, with the caveat that in-situ formation may be more appropriate to describe the presence of low-mass planets close to their star (Howard, 2013). It is interesting to note that

7 of the *Kepler* CB planets are gas giants, with $R \geq 4.3 R_{Earth}$, (the only exception being Kepler 47b) but all 7 host stellar systems are deficient in metals compared to the Sun.

Eclipsing binary systems have long been proposed to be well-suited candidates to the discovery of transiting planets due to the favorable orbital orientation of the stellar system. However, EBs may not be as favorable as generally thought. Given the correct orientation, planets orbiting single stars will transit at every inferior conjunction. As we have shown here, and also discussed by Schneider (1994), misaligned CBPs, however, may either transit or miss depending on their instantaneous orbital configuration. If the configuration is favorable, one can observe several consecutive transits. Otherwise there may be a few, widely-separated transits or even only a single transit. A trivial case is no transits at all during the course of the observations, where the planetary orbit has not yet precessed into the favorable transit geometry and the first "good hit" may be approaching; even a very misaligned system will occasionally transit. Thus, a non-detection of tertiary transits in the light curve of an EB does not rule out the possibility to observe a transiting CBP in the future. This statement is trivially obvious for planets with periods much longer than the duration of observations. However, as this work has illustrated, the statement also applies to short-period planetary orbits with non-zero mutual inclinations.

Such photodynamical effects may further affect the deduced occurrence rate of CBP, even after accounting for detection efficiency, systematic effects, etc. Aligned systems have a strong selection effect, but many systems (potentially a "silent majority" of CBPs) could be misaligned and precessing, and Kepler-413b will be the prototype of that class of

objects.

"*...The existence of planets in these systems [CBP]...*", Paardekooper et al. (2012) note, "*...baffles planet formation theory...*". The facts that the confirmed CBPs are so close to the theoretical limit for dynamical stability, and that shorter-period EBs have typically longer-period CBPs (further away from the critical limit) hint at an interesting dynamical history, and can be directly addressed by finding more CB systems. Future additions to the still small family of CBPs will add important new insight into our understanding of these remarkable objects. Or, perhaps more interestingly, the new discoveries will baffle the theoretical framework even further.

3.5.1 Stellar Insolation

Our best-fit photodynamical model places Kepler-413b on a 0.355 AU-orbit around two stars with effective temperatures of $T_A = 4700$K, estimated from SOPHIE, and $T_B = 3460$K, derived from the temperature ratio T_B/T_A from ELC, respectively (see Table 3.1). The combined incident flux $S_{tot} = S_A + S_B$ due to the two stars A and B at the orbital location of Kepler-413b is shown in Figure 3.13. It varies from a minimum of $\sim 1.64\ S_\star$ to a maximum of $\sim 3.86\ S_\star$ (where $S_\star$ is the mean Solar constant of 1368 W m^{-2}) on two different timescales (stellar and planetary periods), with an average of $\sim 2.42\ S_\star$. Following Kane & Hinkel (2013), we calculate the effective temperature of the EB, $T_{eff,AB}$, as that of a source with an energy flux similar to that of the two stars combined. From Wien's displacement law, and using the combined blackbody radiation of the two stars, we estimate

$T_{eff,AB} \sim 4500$ K. Following Kopparapu et al. (2013) cloud-free models, the inner edge of the habitable zone ("runaway greenhouse") for the Kepler-413 system is at an incident stellar flux $S_{inner} = 0.91\ S_\star$ (red, or grey line in Figure 3.13); the outer edge ("maximum greenhouse") is at $S_{outer} = 0.28\ S_\star$ (blue, or dark line in Figure 3.13). Kepler-413b is slightly closer to its host star than the inner edge of the habitable zone. We note that the inner edge distance for the habitable zone of the Kepler-413 system for dry desert planets is at $\sim 0.32\ AU$ (Equation 12, Zsom et al. (2013)), $\sim 2.71\ S_\star$, for a surface albedo of 0.2 and 1% relative humidity. This limiting case places Kepler-413b ($a_p = 0.3553\ AU$) in the dry desert habitable zone for most of its orbit.

The flux variations experienced by the CBP, coupled with the peculiar behavior of the planetary obliquity described next may result in very interesting and complex weather and climate patterns on Kepler-413b and similar CBPs.

3.5.2 Cassini States

Next we shall discuss how the quick orbital precession, which is highly constrained by the transit fits, should affect the spin orientation of Kepler-413b . Instantaneously, each of the stars causes a torque on the rotational bulge of the planet, but over one EB orbit, and even over one orbit of the CBP, this torque causes little reorientation of the planet. Over many orbits, however, the effect of this torque adds coherently. If we replace the stars with a point mass at their barycenter, the small-obliquity precession angular frequency of the planetary

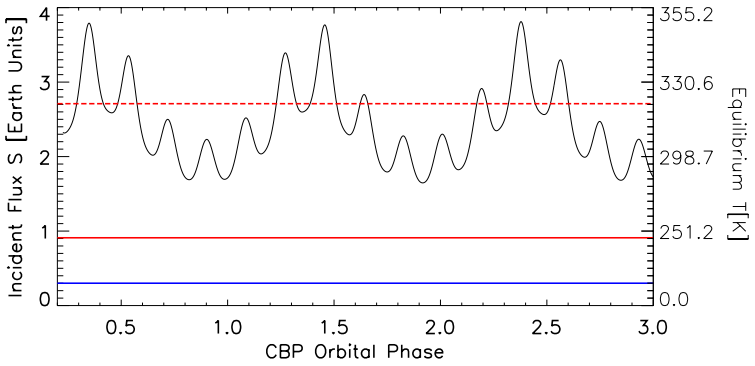

Figure 3.13 Bolometric luminosity in units of $S_\star = 1368\ Wm^{-2}$ (the mean Solar constant), incident at the orbital location of Kepler-413b (black line) as a function of the orbital phase of the planet, and equilibrium temperature for a Bond albedo of 0.34. The CBP orbital phase is defined as $\phi_p = t/P_p$, with $\phi_p = 0$ at $t_0 = 2{,}455{,}014.46543$ (BJD). The planet is slightly closer to its host stars than the inner edge of the habitable zone, which is at $S_{inner} = 0.91\ S_\star$. For comparison, we show the inner (red line) and outer (blue) edges of the habitable zone of Kepler-413 . The dashed line indicates the inner edge of the dry desert habitable zone, $S_{inner,desert} = 2.71\ S_\star$; the planet is in the dry desert habitable zone for most of its orbit.

spin would be (e.g., Fabrycky et al. 2007a):

$$\alpha = \frac{k_{2,p}}{c_p}\frac{M_A + M_B}{M_p}(1-e_p^2)^{-3/2}(R_p/a_p)^3 S_p, \tag{3.12}$$

where $k_{2,p}$ is the apsidal motion constant (half the Love number) of the CBP, c_p is the normalized moment of inertia, and S_p is the spin angular frequency of the planet.

In the presence of quick orbital precession, the dynamics become much richer, as Cassini states appear (Ward & Hamilton, 2004; Hamilton & Ward, 2004; Fabrycky et al., 2007a; Levrard et al., 2007). These states are fixed-points of the spin dynamics in which the spin and orbit precess at the same rate around the total angular momentum. Thus the effect is a 1:1 secular resonance between the orbital precession and the spin precession. The orbital precession rate, g, is known from the best-fitting model $g = 0.57$ radians/year. [[Taking a 16-hr, Neptune-like rotation period for Kepler-413b , $k_{2,p} = 0.1$, $c_p = 0.08$, and assuming $M_p = 15 M_\oplus$, with the above values of the constants, we have $\alpha = 0.02$ radians/year, considerably less than the orbital precession g.

The spin feels the precession-averaged effect of the eclipsing binary orbit, and so the spin-precession pole of the planet is close to the orbit normal of the binary (the dominant angular momentum) and oscillates at the orbital precession frequency of 11 years. This is the case of the Earths moon, whose orbit around the Earth precesses quickly due to solar perturbations, much faster than its α value, and it is tidally damped to Cassini State 2. The spin of Kepler-413b may also have free obliquity (not tidally damped), in which case the planets obliquity would precess around the binary axis with a period of $\sim$300 years. However, we caution that the value of α for the case of Kepler-413b is very uncertain due

to the poorly constrained parameters, particularly M_p and S_p.]]

It is beyond the scope of this work to calculate the obliquity evolution of Kepler-413b in detail. We expect, however, that it would give interesting boundary conditions for climate models (Langton & Laughlin, 2007). Another consideration is that the α value would have changed as the planet cooled, as that contraction would result in changes in R_p, $k_{2,p}$, c_p, and S_p; the scanning of α could cause trapping into a Cassini resonance (Winn & Holman, 2005). We expect that at the orbital distance of Kepler-413b , tides would be too weak to cause spin alignment, but we note that in other systems such alignment would bring the planetary spin to a Cassini state rather than standard spin-orbit locking (Fabrycky et al., 2007a).

Finally, we suggest that spin-precession of a planet may actually be observable for CBP systems. Carter & Winn (2010) pointed out that a precessing planet will display a time-varying surface area to a transit observer, due to the oblateness of the planet changing orientations. A Saturn-like oblateness with a 30° obliquity results in a few-percent change in depth over the precession cycle. The radii ratios in some CBP systems are constrained by *Kepler* photometry at the $\sim 1\%$ level, thus variations at this level might be detectable. This is considerably more observable than the transit shape signature of oblique planets (Seager & Hui, 2002; Barnes and Fortney, 2003).

3.6 Conclusions

We report the discovery of a $R_p = 4.347 \pm 0.099\ R_\oplus$ planet transiting the primary star of Kepler-413 . The system consists of two K+M stars that eclipse each other every 10.116146 days. Due to the small misalignment ([[$\Delta i \sim 4^\circ$]]) between the binary and CBP orbital planes, the latter precesses and the planet often fails to transit the primary star. The CBP revolves around the EB every ~ 66 days on an orbit with $a_p = 0.355$ AU and $e = 0.118 \pm 0.002$. The orbital configuration of the system is such that we observe a set of three transits occurring ~ 66 days apart, followed ~ 800 days later by five more transits also separated by ~ 66 days from each other. We note that, among the known transiting CBPs, Kepler-413b is the only CBP with a higher eccentricity compared to its host binary star.

Spectroscopic measurements determined the target as a single-lined EB, and provided its mass function, eccentricity and argument of periastron. Photometric observations identified a nearby companion ("third light") to Kepler-413 inside the central *Kepler* pixel, and addressed its flux contamination to the target's light curve (Kostov et al., in prep.). Based on statistical estimates, we propose that the companion star is gravitationally bound to the EB, making Kepler-413b a CBP in a triple stellar system.

Our best-fit model places Kepler-413b slightly closer to its host stars than the inner edge of the extended habitable zone, with the bolometric insolation at the location of the planet's orbit varying between $\sim 1.75\ S_\star$ and $\sim 3.9\ S_\star$ on multiple timescales (where $S_\star = 1368\ Wm^{-2}$, the mean Solar constant). The planet is, however in the dry desert hab-

itable zone for most of its orbit. [[Also, the peculiar orbital configuration of the system indicates that Kepler-413b may be subject to Cassini-States dynamics. Depending on the angular precession frequency of the planet, its spin and orbital precession rates could be commensurate where the spin-precession pole of the planet is close to the orbit normal of the binary.]]

The transits of a CBP provide precise measurements on the stellar and planetary sizes and on the masses of the host binary star. Our discovery adds to the growing knowledge about CBPs: their radii, masses, occurrence frequency about which types of stars, when they formed (first versus second generation) and even whether the concept of habitability can be extended beyond single-star planetary systems. The results reported here can be applied to studies of the formation and evolution of protoplanetary disks and planetary systems in multiple-stellar systems.

This research was performed in partial fulfillment of the requirements of the PhD of V.B.K. at Johns Hopkins University. The authors gratefully acknowledge everyone who has contributed to the *Kepler* Mission, which is funded by NASA's Science Mission Directorate. We acknowledge conversations with Nicolas Crouzet, Holland Ford, K. Goździewski, Nader Haghighipour, Amy McQuillan, Colin Norman, Rachel Osten, Neill Reid, Jean Schneider, M. Słonina, and Martin Still. The authors thank the referee for the helpful comments and suggestions.

This research used observations made with the SOPHIE instrument on the 1.93-m telescope at Observatoire de Haute-Provence (CNRS), France, as part of programs 12B.PNP.MOUT

and 13A.PNP.MOUT. This research made use of the the SIMBAD database, operated at CDS, Strasbourg, France; data products from the Two Micron All Sky Survey (2MASS), the Digitized Sky Survey (DSS), the NASA exoplanet archive NexSci[8]; source code for transit light curves (Mandel and Agol 2002); SFI/HEA Irish Centre for High-End Computing (ICHEC); Numerical computations presented in this work were partly carried out using the SFI/HEA Irish Centre for High-End Computing (ICHEC, STOKES) and the PLUTO computing cluster at KASI; Astronomical research at Armagh Observatory is funded by the Department of Culture, Arts and Leisure (DCAL). V.B.K. and P.R.M. received funding from NASA Origins of Solar Systems grant NNX10AG30G, and NESSF grant NNX13AM33H. W.F.W. and J.A.O. gratefully acknowledge support from the National Science Foundation via grant AST-1109928, and from NASA's *Kepler* Participating Scientist Program (NNX12AD23G) and Origins of Solar Systems Program (NNX13AI76G). T.C.H acknowledges support by the Korea Research Council for Science and Technology (KRCF) through the Young Scientist Research Fellowship Program grant number 2013-9-400-00. T.M. acknowledges support from the European Research Council under the EU's Seventh Framework Programme (FP7/(2007-2013)/ ERC Grant Agreement No. 291352) and from the Israel Science Foundation (grant No. 1423/11).

[8]http://exoplanetarchive.ipac.caltech.edu

Table 3.1 Parameters of the Binary Star System.

Kepler-413					
Parameter	Symbol	Value	Uncertainty (1σ)	Unit	Note
Orbital Period	P_{bin}	10.116146	0.000001	d	*Kepler* photometry
Epoch of primary eclipse	T_{prim}	2454972.981520	-	BJD	Prša et al. (2011)
Epoch of secondary eclipse	T_{sec}	2454977.999	0.001	BJD	Prša et al. (2011)
Epoch of Periastron passage	T_0	2454973.230	0.023	BJD	SOPHIE
Velocity semi-amplitude	K_1	43.489	0.085	km s^{-1}	SOPHIE
Velocity offset	γ	-27.78	0.05	km s^{-1}	SOPHIE
Argument of Periapsis	ω_{bin}	279.54††	0.86	$\circ$	SOPHIE
Eccentricity	e_{bin}	0.0372	0.0017		SOPHIE
Orbital Inclination	i_{bin}	87.3258	0.0987	$\circ$	*Kepler* photometry†
Normalized Semimajor Axis	a_{bin}/R_A	27.5438	0.0003		*Kepler* photometry†
Fractional Radius	R_B/R_A	0.5832	0.0695		*Kepler* photometry†
Temperature of Star A	T_A	4700	-	K	Spectroscopic
Temperature ratio	T_B/T_A	0.7369	0.0153	K	*Kepler* photometry†
Limb-Darkening Coeff. of Star A	x_A	0.3567	0.0615	K	*Kepler* photometry†
V sin i of Star A	$V sini$	5	2	km s^{-1}	SOPHIE
Fe/H of Star A	$[Fe/H]$	-0.2	-		NexSci†††
Gravity of Star A	$\log g_A$	4.67	-		NexSci

†: ELC fit (Orosz et al., 2012a)

††: Observer at -z

†††: http://exoplanetarchive.ipac.caltech.edu

Table 3.2 Measured radial velocities.

BJD_{UTC} $-2\,400\,000$	RV ($km\,s^{-1}$)	$\pm 1\sigma$ ($km\,s^{-1}$)
56 180.42595	−59.89	0.20
56 184.39404	15.59	0.19
56 186.44561	−14.52	0.09
56 187.47375	−43.73	0.10
56 192.42495	−16.21	0.16
56 195.40345†	9.99	0.25
56 213.36121	−0.37	0.17
56 362.67907	−56.59	0.16
56 401.55880	−71.26	0.14
56 403.56461	−47.72	0.27
56 404.62680	−21.87	0.19

†: measurement corrected for sky background pollution.

Table 3.3 Model parameters for the photometric-dynamical model. We adopt the "best-fit" values as the system's parameters. The reference epoch is $t_0 = 2,455,014.46543$ (BJD).

Index	Parameter Name	Best-fit	50%	15.8%	84.2%
	Mass parameters				
0	RV Semi-Amplitude Star A, K_A (km s^{-1})	43.42	43.49	-0.16	$+0.19$
1	Mass ratio, Star B, M_B/M_A	0.6611	0.6592	-0.0035	$+0.0034$
2	Planetary mass ratio, M_p/M_A ($\times 1000$)	0.245	0.186	-0.078	$+0.078$
	Stellar Orbit				
3	Orbital Period, P_{bin} (day)	10.1161114	10.1161185	-0.0000101	$+0.0000099$
4	Time of Barycentric Passage, $t_{bin} - 2455000$ (BJD)	8.34898	8.34902	-0.00024	$+0.00024$
5	Eccentricity Parameter, $e_{bin}\sin(\omega_{bin})$	-0.0359	-0.0360	-0.0023	$+0.0022$
6	Eccentricity Parameter, $e_{bin}\cos(\omega_{bin})$	0.006169	0.006166	-0.000037	$+0.000038$
7	Orbital Inclination, i_{bin} (deg)	87.332	87.301	-0.060	$+0.050$
	Planetary Orbit				
8	Orbital Period, P_p (day)	66.262	66.269	-0.021	$+0.024$
9	Time of Barycenteric Passage, $t_p - 2455000$ (BJD)	96.64	96.57	-0.17	$+0.16$
10	Eccentricity Parameter, $\sqrt{e_p}\sin(\omega_p)$	0.3426	0.3435	-0.0033	$+0.0031$
11	Eccentricity Parameter, $\sqrt{e_p}\cos(\omega_p)$	-0.027	-0.022	-0.013	$+0.014$
12	Orbital Inclination, i_p (deg)	89.929	89.942	-0.016	$+0.024$
13	Relative Nodal Longitude, $\Delta\Omega_p$ (deg)	3.139	3.169	-0.064	$+0.080$
	Radius/Light Parameters				
14	Linear Limb Darkening Parameter, u_A	0.599	0.643	-0.036	$+0.036$
15	Density of Star A, ρ_A (g cm^{-3})	1.755	1.799	-0.049	$+0.066$
16	Radius Ratio, Star B, R_B/R_A	0.624	0.650	-0.032	$+0.043$
17	Planetary Radius Ratio, R_p/R_A	0.0514	0.0517	-0.0013	$+0.0013$
18	Stellar Flux Ratio, F_B/F_A ($\times 100$)	5.90	6.40	-0.76	$+1.05$
	Relative Contamination, $F_{\rm cont}/F_A$ ($\times 100$)				
19	All Seasons	7.6	8.0	-1.0	$+1.0$
	Noise Parameter				
20	Long Cadence Relative Width, $\sigma_{\rm LC}$ ($\times 10^5$)	67.78	67.76	-0.53	$+0.54$
	Radial Velocity Parameters				
21	RV Offset, γ (km s^{-1})	-27.784	-27.810	-0.113	$+0.098$
22	RV Jitter, $\sigma_{\rm RV}$ (km s^{-1})	0.01	0.17	-0.11	$+0.20$

Table 3.4 Derived parameters from the photometric-dynamic model. We adopt the "best-fit" values as the system's parameters. The reference epoch is $t_0 = 2,455,014.46543$ (BJD).

Parameter	Best-fit	50%	15.8%	84.2%
Bulk Properties				
Mass of Star A, M_A ($M_\odot$)	0.820	0.830	-0.014	$+0.015$
Mass of Star B, M_B ($M_\odot$)	0.5423	0.5472	-0.0073	$+0.0081$
Mass of Planet b, M_p ($M_\oplus$)	67.	51.	$-21.$	$+22.$
Radius of Star A, R_A ($R_\odot$)	0.7761	0.7725	-0.0096	$+0.0088$
Radius of Star B, R_B ($R_\odot$)	0.484	0.502	-0.021	$+0.027$
Radius of Planet p, R_p ($R_\oplus$)	4.347	4.352	-0.099	$+0.099$
Density of Star A, ρ_A (g cm^{-3})	1.755	1.799	-0.049	$+0.066$
Density of Star B, ρ_B (g cm^{-3})	4.77	4.32	-0.63	$+0.58$
Density of Planet, ρ_p (g cm^{-3})	3.2	2.4	-1.0	$+1.0$
Gravity of Star A, $\log g_A$ (cgs)	4.5721	4.5811	-0.0086	$+0.0108$
Gravity of Star B, $\log g_B$ (cgs)	4.802	4.774	-0.046	$+0.036$
Orbital Properties				
Semimajor Axis of Stellar Orbit, a_{bin} (AU)	0.10148	0.10185	-0.00052	$+0.00057$
Semimajor Axis of Planet, a_p (AU)	0.3553	0.3566	-0.0018	$+0.0020$
Eccentricity of Stellar Orbit, e_{bin}	0.0365	0.0366	-0.0021	$+0.0023$
Argument of Periapse Stellar Orbit, ω_{bin} (Degrees)	279.74	279.71	-0.58	$+0.62$
Eccentricity of Planetary Orbit , e_p	0.1181	0.1185	-0.0017	$+0.0018$
Argument of Periapse Planet Orbit, ω_p (Degrees)	94.6	93.6	-2.3	$+2.2$
Mutual Orbital Inclination, Δi (deg)†	4.073	4.121	-0.083	$+0.113$

†: $\cos(\Delta i) = \sin(i_{bin})\sin(i_p)\cos(\Delta\Omega) + \cos(i_{bin})\cos(i_p)$

Table 3.5 Mid-transit times, depths and durations of the planetary transits.

Event #	Center (Time-2455000 [BJD])	σ (Center)	Depth† [ppm]	σ (Depth)	Duration [days]	σ (Duration)	Center (Time-2455000 [BJD])	Duration [days]
Observed							**Predicted**	
1	-4.3799	0.0019	1557	668	0.1517	0.0113	-4.38	0.14
2	62.3363	0.0018	2134	537	0.18	0.0138	62.34	0.18
3	125.0938	0.0033	2958	678	0.1549	0.0145	125.1	0.16
–	–	–	–	–	–	–	188.34††	0.1
4	963.1529	0.0045	2662	406	0.1551	0.0209	963.16	0.16
5	1026.1544	0.0037	2376	381	0.1083	0.0062	1026.16	0.12
6	1092.3978	0.0075	2759	322	0.3587	0.0199	1092.40	0.36
7	1156.2889	0.0057	1892	394	0.0921	0.0144	1156.29	0.1
8	1219.5674	0.0084	3282	432	0.2149	0.0236	1219.56	0.22
Future								
9	–	–	–	–	–	–	3999.47	0.12

†: in terms of $(\frac{r_p}{r_A})^2$

††: Predicted transit, difficult to be detected in the data

Chapter 4

Conclusions

Here we summarize the highlights of our work, and draw directions for future research.

4.1 Summary

In Chapter 2 we report the discovery and characterization of the transiting circumbinary planet Kepler-64b. The system is a detached eclipsing binary composed of two $M_A = 1.47\ M_{Sun}$ and $M_B = 0.37\ M_{Sun}$ stars on an eccentric ($e_{binary} = 0.2$), $\sim$ 20-day orbit, hosting a $r_p = 0.52\ R_{Jupiter}$ planet revolving around them every $\sim$ 138 days. Additionally, we outline our independent discovery of the circumbinary planets Kepler-47bc. After their announcement by Orosz et al. (2012a) we confirmed their results, then discontinued our analysis. We present the results from our ground-based spectroscopic observations aimed at obtaining the radial velocity of the host binary stars, measure the radial velocity of Kepler-

64 directly from its light curve with the Doppler beaming technique (demonstrating its potential for complementary analysis), and numerically show the dynamical stability of Kepler-64b. We note that Kepler-64 is a single-lined spectroscopic binary, which allows for determining the mass function of the binary but not the individual stellar masses.

Traditional transit-searching methods are designed for finding periodic signals in the light curves of single-star system. Thus, they are hard-pressed to detect the aperiodic circumbinary transits, which vary in time, duration, and depth, all of which depend on the phase of the binary star. Typically, consecutive transits of a circumbinary planet can deviate from linear ephemeris be several days, and their duration can vary from one transit to the next by a factor of a few. To tackle this obstacle, we invented a semi-automatic procedure tailored to finding individual transits. We use the procedure to search for such aperiodic transits in the *Kepler* catalog of detached eclipsing binaries, discuss the implications of the peculiar signature of transiting circumbinary planets for their confirmation and characterizations, and describe the analytic model we developed to estimate the individual masses of the two components of the binary star. Finally, to account for the many parameters required for a comprehensive description of the Kepler-64 system (e.g. masses, sizes, orbital elements), we build a photometric-dynamic model based on an N-body numerical integrator. For simplicity, we restrict the system to co-planarity.

Chapter 3 presents our discovery of Kepler-413b – a slightly misaligned ($\Delta i \sim 4^\circ$), $r_p = 4.4\,R_{Earth}$, transiting circumbinary planet orbiting a $\sim$ 10-day *Kepler* eclipsing binary. The binary is composed of a K and an M star with masses of $M_A = 0.84\,M_{Sun}$ and $M_B =$

0.54 M_{Sun} respectively, and has negligible eccentricity. The planet completes one orbit in $\sim$ 66 days and, due to fast orbital precession ($\sim$ 11 years), does not transit every inferior conjunction. The observational consequence of this is that *Kepler* observed two sets of consecutive transits (three and five respectively) separated by $\sim$ 800 days. At the time of writing, Kepler-413b is the only known transiting circumbinary system where the planetary orbit is more eccentric than that of the host binary ($e_{planet} = 0.12$, $e_{binary} = 0.04$).

We describe our spectroscopic and photometric observations of the system, determine the parameters of the binary star system (e.g. mass function, eccentricity) and the photometric contamination inside the *Kepler* aperture of the target. Like Kepler-64, Kepler-413 is also a single-lined spectroscopic binary. Statistical estimates, based on the presence of a spatially-resolved, nearby companion star in the central pixel, suggest that Kepler-413 is a triple stellar system. To accommodate the peculiar orbital configuration of the circumbinary planet Kepler-413b and account for its infrequent transits, we update our analytic model by allowing for variable impact parameters between different transits, and our photodynamic model by relaxing the co-planarity restriction. Additionally, we suggest that Kepler-413b may experience Cassini-States dynamics where its spin- and orbital-precession rates could be similar, and the obliquity of the planet may be closely aligned with the binary's orbit normal. Finally, we outline the fluctuations of the stellar flux incident on the circumbinary planet caused by its orbital motion, and note that although Kepler-413b is too close to its host binary for habitability (ignoring the planet's size), it is inside the dry desert habitable zone.

As important as our discoveries are to indulge our basic human curiosity about distant worlds, their main significance is for better understanding the inner workings of planetary systems. The orbital parameters of circumbinary planets (e.g. period, eccentricity, inclination, precession rate), for example, provide insight into the properties of protoplanetary disks, and shed light on planetary migration in the dynamically-rich environments of binary stars. More generally, the results of our work provide strong observational tests in terms of a) *origin* – formation, stability and evolution of planets in multiple stellar systems; b) *Galactic context* – host star characteristics; occurrence frequency of circumbinary planets; and c) $life$ – exploring the habitability of binary stars

4.2 Future work

To draw conclusions for the general characteristics of circumbinary planets based on the still small sample may be tempting, but it is premature. The host systems of the known transiting circumbinary planets are an important, but not representative subset of the *Kepler* eclipsing binary catalog: $\sim$2/3 of all catalog members have orbital periods smaller than 7.5 days; $\sim$ 50% have orbital periods less than 2 days. Intuitively, we'd would expect that finding transiting circumbinary planets around short-period eclipsing binaries should be easier compared to circumbinary planets in longer-period eclipsing binaries. Assuming circumbinary planets in short-period eclipsing binaries abide by the theoretical considerations (co-planarity, proximity to the dynamical stability limit), they will exhibit more transits per

unit time by being on shorter orbits. Yet no such planets have been detected at the time of writing. This apparent paucity of CBPs in short-period EBs could be due to a detection bias, i.e. they are harder to find as the light curves of their host EBs are more difficult to analyze (stronger intrinsic variability, more stellar eclipses per unit time). Alternatively, the bias could be astrophysical, due to complex formation and evolution history of the host system (the CBPs are either misaligned, or on longer orbits, or were ejected from the system, or were never formed). Our future plans are to address the detection bias by searching for transiting CBPs in the short-period *Kepler* EB catalog.

Bibliography

Adams, E. R., Ciardi, D. R., Dupree, A. K. et al. 2012, ApJ, 144, 42

Alexander, R. 2012, ApJ, 757, 29

Allard, F., Hauschildt, P. H., Alexander, D. R. et al. 2001, ApJ, 556, 357

Allard, F., Homeier, D., & Freytag, B. 2011, ASPC, 448, 91

Alonso, R., Brown, T. M., Torres, G., et al. 2004, ApJ, 613, 153

Anderson, D. R., Hellier, C., Gillon, M. et al. 2010, ApJ, 709, 159

Apai, D., Janson, M., Moro-Martín, A. et al., 2008, ApJ, 672, 1196

Apai, D., Radigan, J., Buenzlu, E. et al. 2013, ApJ, 768, 121

Armstrong, D. J., Osborn, H., Brown, D. et al. 2014, eprint arXiv:1404.5617

Artigau,É., Bouchard, S., Doyon, R., & Lafrenieѐre, D. 2009, ApJ, 701, 1534

Asay-Davis, X. S., Marcus, P. S., Wong, M. H., & de Pater, I. 2009, Icarus, 203, 164

BIBLIOGRAPHY

Bakos, G. Á., Noyes, R. W., Kovaćs, G., et al. 2004, PASP, 116, 266

Bailer-Jones, C. A. L. & Mundt, R. 1999, A&A, 348, 800

Bailer-Jones, C. A. L. & Mundt, R. 2001, A&A, 367, 218

Bailer-Jones, C. A. L. 2004, A&A, 419, 703

Bailer-Jones, C. A. L. 2008, MNRAS, 384, 1145

Baines, K. H., Drossart, P., Momary, T. W. et al. 2005, Earth Moon and Planets, 96, 119

Baraffe, I., Chabrier, G., Barman, T. S., et al. 2003, A&A, 402, 701

Baranec, C., et al. 2013, J. Vis. Exp. (72), e50021, doi:10.3791/50021

Baranne, A., Queloz, D., Mayor, M., et al. 1996, A&A, 119, 373

Barbieri, M., et al. 2007, A&A, 476, L13

Barman, T. S., Macintosh, B., Konopacky, Q. M., & Marois, C. 2011a, ApJ, 733, 65

Barman, T. S., Macintosh, B., Konopacky, Q. M., & Marois, C. 2011b, ApJ, 735, 39

Barnes, J. W., & Fortney, J. J. 2003, ApJ, 588, 545

Barnes, J. W., Linscott, E., & Shporer, A. 2011, ApJS, 197, 10

Barrado-Izagirre, N., Peŕez-Hoyos, S., & Sańchez-Lavega, A. 2009, Icarus, 202, 181

Beatty, T. G., Pepper, J., Siverd, R. J., et al. 2012, ApJ, 756, 39

BIBLIOGRAPHY

Bell, J., III, & Borucki, W. J. 1995, ASPC, 74, 165

Bender, C. F., Mahadevan, S., Deshpande, R., et al. 2012, ApJ, 751, L31

Beuermann, K., Hessman, F. V., Dreizler, S. et al. 2010, A&A, 521, 60

Beuermann, K., Buhlmann, J., Diese, J. et al. 2011, A&A, 526, 53

Beuermann, K., Dreizler, S., Hessman, F. V., Deller, J. 2012, A&A, 543, 138

Birkby, J., Nefs, B., Hodgkin, S. et al. 2012, MNRAS, 426, 1507

Bloemen, S., Marsh, T. R., Østensen, R. H., et al. 2011, MNRAS, 410, 1787

Bloemen, S., Marsh, T. R., Degroote, P., et al. 2012, MNRAS, 422, 2600

Boisnard, L., & Auvergne 2004, CoRoR mission engineering, IAC-04-IAF-Q.1.01

Bond I. A., et al. 2004, ApJ, 606, 155

Bonnefoy, M., Lagrange, A.-M., Boccaletti, A.,et al. 2011, A&A, 528, 15

Borkovits, T., Derekas, A., Kiss, L. L. et al. 2012, MNRAS, 428,1656

Borucki, W. J., & Summers, A. L. 1984, Icarus, 58, 121

Borucki, W. J., Koch, D. G., Basri, G. et al. 2010, Science, 327, 977

Borucki, W. J., Koch, D. G., Batalha, N., et al. 2012, ApJ, 745, 120

Borucki, W. J., Agol, E., Fressin, F., et al. 2013, Science, 340, 587

BIBLIOGRAPHY

Boyajian, T. S., von Braun, K., van Belle, G. et al. 2012, ApJ, 757, 112

Bouchy, F., Hébrard, G., Udry, S., et al. 2009, A&A, 505, 853

Brown, T. M., Latham, D. W., Everett, M. E., & Esquerdo, G. A. 2011, AJ, 142, 112

Burgasser, A. J., Wilson, J. C., Kirkpatrick, J. D., et al. 2000, AJ, 120, 1100

Burgasser, A. J., Marley, M. S., Ackerman, A. S., et al. 2002, AJ, 571, 151

Burgasser, A. J. 2009, AIPC, 1094, 501

Burke, C. J., Gaudi, B. S., DePoy, D. L., & Pogge, R. W. 2006, AJ, 132, 210

Burke, C. J.; Bryson, S.; Christiansen, J., et al. 2013, AAS, 221, 216

Burrows, A., Sudarsky, D., & Hubeny, I. 2006, ApJ, 640, 1063

Burrows, A. 2006, ASPC, 414, 115

Carter, B. D., Butler, R. P., Tinney, C. G., et al. 2003, ApJ, 593, 43

Carter, J. A., & Winn, J. N. 2010, ApJ, 716, 850

Carter, J. A., et al. 2011, Science, 331, 562

Carter, J., Agol., E. 2013, ApJ, 765, 132C

Chabrier, G., Baraffe, I., Allard, F., & Hauschildt, P. 2000, ApJ, 542, 464

Charbonneau, D., Brown, T. M, Latham, D. W., & Mayor, M. 2000, ApJ, 529, 45

BIBLIOGRAPHY

Chauvin, G., Lagrange, A.-M., Dumas. C. et al. 2004, A&A, 425, 29

Choi, J., McCarthy, C., Marcy, G. W. et al. 2013, ApJ, 764, 2

Cincotta, P. M., & Simó, C. 2000a, CMDA, 73, 195

Cincotta, P. M., & Simó, C. 2000b, ApJS, 147, 205

Cincotta, P. M., Giordano, C. M., & Simó, C. 2003, Physica D, 182, 151

Clampin, M. 2008, Advances in Space Research, 41, 1983

Clanton, C. 2013, ApJ, 768, 15

Claret, A. 2000, A&A, 363, 1081

Claret, A., & Bloemen, S. 2011, A&A, 529, 75

Clarke, F. J., Hodgkin, S. T., Oppenheimer, B. R., et al. 2008, MNRAS, 386, 2009

Cochran, W. D., & Hatzes, A. P. 2003, in IAU Symp. 202, Planetary Systems in the Universe: Observation, Formation, and Evolution, ed. A. J. Penny, P. Artymowicz, A.-M. Lagrange, and S. S. Russell, ISBN: 1-58381-176-1

Cowan, N. B., Agol, E., Meadows, V. S., et al. 2009, ApJ, 700, 915

Croll, B., Albert, L., Jayawardhana, R., et al. 2011, ApJ, 736, 78

Currie, T., Burrows, A., Itoh, Y., et al. 2011, ApJ, 729, 128

Currie, T., Debes, J., Rodigas, T. J., et al. 2012, ApJ, 760, 32

BIBLIOGRAPHY

Currie, T., Daemgen, S., Debes, J., et al. 2014, ApJ, 780, 30

Cushing, M. C., Roellig, T. L., Marley, M. S., et al. 2006, ApJ, 648, 614

Deeg, H.-J., Doyle, L. R., Kozhevnikov, V. P., et al. 1998, A&A, 338, 479

Deeg, H. J., Ocana, B., Kozhevnikov, V. P., et al. 2008, A&A, 480, 563

Dekany, R. G., Britton, M. C., Gavel, D. T., et al. 2004, SPIE, 5490, 879

Demarque, P., Woo, J-H, Kim, Y-C, & Yi, S. K. 2004, ApJS, 155, 667

Désert, J.-M., Bean, J., Miller-Ricci Kempton, E., et al. 2011, ApJ, 731, 40

Díaz, R. F., Damiani, D., Deleuil, M., et al. 2013, A&A, 551, L9

Dirk, R. & Holmberg, E. 1943, ApJ, 97, 41

Doyle, L. R. et al. 2000, ApJ, 535, 338

Doyle, L. R., & Deeg, H.-J. 2004, IAUS, 213, 80

Doyle, L. R., Carter, J. A., Fabrycky, D. C., et al. 2011, Science, 333, 6049

Duquennoy, A., & Mayor, M. 1991, A&A, 248, 485

Dvorak, R. 1982, Oesterreichische Akademie Wissenschaften Mathematisch naturwissenschaftliche Klasse Sitzungsberichte Abteilung, 191, 423

Dvorak, R. 1986, A&A, 167, 379

BIBLIOGRAPHY

Dvora, R., Froeschle, Ch., & Froeschle, Cl. 1989, A&A, 226, 335

Dyudina, U. A., Ingersoll, A. P., Danielson, G. E., et al. 2001, Icarus, 150, 219

Eggleton, P. P., & Kiseleva-Eggleton, L. 2001, ApJ, 562, 1012

Eggleton, P. P., & Tokovinin, A. A. 2008, MNRAS, 389, 869

Fabrycky, D. C., & Tremaine, S. 2007, ApJ, 669, 1289

Fabrycky, D. C.,Johnson, E. T.; Goodman, J. 2007 ApJ, 665, 754

Facchini, S., Ricci, L., & Lodato, G. 2014, MNRAS, eprint arXiv:1406.2708

Fischer, D. A., Howard, A. W., Laughlin, G. P., et al. 2014, "Exoplanet Detection Techniques" in Protostars and Planets VI, edited by Henrik Beuther; Ralf S. Klessen; Cornelis P. Dullemond; Thomas Henning;

Fortney, J. J., Marley, M. S., Saumon, D., & Lodders, K.. 2008, ApJ, 683, 1104

Fortney, J. J., Shabram, M., Showman, A. P., et al. 2010, ApJ, 709, 1396

Fossey, S. J., Waldmann, I. P., & Kipping, D. M. 2009, MNRAS, 396, 16

Foucart, F., & Lai, D. 2013, ApJ, 764, 106

Foucart, F., & Lai, D. 2014, eprint arXiv: 1406.3331

Fressin, F., Torres, G., Rowe, J. F., et al. 2012, Nature, 482, 195

Fressin, F., Torres, G., Charbonneau, D., et al. 2013, ApJ, 766, 81

BIBLIOGRAPHY

Gardner, J. P., Mather, J. C., Clampin, M., et al. 2006, Space Sci. Rev., 123, 485

Garufi, A., Quanz, S. P., Avenhaus, H. et al. 2013, A&A, 560, 105

Gatewood, G., & Eichhorn, H. 1973, AJ, 78, 769

Gaudi, B. S. 2012, ARA&A, 50, 411

Gelino, C. & Marley, M. 2000, ASPC, 212, 322

Gilliland, R. L., Chaplin, W. J., Dunham, E. W. et al. 2011, ApJS, 197, 6

Giant Magellan Telescope Science Case 2006, http://gmto.as.utexas.edu/

Goldman, B. 2005, AN, 326, 1059

Goździewski, K., Bois, E., Maciejewski, A. J., & Kiseleva-Eggleton, L. 2001, A&A, 378, 569

Goździewski, K. 2003, A&A, 398, 315

Goździewski, K., Breiter, S., Borczyk, W. 2008, MNRAS, 383, 989

Goździewski, K., et al. 2012, MNRAS, 425, 930

Green, J. J., Beichman, C., Basinger, S. A., et al. 2005, SPIE, 5905, 185

Hairer, E., Norsett, S., & Wanner, G. 1993, Solving ordinary differential equations I, nonstiff problems, 2nd Ed., Springer Series in Computational Mathematics (Springer-Verlag)

Hamilton, D. P., & Ward, W. R. 2004, ApJ, 128, 2510

BIBLIOGRAPHY

Harmanec, P. 1988, BAICz, 39, 329

Hébrard, G., Bouchy, F., Pont, F., et al. 2008, A&A, 488, 763

Hébrard, G., Amenara, J.-M, Santerne, A., et al. 2013, A&A, 554, A114

Heintz, W. D. 1988, JRASC, 82, 140

Heng, K. 2012, eprint arXiv:1304.6104

Herriot, G., Hickson, P., Ellerboek, B. L., et al. 2006, SPIE, 6272, 22

Higgins, C. A., Carr, T. D., & Reyes, F. 1996, GeoRL, 23, 2653

Hilditch, R. W. 2001, An Introduction to Close Binary Stars, by R. W. Hilditch, pp. 392. ISBN 0521241065. Cambridge, UK: Cambridge University Press, March 2001.

Hinse, T. C., Christou, A. A., Alvarellos, J. L. A., Goździewski, K. 2010, MNRAS, 404, 837

Hinse, T. C., Lee, J. W, Goździewski, K., Haghighipour, N., Lee, C.-U., Scullion, E. M. 2012, MNRAS, 420, 3609

Hinz, P. M., Rodigas, T. J., Kenworthy, M. A., et al. 2010, ApJ, 716, 417

Holman, M. J., & Wiegert, P. A. 1999, AJ, 117, 621

Horner, J., Marshall, J. P., Wittenmyer, & R. A., Tinney, C. G. 2011, MNRAS, 416, 11

Horner, J., Wittenmyer, R. A., Hinse, & T. C., Tinney, C. G. 2012a, MNRAS, 425, 749

BIBLIOGRAPHY

Horner, J., Hinse, T. C.,Wittenmyer, R. A., et al. 2012b, MNRAS427, 2812

Howard, A. W., Marcy, G. W., Johnson, J. A., et al. 2010, Science, 330, 653

Howard, A. W. 2013, Science, 340, 572

Howell, S. B., Sobeck, C., Haas, M., et al. 2014, PASP, 126, 398

Irwin, P. G. J. 2003, "Giant planets of our solar system : atmospheres, compositions, and structure", by P.G.J. Irwin. Springer Praxis books in geophysical sciences. Berlin: Springer

Jacob, W. S. 1855, MNRAS, 15, 228

Jaffe, D. T., Depoy, D. L., Fabricant, D. G., et al. 2010, SPIE, 7735, 72

Jenkins, J. M., et al. 2010a, ApJ, 713, 2

Jenkins, J. M., et al. 2010b, ApJ, 713, 87

Johns, M. 2008, SPIE, 6986, 3

Kane, S. R, & Hinkel, N. R. 2013, ApJ, 762, 7

Kasper, M., Apai, D., Janson, M., & Brandner, W. 2007, A&A, 472, 321

Kasper, M., Beuzit, J.-L., Vérinaud, C., et al. 2008, SPIE, 7015, 46

Kasper, M., Amico, P., Pompei, E., et al. 2009, The Messenger, 137, 8

Kasper, M., Beuzit, J.-L., Vérinaud, C., et al. 2010, SPIE, 7735, 81

BIBLIOGRAPHY

Kinemuchi, K., Barclay, T., Fanelli, M. et al. 2012, PASP, 124, 963

Kirk, B. et al. 2014, in prep.

Kiseleva, L. G., Eggleton, P. P., & Mikkola, S. 1998, MNRAS, 300, 292

Kley, W., & Haghighipour, N. 2014, A&A, 564, 72

Knapp, G. R., Leggett, S. K., Fan, X., et al. 2004, AJ, 127, 3553

Kopal, Z. 1955, AnAp, 18, 379

Kopparapu, R. K., Ramirez, R., & Kasting, J. F. et al. 2013, ApJ, 765, 2

Kratter, K. M., & Shannon, A. 2014, MNRAS, 437, 3727

Koch, D. G., Borucki, W. J., Basri, G. et al. 2010, ApJ, 713, 79

Kostov, V. B., McCullough, P. R., Hinse, T. C., et al. 2013, ApJ, 770, 52

Kostov, V. B., McCullough, P. R., Carter, J. A., et al. 2014, ApJ, 784, 14

Kostov, V. B., McCullough, P. R., Carter, J. A., et al. 2014b, ApJ, 787, 93

Kostov, V. B. et al. in prep.

Kovács, G., Zucker, S., & Mazeh, T. 2002, A&A, 391, 369

Kozai, Y. 1962, AJ, 67, 591

Lafrenière, D., Marois, C., Doyon, R., et al. 2007, ApJ, 660, 770

BIBLIOGRAPHY

Lafrenière, D., Jayawardhana, R., & van Kekwijk, M. H. 2010, ApJ, 719, 497

Lagage, P. O. & European MIRI Team 2010, In the Spirit of Lyot

Lagarde, N., Decressin, T., Charbonnel, C., et al. 2012, A&A, 543, A108

Lagrange, A.-M., Gratadour, D., Chauvin, G. et al. 2009, A&A, 493, 21

Lagrange, A.-M., Bonnefoy, M., Chauvin, G. et al. 2010, Science, 329, 57

Langton, J., & Laughlin, G. 2007, ApJ, 657, 113

Latham, D. W., Stefanik, R. P., Mazeh, T. et al. 1989, Nature, 339, 38

Lawrence, A., et al. 2007, MNRAS, 379, 1599

Lecavelier des Etang, A., Deleuil, M., Vidal-Madjar, A. et al. 1995, A&A, 299, 557

Lecavelier des Etang, A., Pont, F., Vidal-Madjar, A., & Sing, D. 2008, A&A, 481, 83

Lecavelier des Etang, A., Vidal-Madjar, A., Désert, J.-M., & Sing, D. 2008, A&A, 485, 865

Leggett, S. K., Geballe, T. R., Fan, X., et al. 2000, ApJ, 536, 35

Levrard, B.; Correia, A. C. M.; Chabrier, G. et al. 2007, A&A, 462,5

Lidov, M. L. 1962, P&SS, 9, 719

Lillo-Box, J., Barrado, D., & Bouy, H. 2012, A&A, 546, 10

BIBLIOGRAPHY

Liske, J., et al. 2011, The E-ELT Design Reference Mission, ESO publication E-TRE-ESO-080-0717, 2

Lissauer, J. J., Fabrycky, D. C., Ford, E. B., et al. 2011a, Nature, 470, 53

Lissauer, J. J., et al. 2011b, ApJS, 197, 8

Lissauer, J. J., Marcy, G. W., Rowe, J. F., et al. 2012, ApJ, 750, 112

Loeb, A., & Gaudi, B. S. 2003, ApJ, 588, L117

Macintosh, B., Troy, M., Doyon, R., et al. 2006, SPIE, 6272, 20

Macintosh, B. A., Graham, J. R., Palmer, D. W., et al. 2008, SPIE, 7015, 31

Madhusudhan, N., Burrows, A., & Currie, T. 2011, ApJ, 737, 34

Marcy, G. W., Butler, R. P., Williams, E., et al. 1997, ApJ, 481, 926

Marley, M. S., Saumon, D., & Goldblatt, C. 2010, ApJ, 723, 117

Mandel, K., & Agol, E. 2002, ApJ, 580, L171

Marois, C., Lafrenieѐre, D., Doyon, R., et al. 2006a, ApJ, 641, 556

Marois, C., Lafrenieѐre, D., Macintosh, B., & Doyon, R. 2006b, ApJ, 647, 612

Marois, C., Macintosh, B., Barman, T., et al. 2008, Science, 322, 1348

Marois, C., Zuckerman, B., Konopacky, Q. M., et al. 2010, Nature, 468, 1080

BIBLIOGRAPHY

Martin, R. G.; Armitage, P. J.; Alexander, R. D. 2013, ApJ, 773, 74

Martin, D. V., & Triaud, A. H. M. J. 2014, eprint arXiv:1404.5360

Marzari, F.; Thebault, P.; Scholl, H., et al. 2013, A&A, 553, 71

Matijevič, G., Prša, A., Orosz, J. A., et al. 2012, AJ, 143, 123

Mayor, M., & Queloz, D. 1995, Nature, 378, 355

Mayor, M. et al. 2011, eprint arXiv:1109.2497

Mazeh, T., Naef, D., Torres, G., et al. 2000, ApJ, 532, 55

Mazeh, T., & Faigler, S. 2010, A&A, 521, L59

McCarthy, Jr., D. W., Ge, J., Hinz, J. L., et al. 2001, PASP, 113, 353

McCullough, P. R., Stys, J. E., Valenti, J. A., et al. 2006, ApJ, 648, 1228

McLean, I. S. 1997, "Electronic imaging in astronomy. Detectors and instrumentation", Publisher: Chichester, UK Wiley, 1997, Series Wiley-PRAXIS series in astronomy and astrophysics. Published in association with Praxis Publishing, Chichester ISBN0471969710

McQuillan, A., Aigrain, S., & Mazeh, T. 2013, MNRAS, 432, 1203

McQuillan, A., Mazeh, T., & Aigrain, S. 2013, ApJ, 775, 11

Meixner, M., Smee, S., Doering, R. L., et al. 2010, PASP, 122, 890

BIBLIOGRAPHY

Mesa, D., Gratton, R., Berton, A., et al. 2011, A&A, 529, 131

Meschiari, S. 2012a, ApJ, 752, 71

Meschiari, S. 2012b, ApJ, 761, 7

Meschiari, S. 2013, eprint arXiv:1309.4679

Metchev, S. A. & Hillenbrand, L. A. 2006, ApJ, 651, 1166

Mikkola, S., & Innanen, K., 1999, CMDA, 74, 59

Miller-Ricci Kempton, E., Zahnle, K., & Fortney, J. J. 2012,ApJ, 745, 3

Mohanty, S., Jayawardhana, R., Hueĺamo, N., & Mamajek, E. 2007, ApJ, 657, 1064

Morales-Calderón, M., Stauffer, J. R., Kirkpatrick, J. D., et al. 2006, ApJ, 653, 1454

Morton, T. D., & Johnson, J. A. 2011, ApJ, 738, 170

Murray, C. D., & Correia, A. C. M. 2011, Exoplanets, edited by S. Seager. Tucson, AZ: University of Arizona Press, 2011, 526 pp. ISBN 978-0-8165-2945-2., p.15-23

Muterspaugh, M. W., Lane, B. F., Kulkarni, S. R. et al. 2010, AJ, 140, 1657

Nutzman, P., & Charbonneau, D. 2008, PASP, 120, 317

Nutzman, P. A., Fabrycky, D. C., & Fortney, J. J. 2011, ApJ, 740, L10

Oppenheimer, B. R., Digby, A. P., Newburgh, L., et al. 2004, SPIE, 5490, 433

BIBLIOGRAPHY

Orosz, J. A., Welsh, W. F., Carter, J. A., et al. 2012a, Science, 337, 1511

Orosz, J. A., Welsh, W. F., Carter, J. A., et al. 2012b, ApJ, 758, 87

Orton, G., Ortiz, J. L., Baines, K., et al. 1996, Science, 272, 839

Paardekooper, S.-J., Leinhardt, Z. M., Thbault, P., & Baruteau, C. 2012, ApJ, 754, 16

Paczyński, B. 1971, ARA&A, 9, 183

Pál, A. 2012, MNRAS, 420, 1630

Patience, J., King, R. R., de Rosa, R. J., & Marois, C. 2010, A&A, 517, 76

Peale, S. J. 1969, AJ, 74, 483

Pejcha, O., Antognini, J. M., Shappee, B. J.,& Thompson, T. A. 2013, MNRAS, tmp.2074

Pepe, F., Mayor, M., Galland, F., et al. 2002, A&A, 388, 632

Pepe, F., Mayor, M., Rupprecht, G., et al. 2002b, The Messenger, 110, 9

Pickles, A. J. 1998, PASP, 110, 863

Prša, A., Batalha, N., Slawson, R. W., et al. 2011, AJ, 141, 83

Pierens, A., & Nelson, R. P. 2007, A&A, 472, 993

Pierens, A., & Nelson, R. P., 2008a, A&A, 478, 939

Pierens, A., & Nelson, R. P. 2008b, A&A, 482, 333

Pierens, A., & Nelson, R. P. 2008c, A&A, 483, 633

Pierens, A., & Nelson, R. P. 2013, A&A, 556, 134

Pollacco, D. L., Skillen, I., Collier, C. A., et al. 2006, 118, 1407

Postman, M., Brown, T., Sembach, K., et al. 2010, SPIE, 7731, 79

Potter, S. B., Romero-Colmenero, E., Ramsay, G. et al. 2011, MNRAS, 416, 2202

Qian, S.-B., Liu, L., Liao, W.-F., et al. 2011, MNRAS, 414, 16

Qian, S.-B., Liu, L., Zhu, L.-Y., et al. 2012a, MNRAS, 422, 24

Qian, S.-B., Zhu, L.-Y., Dai, Z.-B., et al. 2012b, ApJ, 745, 23

Quanz, S. P., Meyer, M. R., Kenworthy, M. A., et al. 2010, ApJ, 722, 49

Queloz, D., Mayor, M., Weber, L., et al. 2000, A&A, 354, 99

Quillen, A. C.; Bodman, E.; Moore, A. 2013, MNRAS, 435, 3

Quintana, E. V., & Lissauer, J. J. 2006, Icarus, 185, 1

Quintana, E., V., Barclay, T., Raymond, S. N., et al. 2014, Science, 344, 277

Radigan, J., Jayawardhana, R., Lafrenieѐre, D., et al. 2012, ApJ, 722, 49

Rafikov, R. 2013, ApJ, 764, 16

Raghavan, D.; McAlister, H. A.; Henry, T. J. et al. 2010, ApJS, 191, 1

BIBLIOGRAPHY

Rappaport, S., Levine, A., Chiang, E., et al. 2012, ApJ, 752, 1

Rappaport, S., Deck, K., Levine, A., et al. 2013, ApJ, 768, 33

Rogers, J. H. 2008, JBAA, 118, 14

Rogers, L. A. & Seager, S. 2010, ApJ, 716, 1208

Russell, H. N. 1906, ApJ, 24, 1

Russell, H. N. 1948, Harvard Observatory Monographs, 7, 181

Rybicki, G.B., & Lightman, A. P. 1985, *John Wiley & Sons, ISBN-10: 0471827592*

Sahu, K. C., Casertano, S., Bond, H. E. et al. 2006, Nature, 443, 534

Santerne, A., Bonomo, A., S., Hébrard, G., et al. 2011, A&A, 536, A70

Sato, B., Ando, H., Kambe, E., et al. 2003, ApJ, 597, L157

Saumon, D. & Marley, M. S. 2008, ApJ, 689, 1327

Schneider, J., & Chevreton, M. 1990, A&A, 232, 251

Schneider, J. 1994, *P&SS*, 42, 539

Schneider, J., & Doyle, L. R. 1995, EM&P, 71, 153

Schneider, J. 2011, EPSC-DPS, p.3.

Schwamb, M. E., Orosz, J. A., Carter, J. A. et al. 2013, ApJ, 768, 127

BIBLIOGRAPHY

Seager, S., & Hui, L. 2002, ApJ, 574, 1004

Seager, S., & Malln-Ornelas, G. 2003, ApJ, 585, 1038

Seager, S. & Deming, D. 2010, ARA&A, 48, 631

Seager, S., & Lissauer, J. J. 2011, *E*xoplanets, edited by S. Seager. Tucson, AZ: University of Arizona Press, 2011, 526 pp. ISBN 978-0-8165-2945-2., p.3-13

See, T. J. J. 1896, AJ, 16, 17

Seiff, A., Kirk, D. B., Knight, T. C. D., et al. 1998, J. Geophys. Res., 1032, 22857

Showman, A. P., Cho, J. Y.-K., & Menou, K. 2010, Atmospheric Circulation of Exoplanets, Exoplanets, ed. S. Seager, 471

Sigurdsson, S., Richer, H. B., Hansen, B. M., et al. 2003, Science, 301, 193

Silva, A. V. R. 2003, Bulletin of the Astronomical Society of Brazil, 23, 15

Silva-Valio, A. 2008, ApJ, 683, L179

Skemer, A. J., Close, L. M., Szűcs, L., et al. 2011, ApJ, 732, 107

Skemer, A. J., Hinz, P. M., Esposito, S., et al. 2012, ApJ, 753, 14

Slawson, R. W., Prša, A. Welsh, W. F. et al. 2011, AJ, 142, 160

Słonina M., Goździewski K., Migaszewski C. 2012, in F. Arenou, & D. Hestroffer ed., Orbital Couples: Pas de Deux in the Solar System and the Milky Way

(arXiv:1202.6513v1,in print) Mechanic: a new numerical MPI framework for the dynamical astronomy

Słonina, M., Goździewski, K., Migaszewski, C., Rozenkiewicz, A. 2014, submitted to *New Astronomy*

Snyder, J. P. 1987, "Map Projections – A Working Manual", ed. Washington, D.C.: US Government Printing Office, 145

Southworth, J. 2012, Proceedings of the workshop "Orbital Couples: Pas de Deux in the Solar System and the Milky Way". Held at the Observatoire de Paris, 10-12 October 2011. Editors: F. Arenou, D. Hestroffer. ISBN 2-910015-64-5, p. 51-58

Sozzetti, A., Giacobbe, P., Lattanzi, M. G., et al. 2014, MNRAS, 437, 497

Stephens, D. C., Leggett, S. K., Cushing, M. C., et al. 2009, ApJ, 702, 154

Stiavelli, M. et al. 2008, "JWST Primer", Version 2.0, (Baltimore: STScI)

Still, M., & Barclay, T. 2012, Astrophysics Source Code Library, record ascl:1208.004

Struve, O. 1952, The Observatory, 72, 199

Sumi, T., Kamiya, K., Bennett, D. P. et al. 2011, Nature, 473, 349

ter Braak, C.J.F., & Vrugt, J.A. 2008, *Statistics and Computing* 16, 239

Tohline, J. E. 2002, ARA&A, 40, 349

BIBLIOGRAPHY

Tokovinin, A. A. 1993, Astronomy Letters, 23, 6

Torrence, C., & G.P. Compo, 1998, Bull. Amer. Met. Soc., 79, 61-78

Torres, G., Andersen, J., & Giménes, A. 2010, A&ARv, 18, 67

Tsuji, T. & Nakajima, T. 2003, ApJ, 585, 151

Vasavada, A. R. & Showman, A. P. 2005, Reports on Progress in Physics, 68, 1935

Vérinaud, C., Kasper, M., Beuzit, J.-L., et al. 2010, SPIE, 7736, 55

Vigan, A., Moutou, C., Langlois, M., et al. 2010, MNRAS, 407, 71

Udalski, A., Pietrzynksi, G., Szymanski, M., et al. 2003, Acta Astronomica, 53, 133

van Kerkwijk, M. H., Rappaport, S. A., Breton, R. P., et al. 2010, ApJ, 715, 51

van de Kamp, P. 1963, AJ, 68, 515

van de Kamp, P. 1969, AJ, 74, 757

van der Marel, N., van Dishoek, E. F., Bruderer, S. et al. 2013, Science, 340, 1199

Walker, Matthews, Kuschnig, et al., 2003, PASP, 115, 1023

Ward, W. R., & Hamilton, D. P. 2004, ApJ, 128, 2501

Weiss, L. M.; Marcy, G. W.; Rowe, J. F. et al. 2013, ApJ, 768, 1

Welsh, W. F.; Orosz, J. A.; Carter, J. A., et al. 2012, Nature, 481, 475

BIBLIOGRAPHY

Welsh, W. F. et al. 2014, in prep

West, R. A., Baines, K. H., Friedson, A. J., et al. 2004, "Jovian clouds and haze", in Jupiter. The Planet, Satellites and Magnetosphere, ed. Bagenal, F., Dowling, T. E., & McKinnon, W. B., 79

Westphal, J. A., Matthews, K., &Terrile, R. J. 1974, ApJ, 188, L111

Winn, J. N., & Holman, M. 2005, ApJ, 628, 159

Winn, J. N., Johnson, J. A., Fabrycky, D. A. et al. 2009, ApJ, 700, 32

Wolszczan, A., & Frail, D. A. 1992, Nature, 355, 145

Wolszczan, A. 1994, Science, 264, 538

Wittenmyer, R. A., Endl, M., Cochran, W. D. et al. 2006, ApJ, 132, 1

Wright, J. T., Fakhouri, O., Marcy, G. W., et al. 2011, PASP, 123, 412

Wright, J. T., & Gaudi, B. S. 2013, "Planets, Stars and Stellar Systems", by Oswalt, Terry D.; French, Linda M.; Kalas, Paul, ISBN 978-94-007-5605-2. Springer Science+Business Media Dordrecht

Zsom, A., Seager, S., de Wit, J., & Stamenkovic, V. 2013, ApJ, 778, 2

Appendix A

Mapping Directly Imaged Giant Exoplanets

Kostov, Veselin B. and Apai, Dániel, 2013, *The Astrophysical Journal*, **762**, 1

APPENDIX A. MAPPING DIRECTLY IMAGED GIANT EXOPLANETS

The quest to discover and characterize planets outside the Solar System is inherently multi-directional – depending on the targets being pursued, it involves a suite of different detection methods and analysis techniques, and a vast armada of instruments spread across the Earth and in space, all actively competing and at the same time complementary to each other. While the physical sizes of the planets discovered by the Kepler mission can be deduced, and the mass and temperature of a small subset of them can be estimated, they are all too far to be followed-up by current direct-imaging instruments, leaving us hard-pressed to study their atmospheric structure and composition. Such is not the case, however, for extrasolar planets that are close enough (and bright too) to be amenable for photometric and spectroscopic observations. As we argue below, the next generation of adaptive-optics instruments (some already in the process of deployment, i.e. VLT/SPHERE and Gemini/GPI) will be capable of characterizing the atmospheric appearance and composition of directly-imaged, giant extrasolar planets through observations of rotationally-modulated photometric and spectroscopic variations caused by patchy, cloudy atmospheres (like Jupiter's). Building on the legacy of Kepler, future planet-hunting missions like TESS will provide an abundance of nearby planets, some of which would be appropriate targets for the observations and analysis we suggest below.

Abstract

With the increasing number of directly imaged giant exoplanets the current atmosphere models are often not capable of fully explaining the spectra and luminosity of the sources. A particularly challenging component of the atmosphere models is the formation and properties of condensate cloud layers, which fundamentally impact the energetics, opacity, and evolution of the planets.

Here we present a suite of techniques that can be used to estimate the level of rotational modulations these planets may show. We propose that the time–resolved observations of such periodic photometric and spectroscopic variations of extrasolar planets due to their rotation can be used as a powerful tool to probe the heterogeneity of their optical surfaces. In this paper we develop simulations to explore the capabilities of current and next–generation ground– and space–based instruments for this technique. We address and discuss the following questions: a) what planet properties can be deduced from the light curve and/or spectra, and in particular can we determine rotation periods, spot–coverage, spot colors, spot spectra; b) what is the optimal configuration of instrument/wavelength/temporal sampling required for these measurements; and, c) can principal component analysis be used

to invert the light curve and deduce the surface map of the planet.

Our simulations describe the expected spectral differences between homogeneous (clear or cloudy) and patchy atmospheres, outline the significance of the dominant absorption features of H_2O, CH_4, and CO and provide a method to distinguish these two types of atmospheres. Assuming surfaces with and without clouds for most currently imaged planets the current models predict the largest variations in the J–band. Simulated photometry from current and future instruments is used to estimate the level of detectable photometric variations. We conclude that future instruments will be able to recover not only the rotation periods, cloud cover, cloud colors and spectra but even cloud evolution. We also show that a longitudinal map of the planet's atmosphere can be deduced from its disk–integrated light curves.

A.1 Introduction

Clouds play a fundamental but complex role in the atmospheres of brown dwarfs and exoplanets: describing their vertical and horizontal distributions, composition, formation and evolution are the outstanding challenges faced by models of ultracool atmospheres. Refractory minerals, such as Ca-Al-oxides, metallic iron and silicates, condense in the temperature range ∼1,300–1,900 K, forming clouds that dominate the atmospheres of L–type dwarfs and exoplanets of similar temperatures (e.g. Burrows , 2009; Fortney et al., 2008). These silicate clouds are responsible for their very red near-infrared colors (e.g. Burrows , 2009; Burgasser , 2009; Marley et al., 2010). Silicate grains, for example, have already been observed with Spitzer (Cushing et al., 2006), supporting this assumption. In contrast, the spectrum of cooler T–dwarfs is markedly different — it is characterized by blue near-infrared colors and is dominated by the absorption of stable gas–phase H_2O and CH_4. The spectra of T dwarfs are explained by clear, i.e. non-cloudy, models. The depletion of refractory elements at the L/T–transition regime (at temperatures of ∼1,000 to 1,200 K), caused by their ”rain out” to deeper, hotter layers (Burrows , 2009; Burgasser , 2009; Allard et al., 2011) results in a strong change in the spectrum which, combined with the cloud dispersal assumption, is the proposed mechanism for the onset of the T–dwarf regime.

Although the loss of cloud opacity at the L/T transition is qualitatively consistent with the drastic changes observed in the spectra, the process leading to the loss of clouds has not yet been identified. At least two different ideas have been explored. One plausible

mechanism, supported by the work of Knapp et al. (2004) and Tsuji & Nakajima (2003), proposes a thinning (or even complete dissipation) of the global cloud cover, caused by the growth and subsequent sinking to deeper layers of the cloud particles. Another possibility, motivated in part by visible and near-infrared observations of Jupiter (Westphal et al., 1974; Orton et al., 1996; Dyudina et al., 2001) and by near-infrared Cassini/VIMS observations of Saturn (Baines et al., 2005), proposes a sudden appearance of clear, optically thin "holes" in the global cloud deck (Burgasser et al., 2002; Marley et al., 2010, and others). In this scenario, in objects close to the L/T transition flux from deeper, hotter regions can escape through these holes. Therefore the atmosphere will appear patchy with bright, hot and deep regions next to cooler, optically thick higher–altitude ones. Both scenarios can produce similar near-infrared colors at the L/T transition by varying different parameters – temperature, surface gravity, sedimentation efficiency and/or grain size for the former and cloud-cover and distribution for the latter (Saumon & Marley, 2008). The predicted differences are subtle which, when combined with the uncertainty in the measured temperature, currently makes it difficult to distinguish these models (Marley et al., 2010). For example, models that can explain the observed broadband photometry of L/T brown dwarfs do not guarantee a proper match for their near-infrared spectra (Burrows et al., 2006). This was clearly shown for the case of HR8799b (e.g. Barman et al., 2011a), where the broad band photometry is well matched to an L6 dwarf while the near-IR spectrum is not.

The differences found between the spectra of individual L/T transition objects and the model predictions, while difficult to explain, are not surprising as the current models do

not account for the possibly complex three-dimensional atmospheres and large-scale atmospheric circulations, which also set the appearance of Jupiter. Therefore, explaining the atmospheric properties of the L/T dwarfs and giant exoplanets of similar temperatures, will likely require more than one-dimensional information. Understanding the spectra of these ultra cool atmospheres will require a physical model not only for the formation, evolution, and destruction of cloudy regions, but also for their longitudinal/latitudinal and vertical distributions.

Not surprisingly, clouds also represent a key problem in the atmospheres of giant exoplanets of similar temperatures. Many of the recently discovered, directly imaged exoplanets fall in the temperature regime of the L/T transition: HR8799 bcde with T$\sim$1,000K (e.g. Marois et al., 2010) and β Pictoris with T$\sim$1,500K (Lagrange et al., 2009; Quanz et al., 2010; Skemer et al., 2012). These planets are cooler than Hot Jupiters ($\sim 1,500-2,400$ K, Seager & Deming 2010), but much hotter than the effective temperature of Jupiter ($\sim$ 200K, Seiff et al. 1998). While directly–imaged planets may differ from brown dwarfs in bulk chemical composition, surface gravity and formation mechanism, their atmospheric physics is thought to be very similar.

The need for understanding cloud properties became even more pressing with the realization that many directly imaged exoplanets are significantly under-luminous in the near-infrared bands compared to field brown dwarfs and some state-of-the-art models: HR8799b (e.g. Marois et al. (2010); Currie et al. (2011); Barman et al. (2011a); Skemer et al. (2012)); 2M1207b (Mohanty et al., 2007; Patience et al., 2010; Skemer et al., 2011). Interestingly,

β Pic b – a younger planet with estimated mass close to HR 8799b and 2M1207b – appears to align well with model predictions (Lagrange et al. , 2010; Quanz et al., 2010; Bonnefoy et al., 2011). In contrast, the prominent underluminosity of HR8799b and 2M1207b sparked intense theoretical work and most groups were led to propose cloud properties that differ significantly from those assumed for field brown dwarfs (Barman et al., 2011a,b; Madhusudhan et al., 2011; Skemer et al., 2012). Several groups found best photometric matches from a combination of thick and thin clouds and therefore argued for patchy atmospheres in the HR 8799 planets (e.g. Marois et al. (2008); Skemer et al. (2012)). For a more detailed discussion on the latest results we refer the reader to Section A.5.1.

While it appears that directly-imaged planets are not a new class of objects but a natural continuation of the L-dwarfs sequence (rather than of the T-dwarfs), these developments emphasized the need for developing a more realistic model for cloud properties which, in turn, demand new, multi-dimensional data. Photometric variations due to rotating, spectrally heterogenous objects have been proposed as a probe of the cloud properties in brown dwarfs (e.g. Bailer-Jones & Mundt (1999, 2001); Burgasser et al. (2002)). Similar observations of Earth from the EPOXI spacecraft were used to probe land mass and ocean distributions (Cowan et al., 2009). While the first searches for varying brown dwarfs produced several tentative detections, the past years brought the detection of periodic, rotational variations in L/T transition dwarfs (Artigau et al., 2009; Clarke et al., 2008; Radigan et al., 2012). For example, a newly discovered L/T transition brown dwarf shows a peak-to-peak near-infrared variation as large as 27% in the J–band (Radigan et al., 2012; Apai

et al., 2013). With short typical rotation periods (<10 hours) these sources reveal patchy cloud covers on brown dwarfs.

The best example of rotationally–induced photometric variability of a giant planet is, not surprisingly, in Jupiter. Using IRTF and HST mosaics Gelino & Marley (2000) simulated the photometric variability of an unresolved Jupiter due to its rotation. At 4.78 μm Jupiter indeed shows a very strong rotational modulation (up to 0.2 magnitudes), detectable at 0.41 μm as well on the level of 0.04 magnitudes. The culprit for these variations is the Great Red Spot which manifests itself as a large dark patch in the thermal infrared (where the directly imaged giant planets are bright). Thus, while not at the temperatures of the current census of directly imaged planets, Jupiter can be used as a reasonable starting point for studying their expected optical appearance.

The need for characterizing cloud properties, combined with the exciting new results on brown dwarf variability, and the strong indications of patchy dust clouds in directly imaged planets motivate our study to propose variability of directly–imaged giant exoplanets as a means for characterizing their cloud covers. We present here a model for the atmospheric appearance of a directly–imaged giant planet that can be easily modified to represent any scenario: clouds on a clear atmosphere, clear "holes" on a cloudy atmosphere, a global clear or cloudy atmosphere with cold and/or hot spots. Cold spots could represent cloud thickness/structrure variations and heterogeneity (Radigan et al., 2012) which would change the brightness of the respective patch so we included both possibilities. The goal of this paper is to explore the observational signatures of such heterogenous atmospheres on

directly–imaged giant planets. The choice of instrument, wavelength, and cadence of the observations are all target–dependent and not obvious. New instruments can be optimized for exploiting this technique, but this requires an understanding of the variations expected from the rotating giant planet targets. We also use the simulated lightcurves to deduce the longitudinal distribution of the eigencolors using principal component analyses and to recreate the longitudinal spot patterns of the input map.

Here we provide a framework for identifying specific photometric and spectroscopic signatures expected of future directly imaged giant planets. The paper is organized as follows. In Section A.2 we explain the details of our model. Our results are described in Section A.3. We present the deduced longitudinal map of the planet in Section A.4, discuss the key points in Section A.5 and draw our conclusions in Section A.6.

A.2 Model Description

We constructed a model to predict photometric and spectroscopic variations as a function of exoplanet rotation phase, wavelengths of the observations, and instrument/telescope. The key properties of the target are its effective temperature and inclination, and the temperature, spatial and size distribution of the spots. We use the contrast limits for the current and future instruments provided in the literature to simulate the relative photometric and spectroscopic accuracy. Our model first generates a 2D spot distribution for the exoplanet, determines the rotational modulations in the integrated lightcurve and spectrum as a func-

tion of wavelength, and then simulates the observations with the selected instrument. We explore the possibilities of this technique for giant planets to guide future observations and identify requirements for various instruments to inform their development.

We will first review and discuss the cloud model, then describe the spectral libraries we use and discuss the simulated observations.

A.2.1 Exoplanet Cloud Models

We model the spot distribution of the exoplanet with a combination of an ambient/mean spectrum, calculated for the effective temperature of the planet, and a set of elliptical spots with different temperatures. The spots can have any size, shape, spatial distribution, temperature, surface gravity, metallicity and covering fraction. In the following, when we speak about the features of our models we will refer to ”spots”, but clouds will be used in the context of the astrophysical objects in ultracool atmospheres.

As a guide for spot size and shape distribution we use Jupiter, our best yet imperfect analogue. As will be shown, the general results of this paper do not depend strongly on this choice or the specific cloud shape and distribution. The cloud pattern of Jupiter is described by latitudinal bands, correlated to zonal circulation (Vasavada & Showman, 2005). The visual appearance of Jupiter is dominated by ammonia clouds located between 250 *mbar* and 1 *bar* (West et al. 2004). Above them are hazes which are observed in the near–UV, while deeper atmospheric layers are probed outside methane bands in the near–IR (Barrado-Izagirre et al., 2009).

APPENDIX A. MAPPING DIRECTLY IMAGED GIANT EXOPLANETS

We set up our initial models to resemble the atmosphere of Jupiter, using elliptical spots with an aspect–ratio of 1.5, based on the Great Red Spot (GRS) – with dimensions of 12,400 km and 19,800 km it had an aspect ration of 1.59 in 2006 (Rogers, 2008). To emphasize the effect such a spot can have on the visual appearance of a giant planet, we note the size the GRS had a 100 years ago when its longitudinal extent was about 45,000 km (Irwin, 2003) and it covered about 3% of the total surface area of Jupiter. The largest attainable size of turbulent eddies, defined as the Rhines length, is a function of the atmospheric wind speed and the gradient of the Coriolis force (Showman et al., 2010) (Section 3.6, Equation 35), neither of which are constrained for giant planets. We note that the maximum size of spots present in planetary atmospheres is not necessary equivalent to the Rhines length, as the nature of such spots may be significantly more complicated than simple cyclonic eddies with different temperatures. It is not unreasonable to imagine a rather exotic situation where the vertical structure of the atmosphere is such that multiple, stratified layers of hazes and/or cloud layers with variable thickness alternate in such a way that they do or do not obscure deeper/hotter regions in the atmosphere. Nevertheless, the Rhines length provides a reasonable initial scale and we adopt it as the parameter setting the size of the largest spots.

For Jupiter, the Rhines scale is on the order of 10% the planet's radius. Atmospheric models of Hot Jupiters, however, have suggested the presence of very high wind speeds on the order of 1–3 km s^{-1}, (Showman et al., 2010) (Section 3.3, Table 1) and the possibility of much larger Rhines scale (comparable to the size of the planet). With a similar radius

to Jupiter and assuming comparable rotation rates but faster winds (between Jupiter's and those for the Hot Jupiters), the Rhines length for directly–imaged giant planets will be larger than that for Jupiter. As a consequence the largest spots may be larger. Thus, to construct our atmospheric map we use a single giant spot covering a 5% fraction of the total surface area and a set of additional, smaller spots, distributing their semi–major axes as a power-law of $D(N) = A \times 10^{-\alpha}$, where D is an array of N semi-major axes (one for each spot), A is a scale–factor (described below) and α is the power-law index. The total number of spots, the power–law index, the total spot–covering factor (f_c hereafter) and the spot aspect-ratio are free parameters in the model. For illustrative purposes, here we use N = 20 spots with $\alpha = 2.0$ and $f_c = 10\%$, in such a way that the largest 5 spots correspond to 85% of the "patchy" contribution. The choice of parameters is such that a single giant spot dominates most of the signal, a few smaller spots produce smaller, albeit still detectable signatures (as discussed below) while the rest of the spots are the tail of the power law and too small to be detectable. We use the scale-factor A to scale the sizes of the spots such that the total area covered by the sum of all spots is the predefined f_c, while keeping their relative sizes, as determined by the power-law size distribution, unchanged:

$$A = \frac{4\pi f_c}{\sum_{i=1}^{N} s_i} \tag{A.1}$$

where s_i is the surface area of the i_{th} spot.

To calculate what fraction of the surface the different spot types cover during the rotation, we first randomly distribute the spots on a sphere then project the hemisphere visible

for discrete rotational phases and finally measure the rotationally modulated fractional coverage for each spot. We use orthographic projection (Snyder, 1987), a technique that represents the actual appearance of a distant planet. It does not preserve the size or the shape of the surface features but as we are interested in the disk–integrated lightcurve and not in the best cartography of its surface, this transformation is well suited for our purposes. The projection is defined as (Snyder, 1987):

$$x = R\cos(\phi)\sin(\lambda - \lambda_0) \tag{A.2}$$

$$y = R[cos(\phi_1)\sin(\phi) - \sin(\phi_1)\cos(\phi)\cos(\lambda - \lambda_0)] \tag{A.3}$$

where x and y are the cartesian coordinates on the projected 2–dimensional map, λ and ϕ are longitude and latitude on the sphere, (λ_0, ϕ_1) are longitude and latitude of the center point of the projection and R is the radius of the sphere, which is unity in our model.

An example of the two projected hemispheres of the planet with an inclination of 0° is shown in Figure A.1, where the different colors correspond to different spots, as described in the figure. From this projected map we extract the rotationally modulated fractional coverage of each surface element as a function of the planet's period, phase angle and inclination as described above. Figure A.2 shows the contributions of the largest spots to the visible hemisphere as a function of rotational phase. The giant spot covers 21.5% of the projected visible hemisphere, while the next five spots by size cover between 2% and 4% each. We note that the relationship between the total surface fraction covered f_c and the surface fraction of each spot is a function of the inclination of the planet and the size

and shape of the spots.

In the next section we describe how these covering fractions are used to combine the spectra of all spots present on the hemisphere facing the observer for each rotation phase.

A.2.2 Spectra and Spectral Libraries

To each unique surface element ("spot") we assign a model spectrum from one of two different spectral libraries – (Burrows et al., 2006) (B06 hereafter) models or the AMES models of (Allard et al., 2001) (A01 hereafter). The free parameters of these model libraries are temperature, metallicity, $log(g)$ and cloudy or clear atmosphere. We combine the cloudy and the clear models from the same library, keeping the surface gravity and the metallicity constant for a given object. We note that this step implicitly assumes that the pressure-temperature distribution of each column of gas is independent of that of neighboring columns, a good first-order assumption, which is not strictly correct (Marley et al., 2010).

We explore objects with broad temperature range around the L/T transition (T $\sim$ 700 K to 1,400 K), representative of the giant self–luminous planets current and next–generation facilities are expected to directly image. Throughout the paper we use model spectra for solar metallicity and $log(g) = 4.5$ for simplicity. Model spectra for different temperature regimes for A01 (Cond) and B06 (both Clear and Cloudy) are shown in Figure A.3. The two Clear models are quite similar, the main difference being the more detailed features of A01. We note that the Cloudy B06 are significantly different from the Clear B06 both in

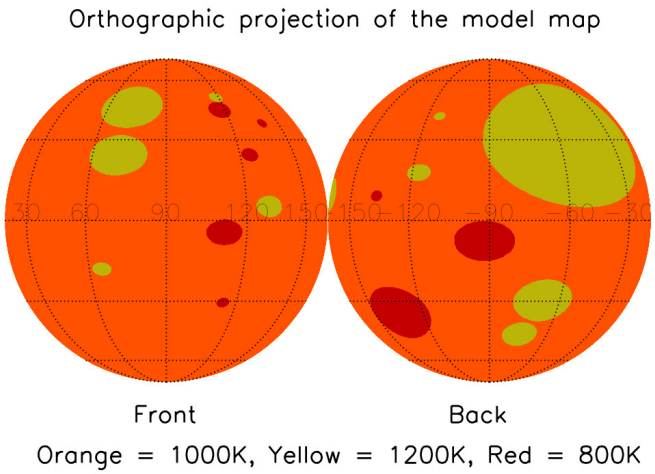

Figure A.1 Projected model atmospheric map of a giant planet with randomly distributed spots according to a power law with an index of –2.0 (such that the largest five clouds are responsible for 85% of the signal). Different colors correspond to different surface types temperatures, as indicated in the figure. This model has a 10% total spot–covering factor (the giant spot covers 5% of the total surface area), 3 different temperatures, and inclination of 0°. The left disk represents the front side of the planet facing the observer, the right disk – the back.

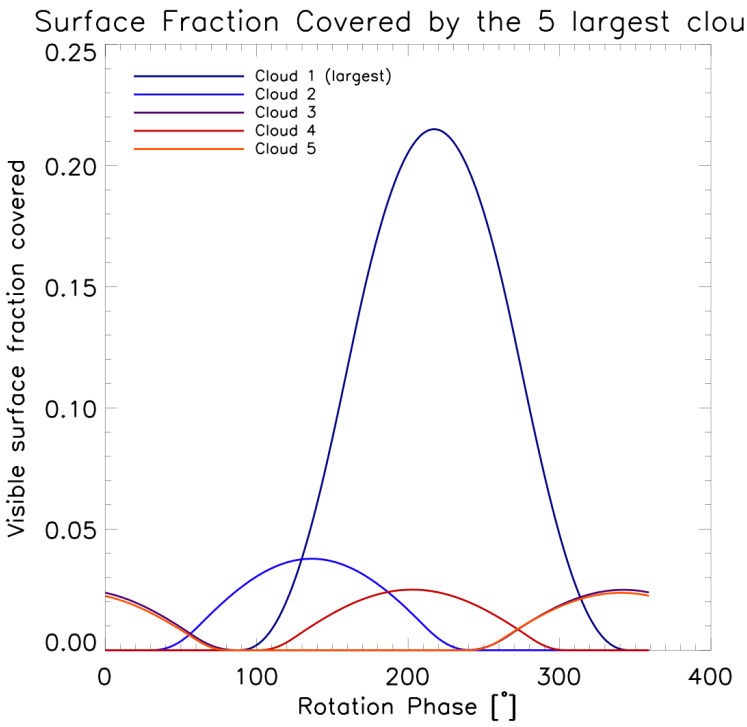

Figure A.2 The visible surface fraction covered by the 5 largest spots as a function of rotational phase for the map shown in Figure A.1.

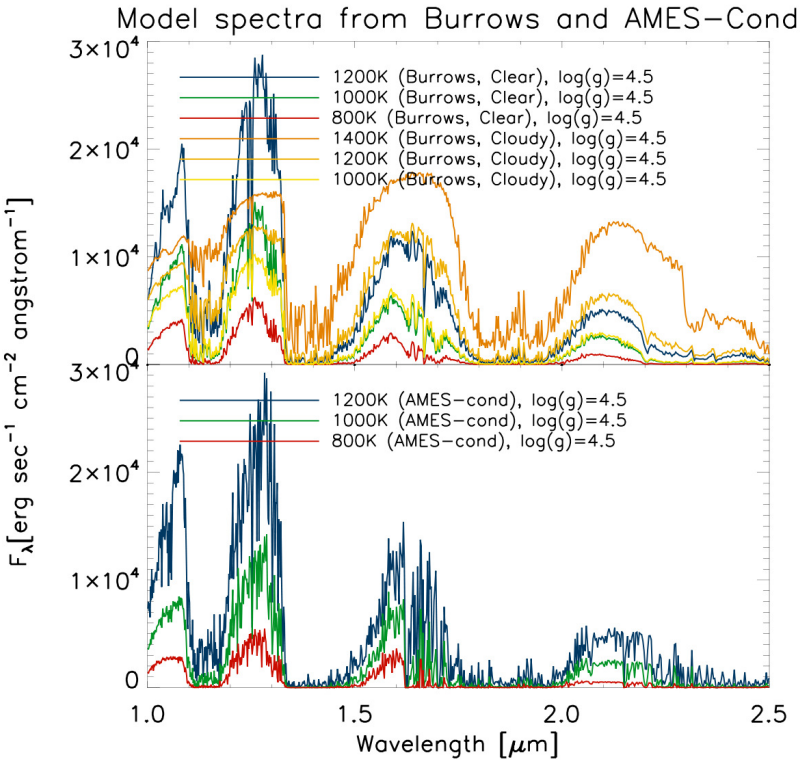

Figure A.3 Sample spectra for temperatures of 800K, 1000K and 1200K and log(g)=4.5 from the Clear Burrows (B06, top) and AMES-Cond (A01, lower) models.

the strength and in the shape of the spectra in all three filters shown in the figure, a feature that will be discussed in more details in the discussion section.

Next, the spectra of all spots present on the hemisphere facing the observer are weighted by their respective surface cover fraction and linearly combined for each rotation phase as:

$$F_{\lambda,tot} = \sum_{i=1}^{N} [F_{\lambda,i} \times f_{c,i}] \tag{A.4}$$

where $F_{\lambda,i}$ and $f_{c,i}$ are the flux density and covering factor respectively of each surface

element on the visible disk of the planet and N is the number of different surfaces on the visible disk. The photometry is calculated from the flux density by first normalizing the spectrum by the width of the different filters we explore and then integrating.

A.2.3 Simulated Observations

A.2.3.1 Targets and Instruments

As a target we assume a star and giant exoplanet resembling HR8799 c (at a distance of 40 parsec), with a rotation period of 4 hours (planet's apparent brightness: J = 17.65 mag, H = 16.93 mag, Ks = 16.33 mag, $T_{eff} = 1,000$ K around an A5V star with J = 5.38 mag, H = 5.28 mag and Ks = 5.24 mag, (Marois et al., 2008)). Correspondingly, the planet–to–star flux contrast ratio is $\sim 1.2 \times 10^{-5}$ in J–band, $\sim 2.2 \times 10^{-5}$ in H–band and $\sim 3.7 \times 10^{-5}$ in Ks–band.

We model four different setups representative to the current and next-generation facilities shown in Table A.1: an 8m–class telescope with Adaptive Optics (8m AO) representing VLT/NACO and Keck AO; an 8m–class telescope with an Extreme–AO (8m ExAO) representing VLT/SPHERE, Gemini/GPI, LBT/AO; a 30m–class telescope with Extreme AO (30m+ ExAO) representing Giant Magellan Telescope (GMT), Thirty Meter Telescope (TMT), Extremely Large Telescope (ELT)); and the James Webb Space Telescope (JWST). While these examples do not include all planned instruments, such as the Lyot 1800 project (Oppenheimer et al., 2004) or ATLAST (Postman et al., 2010), they bracket the range of

relevant instrument capabilities for the next two decades.

To estimate the achievable photometric accuracy of the different instruments we rely on the residual radial contrast curves provided by the instrument teams: VLT/NACO at 4 μm (Kasper et al., 2007, 2009), VLT/SPHERE in J–band (Vigan et al., 2010; Mesa et al., 2011), Gemini/GPI in H–band (Macintosh, et al., 2008), TMT/PFI in H–band (Macintosh, et al., 2006), ELT/EPICS in J–band (Kasper et al., 2008, 2010) and JWST/NIRCAM in K–band (Green et al., 2005). All contrast limits are for coronographic images. For VLT/NACO, VLT/SPHERE, Gemini/GPI and JWST/NIRCAM we place the planet at a separation of 1$''$, similar to the "c" planet in the HR8799bcde system (Marois et al., 2008). For the 30m–class telescopes we assume a separation of 0.2$''$, due to the smaller field-of-view of some of these instruments. The sensitivity limits for the four different instrument classes we explore are shown in Table A.2.

A.2.3.2 Synthetic Photometry and Spectroscopy

To explore our ability to recover surface details of giant exoplanets we create a set of simulated observations. Rotationally–modulated lightcurves in J, H and Ks–bands produced as described in Section A.2.2 for an exoplanet with an atmospheric map from Figure A.1 are used to simulate the flux from the planet measured by a suite of current and future instruments. Throughout this work we use the VLT/NACO filters defined with central wavelengths and widths (in μm) as follows: J–band (1.265 and 0.25 respectively); H–band (1.66 and 0.33); Ks–band (2.18 and 0.35), L' (3.8 and 0.62) and M' (4.78 and 0.59). The

actual filter transmission curves are available on the ESO instrument website.

Most state-of-the-art ground- and space-based high-contrast observations rely on relative instrument-sky rotations to separate faint point sources from instrument speckles. The ground-based version of this technique is often referred to as angular differential imaging (ADI) – a technique with a variety of implementations (e.g. Marois et al., 2006a; Apai et al., 2008; Kasper et al., 2007; Lafrenière et al., 2007). While a powerful method, ADI-type observations necessarily pose an important constraint on time-series observations. Because the observations rely on field rotation to separate real sources from speckles, for each independent photometric measurement a minimum field rotation rate per image (an upper limit on cadence) is required. We describe this by requiring the arc traced by the planet during the rotation to be larger than at least four times the full width at half maximum of the point spread function (PSF) to ensure that the planet's PSF is well separated from instrument speckles. To calculate the field rotation rate and time required by the ADI we follow the prescription of McLean (2001) (Chapter 3, equation 3.14) as follows:

$$\omega = \Omega \frac{\cos(A)\cos(\phi)}{\sin(z)} \tag{A.5}$$

$$f_{rot} = \frac{4\frac{\lambda}{D}}{r_{sep}} \tag{A.6}$$

where ω is the field rotation rate in radians per second, $\Omega = 7.2925 \times 10^{-5}$ radians/sec is the sidereal rate, A is the target's azimuth, ϕ is the latitude of the observatory, z is the target's zenith distance, f_{rot} is the minimum field rotation required for ADI in radians, $\frac{\lambda}{D}$ is the size of the PSF in arcseconds and r_{sep} is the radial distance from the axis of ro-

tation in arcsecond. It is important to note that for a 30–m class telescope the gain in cadence is proportional to the primary mirror's diameter (see Eq. A.6). This is because the diffraction-limited PSF is smaller, which in turns makes the necessary arc traced during the ADI rotation shorter. Space telescopes that allow the rotation of the entire spacecraft, such as the Hubble Space Telescope, may in theory allow for a better temporal sampling, but in practice such rotations are often time–consuming and may limit the cadence. The factor of 4 in the nominator of Equation A.6 comes from the requirement for non-overlapping PSFs. Throughout this paper we use a target with a declination of $\delta \sim +21^{\circ}$ (reminiscent of HR8799) observed from the latitude of the Paranal observatory ($\phi = -24^{\circ}$). Using Equation A.5 for these set of parameters we obtain a value for ω near meridian of $\sim 0.02^{\circ}/sec$

Due to the complexity of adaptive optics instruments and the sensitivity of the AO correction to the atmospheric conditions it can be challenging to reach absolute photometry with 1% accuracy. While extreme AO systems are expected to reach very high signal to noise ratios on bright giant planets, as discussed in Section A.3.3, here we also offer three further techniques that will help reaching high-precision photometry. First, we point out that rotational mapping does not necessarily require absolute photometry. In some cases the host star itself can be used as a photometric reference source. This is not always possible due to the high contrast but other planets in the system should provide ideal comparison points. A good example is the HR8799bcde system, where relative photometry between the three, similarly bright outer planets can provide accurate relative measurements (Apai et al., 2013). Second, most AO high-contrast imaging pipelines allow the injection of an

artificial star in the raw data, which can quantify flux losses during the data reduction. Such artficial star tests can be combined with the relative photometry to further quantify losses and uncertainties. Third, we point out that high-order deformable mirrors can be used to inject an artificial "speckle" into the optical system (Marois et al., 2006b). Such "speckles" are images of the star and thus can serve as ideal references for relative photometry, even if there are no suitable planets or if the star itself is too bright.Therefore, reaching even sub-percent accuracy in relative photometry with next-generation AO systems seems plausible.

We explore six distinct realizations of the different surface types present on the atmosphere of the giant planet, shown in Table A.3: a) cloudy spots on a clear surface, with the same (Model A1 hereafter) or with different temperatures (Model A2 hereafter), representing clouds on a cloud-free surface; b) clear spots on a cloudy surface, with the same (Model B1 hereafter) or with different temperatures (Model B2 hereafter), representing clear, deeper holes in an otherwise global cloud cover; c) clear surface with cold and hot clear spots (Model C hereafter); and d) cloudy surface with cold and hot cloudy spots (Model D hereafter). Using the B06 cloudy and clear models we simulate spectral modulations due to rotation for effective temperatures between 800K and 1200K and a wavelength range between 1 and 12 μm.

In the next section we present the results of our model using a spectral resolution of 100 and the simple spot distribution in Figure A.1.

A.3 Results

The model described in the previous section allows us to predict rotational variations in the photometry and spectroscopy of giant exoplanets and simulate their observations with existing and next–generation facilities. Here we will evaluate the capabilities of different telescope/instrument classes for characterizing giant exoplanets beyond one–dimensional measurements. We also identify the ideal instrument setup as a function of target temperatures and cloud properties.

A.3.1 Properties of the Simulated Variability

An example of normalized model lightcurves is shown in Figure A.4 where we plot the results for the J, H, Ks and L' filters for Model B2, as described in Section A.2.3.2. The maximum normalized amplitude in all three bands occurs when the giant, Clear hot spot (which is 200 K hotter than the 1,000 K effective temperature of the Cloudy surface) rotates into view. As expected from a closer inspection of the green and yellow lines in the top panel of Figure A.3, the largest photometric variations, up to 19% from the mean occur in the J-band. This behavior is consistent with results from Artigau et al. (2009) and Radigan et al. (2012) who also reported the largest photometric modulations in the J band for two early T–type brown dwarfs. The H and K-bands have similar behavior in Figure A.4 with 14% maximum photometric amplitude for the former and 15% for the latter while the amplitude of the modulation in L' is not more than 10%. The minimum in all bands is

caused by the two Clear (red spectrum, top panel of Figure A.3) cold (T=800 K) spots seen on the right panel of Figure A.1. This lightcurve minimum is prominent – up to 13% lower than the mean J band lightcurve – given that neither of the cold spots cover more than 4% of the visible hemisphere (see Section A.2.1 and Figure A.2). Note that the trough is not a symmetric feature because the giant spot rotates into view and dominates the lightcurve, decreasing the effect of the two cold spots. There are many small spots in the model (less than 1% of the visible hemisphere covered) that contribute small-level photometric variations, whose presence can be deduced from the lightcurve with sufficient sampling rate and accuracy.

Simulated normalized rotational spectral modulations for Model B2 are shown in Figure A.5 for the JWST/NIRSPEC and JWST/MIRI wavelength range with a spectral resolution of 100. The variations are very strong (up to 35% minimum to maximum) not only in the J, H and Ks–bands but also in the mid–infrared (MIR) where they can be as high as 20% at 6 μm. The rotation phases for the rise and fall of the amplitudes in the MIR show distinct variations, in particularly at 9.7 μm compared to 10.3 μm. The heterogeneous nature of the atmosphere is easily discernible as spots of different temperature and chemical composition rotate in and out of view. Such spectral maps will not only suggest variations in the abundance of gas–phase absorbers, in particular methane or water, but will also further constrain the covering fraction and longitudinal distribution of the spots.

To further explore the behavior of spectral maps and to study how they respond to changes in the input parameters (surface type, temperature, covering fraction), in Figure

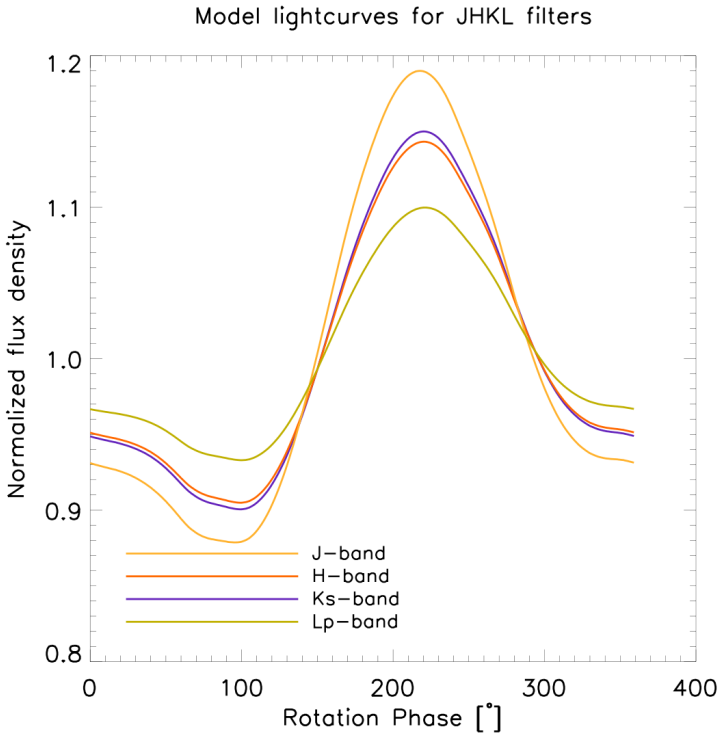

Figure A.4 Normalized model lightcurves as a function of rotation phase for the map in Figure A.1, using Model B2 (clear spots on a cloudy surface, with different temperatures) and assuming $T_{eff} = 1000K$ and the Giant Spot at 1200K. As discussed in the text, a suite of next–generation instruments, dedicated to direct imaging of giant exoplanets, can detect such modulations and measure the rotation periods and/or cloud–coverage of the planet.

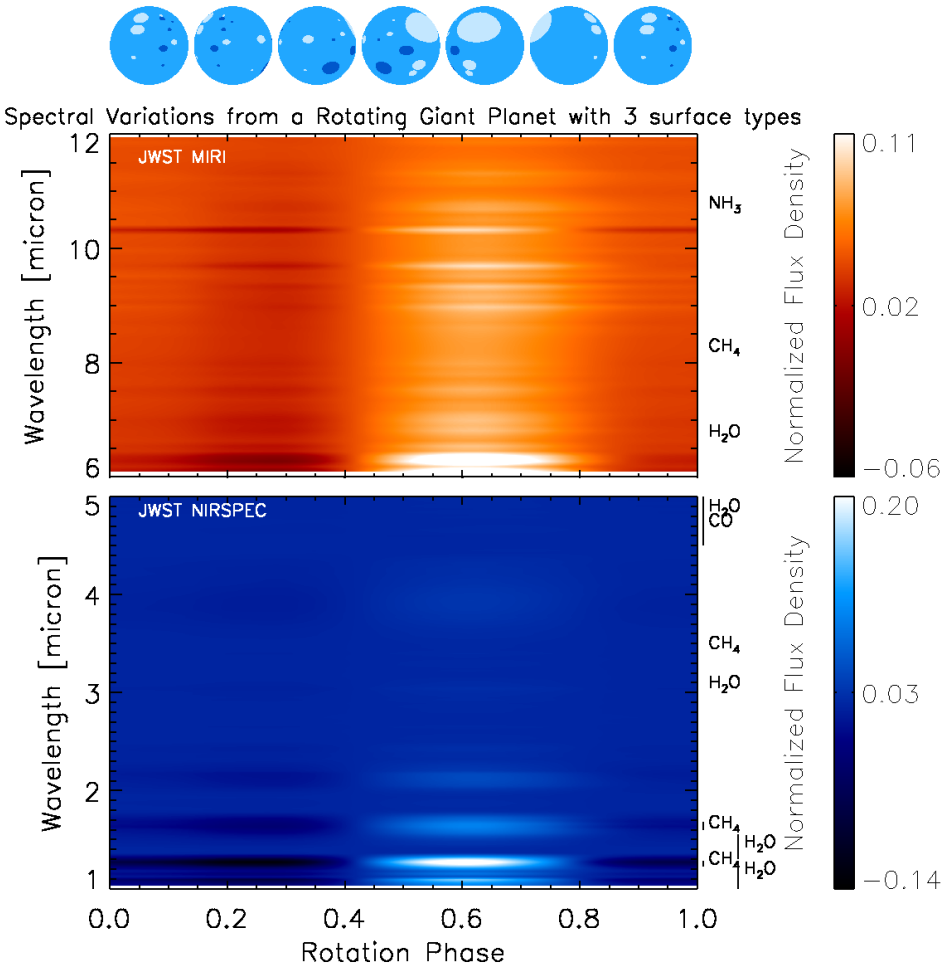

Figure A.5 Predicted spectral modulations (normalized) for JWST/NIRSPEC and JWST/MIRI (with a resolution of 100) as a function of the rotation phase for the map in Figure A.1, using a model with clear spots on a cloudy surface (B2 from Table A.3) for a planet with T_{eff} =1,000 K and a giant hot spot of 1,200 K. The top panel shows the visible hemisphere as a function of orbital phase (shown at the bottom). Absorption bands for the respective molecules are marked on the right.

A.6 we present three different realizations of the spectral map in Figure A.5 for wavelength range between 1 and 2.5 μm. Here we change only the temperature of the spots and their type (Cloudy or Clear) but keep the T_{eff} = 1,000K and total spot-covering fraction f_c constant at 10% and using the atmospheric map in Figure A.1 throughout. Changing the covering fraction will change the amplitude of the variations, but not the wavelengths/spectra or the periods. Using the nomenclature of Table A.3, we show Model A1, Model A2 and Model C on the top, middle and lower panels respectively. The relative variations in the J, H, and Ks-bands are different between the different scenarios. When the giant spot rotates into view, the J-band modulations for Model A1 are negative (as there is less of the brighter, Clear surface; green line in top panel of Figure A.3), while those in H- and Ks-bands are positive (as there is more of the brighter, Cloudy surface; yellow line, Figure A.3). On the contrary, the J-band variations are positive for both Model A2 (middle panel) and Model C (lower panel) when the giant spot faces the observer. The alternating darker and brighter stripes in the J band in the middle panel of Figure A.6 are a direct consequence of the differences between the 1,000 K Clear (top panel Figure A.3, green) effective surface and the 1,200 K Cloudy (top panel Figure A.3, light orange) model spectra – the former is higher but narrower compared to the latter in this waveband. When the Cloudy Spot rotates into view, it enhances the flux density (white, J-band in the middle panel of Figure A.6) in the sides and decreases it in the middle of the filter band, where the contribution of the brighter, Clear surface is lower. Therefore, while photometric variations like the ones in Figure A.4 can be interpreted as caused by either a hotter/colder region and/or different

chemical composition, *spectral* modulations, such as the ones seen in the J–band in middle panel of Figure A.6, can identify gas-phase compositional variations. The magnitudes of the variations are different between the three models: the variations are strongest in Model C (lower panel, minimum to maximum amplitude of 20%) and weakest in Model A1 (top panel, minimum to maximum amplitude of 10%). We note that the magnitudes of the variations for all three models in Figure A.6 are significantly smaller than those in Figure A.5 where the minimum to maximum amplitude is up to 35% (for model B2 from A.2.3.2). Additionally, detection of such spectral modulations can also further improve light curve inversion techniques such as the principal component analysis discussed in Section A.4.

Next we explore the optimal filter for detecting variations for Model B2 as a function of the temperature of the giant spot. In Figure A.7 we show the results for three different effective temperatures of the planet – 800 K, 1,000 K and 1,200 K (top, middle and lower panels, respectively) for the J, H and Ks filters. The temperature of the giant spot varies between -300K and $+300$K from the effective temperature with $\delta T = 100K$, while the temperatures of the rest of the spots (either cooler or hotter by 200 K compared to the effective temperature) stay the same throughout. Changing the temperature of the giant spot while keeping everything else constant will not only change the amplitude of the variations, but also the shape of the lightcurve with the result that different features will produce the largest amplitudes. The two cold spots in the right panel of Figure A.1 are very prominent in some cases where the giant spot plays only a secondary role (for example, $T_{eff} = 1200$K and $T_{spot} = 1000, 1100, 1300$K) and are in fact responsible for the

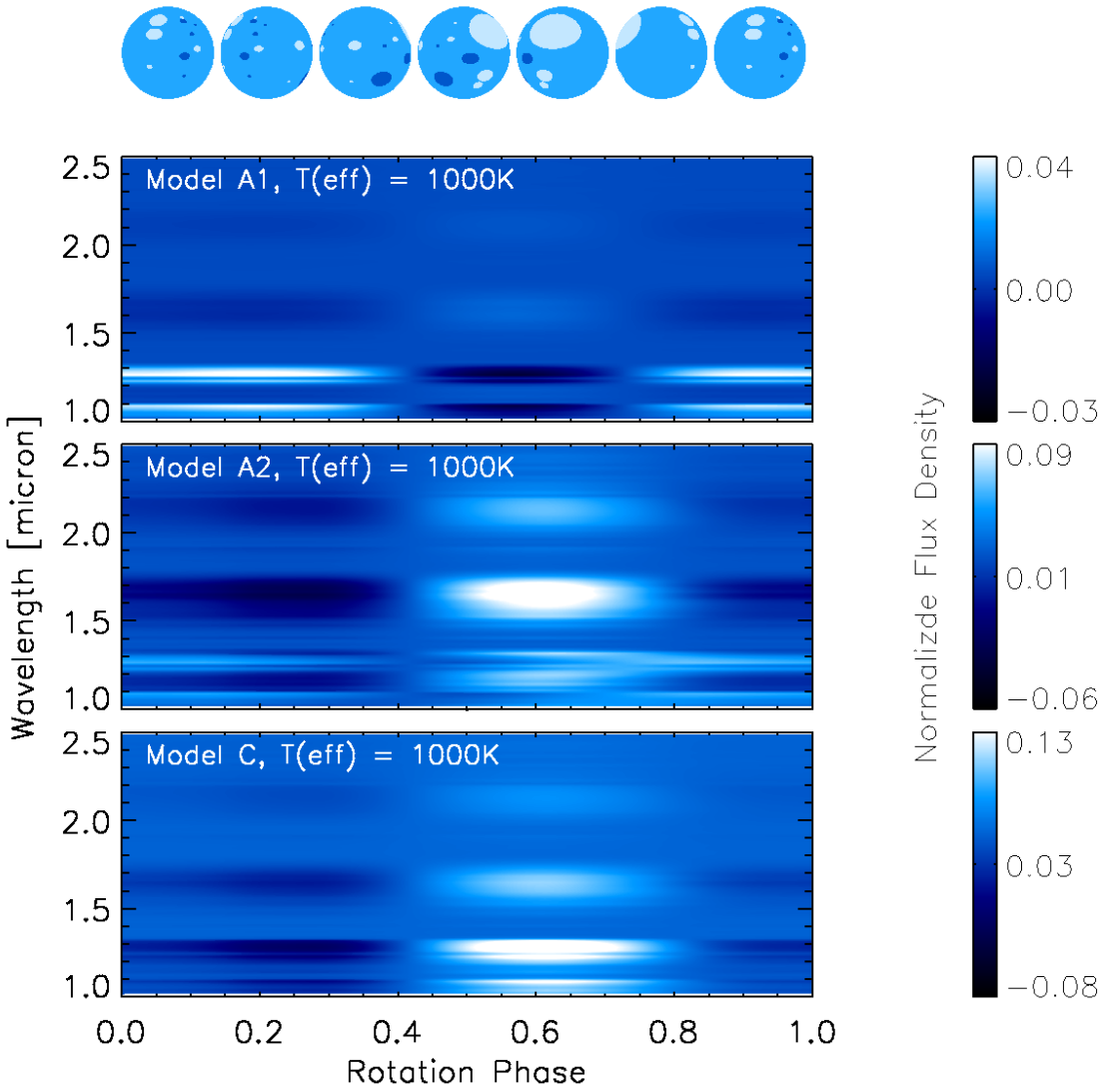

Figure A.6 Same as Figure A.5 but for different properties of the spots (temperature and surface type). Top panel is for Model A1, middle panel is for Model A2 and lower panel is for Model C. All models are for a $T_{eff} = 1000K$.

largest amplitudes. Regardless of the features responsible, the largest photometric modulations – the variations producing the strongest observable signal – occur in the Ks–band for $T_{eff} = 800K$ (up to 60% for the hottest spot, upper panel, Figure A.7) and in the J–band for $T_{eff} = 1000K$ and $1,200K$ (up to 30%, middle and lower panels, Figure A.7). This result suggests that for sources with physics/chemistry similar to those in Model B2, like SIMP0136 (Artigau et al., 2009) and 2M2139 (Radigan et al., 2012), the most appropriate filter where the photometric variations are largest and will be most easily detected is indeed J, as these authors noted. For colder sources or sources with a cold spot, however, Ks would be more appropriate. As expected, all three bands "brighten" as the temperature of the giant spot increases from $T_{eff} + 100K$ to $T_{eff} + 300K$, reminiscent of the well-known J–brightening effect (Burgasser et al., 2000, 2002; Leggett et al., 2000) probably caused by the appearance of cloud–free regions at the L/T transition. Here, the brightness increases not due to increase in the size of the clear regions, but due to the increase in their temperature. The three bands brighten at different rates, from the slowest increase in amplitude of 12% (Ks–band, lower panel) to the fastest of 40% (Ks–band, upper panel). The fastest brightening for all three filters consistently occurs for the model in the upper panel. We also note the continuous transition in the most appropriate choice of filter where the largest amplitudes occur. As the T_{eff} decreases from 1200K to 800K the best filter changes from J (lower panel) to Ks (upper panel) and as the temperature of the giant spot decreases from $T_{eff} + 300K$ to $T_{eff} - 300K$, the best filter changes from J to Ks (middle and lower panels). With even larger temperature differences, Ks–band amplitudes would eventually exceed

those seen in the J–band. Such large temperature differences between the different surface types are, however, not expected (although see Skemer et al. (2012)). All the results discussed above are the direct consequence of the interplay between the spectral differences between the Clear and Cloudy model for these temperatures (see Figure A.3) and the distribution and sizes of the different surface features. The largest photometric amplitudes occur in different filters for different models. For example, for Model A2 the largest modulation for the same calculation as done for Figure A.7 consistently occur in the Ks–band. A survey over targets with different T_{eff} can populate Figure A.7 with more points and in combination with the model presented here can provide information on this level of details.

The following four subsections describe the outcome of simulated photometry for different instruments classes using the theoretical lightcurves from Figure A.4 and outline the increasingly complex picture of the optical appearance of the giant exoplanet that can be learned.

A.3.2 8–m Class Telescopes with AO

The general prediction of our model is that the largest amplitude changes occur in J-band. However, J-band is not the optimal wavelength for current 8 m-class telescopes with state-of-the-art AO systems: the planet–to–star flux ratio is $\sim 1.2 \times 10^{-5}$ (see Section A.2.3.1). Instead, longer wavelengths provide a better AO correction and more favorable planet-to-star contrasts. We use here the example of VLT/NACO and assume residual stellar PSF in Ks similar to that in L' (Kasper et al., 2007, 2009; Lagrange et al. , 2010; Bonnefoy

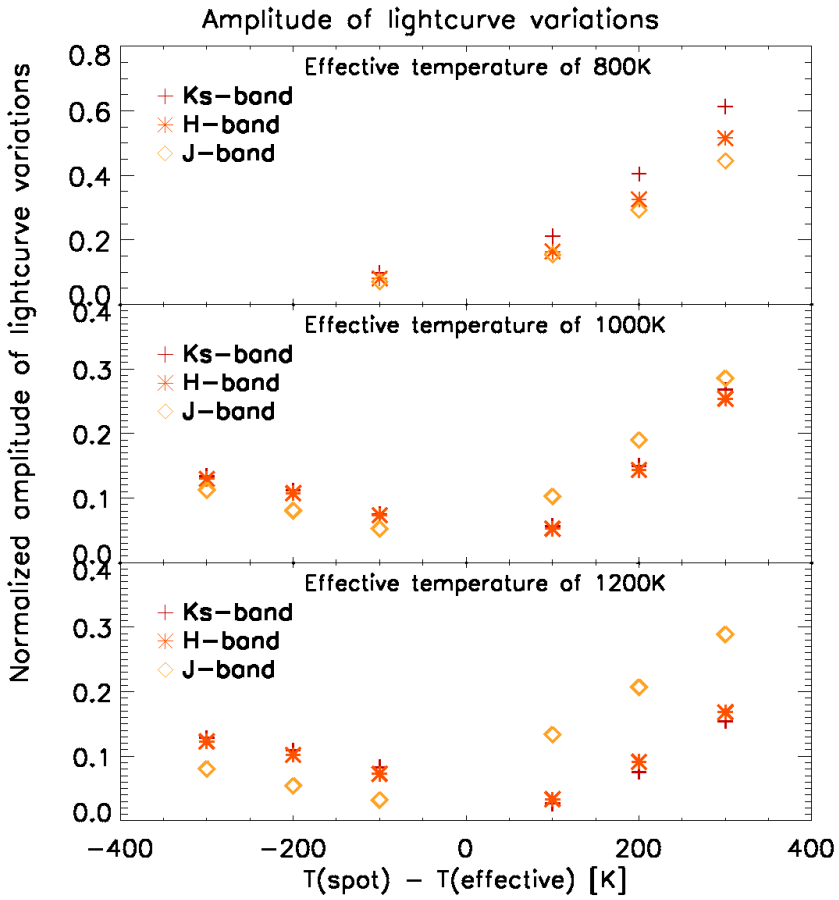

Figure A.7 Normalized amplitudes of lightcurve variations as a function of the temperature of the giant spot for the map in Figure A.1. The top panel is for $T_{eff} = 800K$, the middle panel is for $T_{eff} = 1000K$ and the lower panel – for $T_{eff} = 1200K$. All three panels are for Model B2 (Table A.3). The largest variations occur in different filters depending on the temperature of the giant spot, suggesting that the observations should be carefully tailored to the specific target.

et al., 2011) to simulate Ks–band photometry where the planet–to–star flux ratio is higher (the planet is brighter): $\sim 3.7 \times 10^{-5}$ (Section A.2.3.1). For the Ks–band VLT/NACO PSF FWHM of $\sim 0.069\ ''$ we calculate $f_{rot} \sim 16^{\circ}$ from Equation A.6. Using this value for f_{rot} and a field rotation rate near meridian $\omega \sim 0.02 \frac{^{\circ}}{sec}$ results in ∼14 minutes minimum required time for proper ADI reduction. The signal–to–noise ratio (SNR) for the planet is ∼ 15; here we adopted a read noise of 46.20 electrons as given by the VLT/NACO Exposure Time Calculator (ETC) and an observing mode similar to (Kasper et al., 2009) but modified for Ks, namely dithered individual 1 min exposures with detector integration time (DIT) of 0.3454 sec (given by the VLT/NACO manual) and 200 DIT per position. The simulated Ks–band lightcurve for model B2 with added normally distributed photometric uncertainty of 10% is shown in the top panel of Figure A.8.

Detection of the photometric modulation is not background–limited but is instead limited by the residual stellar point spread function. The smallest detectable Ks–band variability at 3σ level is $\sim$ 20%, on par with our simulated maximum amplitude (see Figure A.4). Therefore, this instrument configuration is capable of confidently detecting the Ks–band photometric variations produced by the giant spot in Figure A.1 and retrieving the rotation period of the planet. It is, however, inadequate to explore the smaller variations (at the ∼1% level) expected from the smaller clouds.

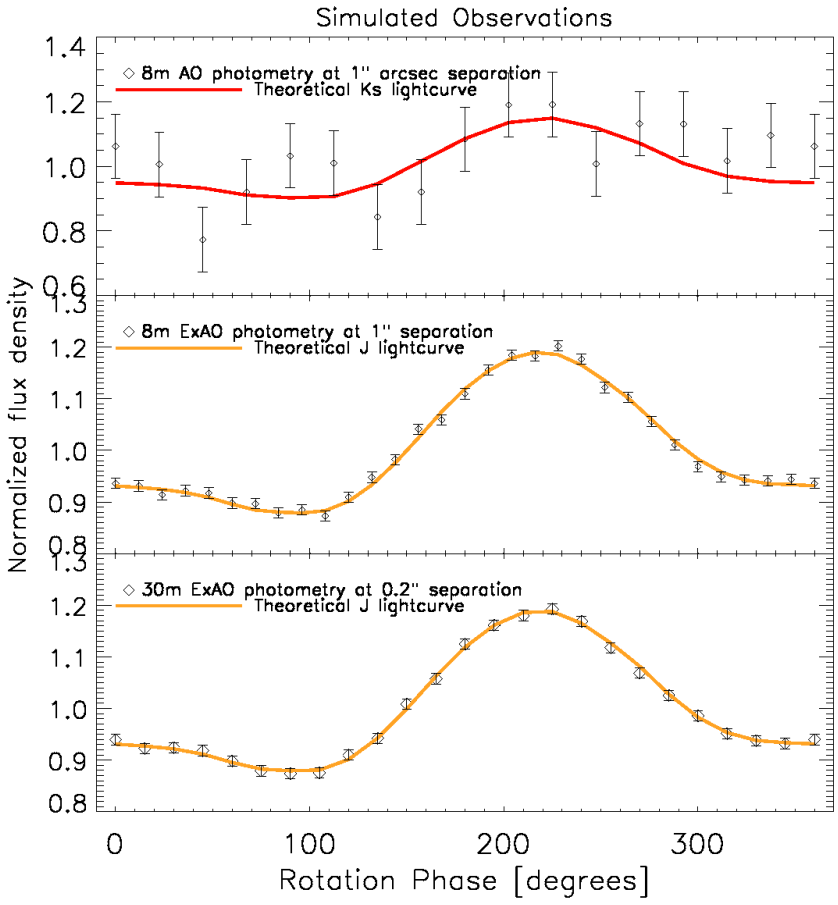

Figure A.8 Simulated observations of a $T_{eff} = 1000K$ planet with a giant hot spot of 1200K (Model B2) for an 8–m class telescope with AO (upper panel) and with Extreme AO (middle panel), and for a 30–m class telescope with Extreme AO (lower panel). The red and yellow line are the theoretical lightcurves from Figure A.4, the black diamonds are simulated photometry; the error bars represent a photometric precision of 10% in the upper panel and 1% in the middle and lower panels. We assume a rotation period of 4 hours. The temporal sampling is 15 min cadence for the 8-m AO, 8 min for the 8-m ExAO and 10 min cadence for the 30-m aperture.

A.3.3 8–m Class Telescopes with next-generation Extreme AO

The next-generation of high-order AO systems (extreme AO, or ExAO) will be capable of delivering very high quality correction also at shorter wavelengths, allowing variability searches to focus on the most favorable wavelengths. To evaluate this configuration we repeat our calculation for the minimum ADI cadence but for J–band PSF – in this case f_{rot} $\sim 9^{\circ}$ and the minimum required time for proper ADI reduction is $\sim$8 minutes.

Following the science requirements for VLT/SPHERE and Gemini/GPI (Mesa et al., 2011; Macintosh, et al., 2008) we use a residual stellar PSF of 10^{-7} at a separation of $1''$, and a read–noise of 10 electrons to simulate the $\sim$ 100 SNR J–band photometry (with added normally distributed noise of 1%, see below) for model B2 shown in the middle panel of Figure A.8. We note that the high Strehl ratio provided by the Extreme AO (up to 80%) reduces the speckle noise to such low levels that the limiting factors for the detection of photometric variability will be the photometric precision, read noise and instrument stability. Here we use a 1% J–band photometric precision following the prescription of Vigan et al. (2010) for VLT/SPHERE, thus setting the limits on the smallest detectable variability. This instrument configuration will be able to easily measure the rotational periods of planets, will allow preliminary exploration of cloud colors and can even detect the temporal evolution of the cloud cover. Evidence for such changes in cloud cover in brown dwarfs have been reported (Artigau et al., 2009; Radigan et al., 2012), but their detection requires

high signal–to–noise.

For example, the amplitude difference in the simulated (H−Ks) color for the giant spot in the right panel of Figure A.1 is on the order of 0.5% while the (J−Ks) amplitude color difference is up to 4%. Amplitude difference in the (J−Ks) color for the two cold spots in the right panel of Figure A.1 is ∼2% while that in (H−Ks) is ∼0.5%. Here we expect a few σ detection of (J−Ks) modulations caused by the rotation of the giant spot but in general the confidence with which such measurements could be obtained will be ultimately dependent on the photometric precision. A limitation on the capabilities of this class of instruments will be the achievable cadence due to the ADI requirements as discussed in Section A.2.3.2, an obstacle that will be overcome by the class of instruments presented in the next section.

A.3.4 30–m Class Telescopes with next-generation Extreme AO (30m+ ExAO)

This group of instruments represents the suite of planned extremely–large-aperture ground–based telescopes. Following the method described in the previous two sections, we calculate a J–band ADI rotation time requirement of $\sim$ 2 minutes and $\sim$ 10 minutes for a planet at a radial separation from the parent star of $1''$ and $0.2''$ respectively; here we present the results for the latter. Using the required characteristics of the GMT/TMT/ELT (GMT, 2006; Macintosh, et al., 2006; Kasper et al., 2010), we use a residual stellar PSF of 10^{-8} at

the radial separation of $0.2''$ to simulate the very high SNR (on the order of several thousands, using the ELT ETC provided by ESO) J–band lightcurve for model B2 in the lower panel of Figure A.8. As was the case for the 8m ExAO systems, the residual stellar PSF is no longer the main culprit for systematic errors. Here we adopt a photometric precision of 1% following the discussion in Dekany et al. (2004) and Liske et al. (2011).

The capabilities of these instruments represent a significant step forward from those of the current 8– and 10–m class telescopes. The high Strehl ratio combined with the improved cadence provided by the 30–m class ground-based telescopes will allow precise measurements of the basic characteristics of the planet's atmosphere like rotation rate or large–scale inhomogeneity. As for the 8–m class Extreme AO instruments, the 30–m class Extreme AO instruments will also be able to measure cloud colors only down to a level ultimately limited by systematic trends in the photometry, due to the instrumental changes, atmospheric variations, etc. The most significant improvement of the 30–m Extreme AO over the 8–m Extreme AO instruments will be in their ability to do moderate–resolution ($R \sim 100 - 1000$) spectroscopy both in the near IR with an Integral Field Spectrograph (IFS) on ELT/EPICS, TMT/NFIRAOS and GMT/NIRExAO Imager (Vérinaud et al., 2010; Herriot et al., 2006; Johns, 2008) and in the mid–IR using, for example, instruments like GMT/TIGER in the 8 to 20 μm wavelength coverage (Jaffe et al., 2010). Further improvements will come in the form of polarimetric measurements and the extended time–domain probed with the faster cadence, allowing detection of smaller-scale variations. Also, the radial separations at which giant exoplanets will be observed with a contrast of up to 10^{-9}

will be as small as $0.1''$, allowing the observations of colder and/or older giant planets in reflected light at orbital distances comparable to that of Jupiter (Kasper et al., 2010) and of very young planets close to the snow line. Access to such small angular separations will also significantly expand the available distance over which systems containing self-luminous Jovian planets can be directly imaged. This illustrates the unique capabilities of the next–generation extremely–large telescopes as even the future space-based telescopes like the JWST (discussed in the next section) will not have such small angular resolution. Direct imaging of Neptune–size or even Super Earths around the closest stars should be also achievable (Kasper et al., 2010). The favorable contrast between such planets and their host star at the mid–IR wavelengths will, albeit through challenging observations, allow low–resolution spectral characterization of their atmospheres by detecting H_2O, CH_4, CO, CO_2 and NH_3 features. Such measurements could also discern between a hydrogen–rich and a water–rich atmosphere and test for presence of hazes and non–equilibrium chemistry in the atmospheres of directly–imaged planets (e.g. Miller-Ricci Kempton et al. (2012); Rogers & Seager (2010); Désert et al. (2011)). Finding such planets in the habitable zone and studying their spectra for biosignatures will also significantly advance the field of astrobiology.

A.3.5 JWST

The James Webb Space Telescope will open a new chapter in the studies of directly-imaged giant exoplanets. With an aperture and Strehl ratio on par with the VLT/SPHERE but

free of the atmospheric aberrations, and combined with a dramatically low thermal background, JWST will have a greatly increased sensitivity and cadence. To simulate J–band photometry from NIRCAM we use a residual stellar PSF of 10^{-7} at a separation of $1''$ using the results of Green et al. (2005). To reduce the effect of aberrations, we assume a roll–deconvolution (Gardner et al., 2006) mode to be employed by the JWST using a conservative cadence of 15 minutes. Also, following the discussion in Lagage et al. (2010), we assume a photometric precision of $\sim 10^{-4}$. This is already at least an order of magnitude higher than the one for the ground-based facilities discusses in Sections A.3.3 and A.3.4 but is still significantly higher than the achievable contrast, and is again what ultimately limits the level of detectable variations.

The simulated observation is shown in Figure A.9. The significant decrease in the speckle pattern, combined with the very low background noise, the stability of the instrument and the short cadence will allow detailed studies of the rotation periods, cloud distribution, cloud colors and spectra, atmospheric maps and possibly weather patterns of directly imaged giant planets. The unique strength of JWST will be in the complementary observations in the near- and mid-infrared, studying wavelengths that are difficult to explore from the ground, such as the peak in thermal emission of young Jovian planets at 4.5 μm. As discussed by Clampin (2008), both the capabilities of NIRCAM in the F460M filter at separations larger than $0.6''$ and the sensitivity of MIRI will exceed that of even the planned 30-m class ground-based instruments. MIRI will also provide a platform uniquely suitable for observing planets at wavelengths longer than 5 μm.

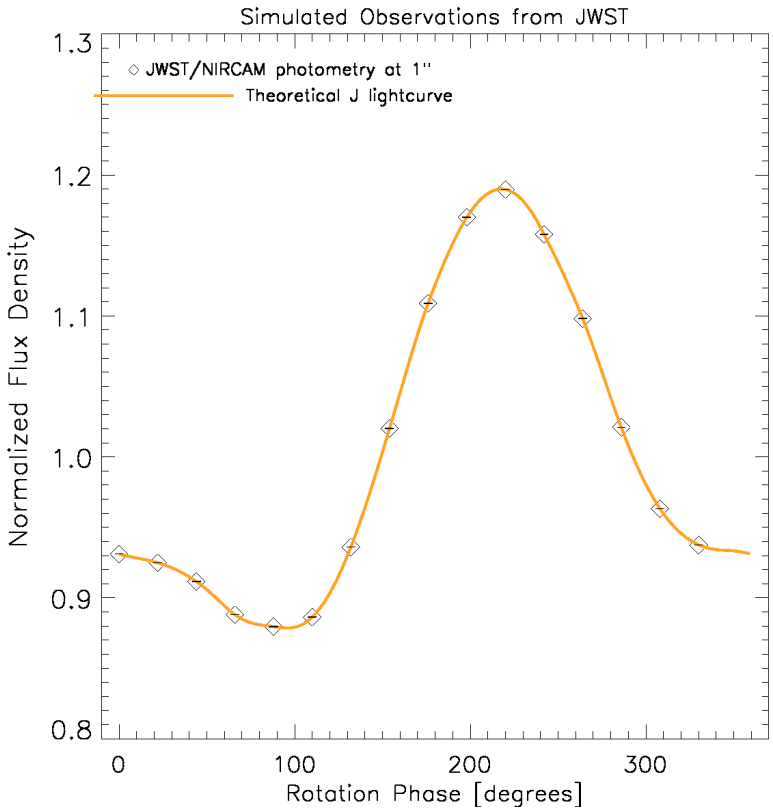

Figure A.9 Same as the previous figure, but for simulated observations from JWST/NIRCAM F115W with a cadence of 15 min and photometric precision of $\sim 10^{-4}$.

The fact that JWST will not suffer from telluric absorption will also allow more accurate observations of several key gas-phase molecular absorbers. As seen in Figures A.5 and A.6 prominent absorbers such as H_2O, CH_4, CO and NH_3 with very strong spectral features can be studied by NIRSPEC and MIRI in detail, allowing their spatial and temporal distribution among other things to be deduced. As discussed by Marley et al. (2010) and Bailer-Jones (2008) detection of variability in very temperature–dependent spectral features such as FeH, NaI and KI and/or correlated modulations between these features will further support the assumption of a patchy atmosphere. Detection of strong water absorption, for example, will indicate a hydrogen–rich envelope. The JWST will also be uniquely suited to study the mid–infrared regime, where the spectroscopic variations can be as high as 20% for the model seen in Figure A.5.

A.4 Lightcurve Inversion

To explore the feasibility of recovering the map from Figure A.1, we use a principal component analysis (PCA) and sinusoidal variations in surface brightness as a function of only the longitude as studied by Cowan et al. (2009) in combination with the formalism for light curve inversion (LCI) developed in Russell (1906). The purpose of this section is to illustrate the potential of LCI.

As an example we utilize a covariance-matrix PCA, using the five J, H, Ks, L' and M' filters as the input vectors defining a 5–dimensional parameter space to be converted to

a minimum set of eigenvectors sufficient to produce the simulated variations. The resulting normalized eigenvalues are shown in Figure A.10. Following the prescription for the method, we notice that the largest gap occurs between the second and the third eigenvalues, suggesting that only two principal colors above the mean background color are required to reproduce the observed variations, consistent with the three colors we used for our map in Figure A.1. The contribution from the two primary colors as a function of the rotation phase is shown in Figure A.11 where we use two panels to show the actual magnitude of the variations (rotation phase of zero is defined as the left panel on A.1). A maximum value corresponds to a rotation phase at which the largest area covered of that respective eigencolor is present on the side facing us and a minimum – the least. The primary eigencolor basically traces the input (orange) J–band lightcurve from Figure A.4. On the contrary, the behavior of the secondary is not immediately obvious from the input lightcurve. As pointed out in Cowan et al. (2009), the eigencolors do not represent an actual color but a deviation from the mean "color", which for our map in Figure A.1 is the 1,000 K (orange) background temperature.

To recover the surface map from Figure A.1, we follow the prescription of Russell (1906). We use the two different eigencolors as separate light curves and expand them in spherical harmonics. We then invert them for a longitudinal, sinusoidal brightness distribution. The inversion is done in one dimension only – there is no latitudinal resolution. For simplicity, we assume that the planet's rotation axis is perpendicular to the line of sight. The resulting longitudinal maps in Mollweide projection for the primary and sec-

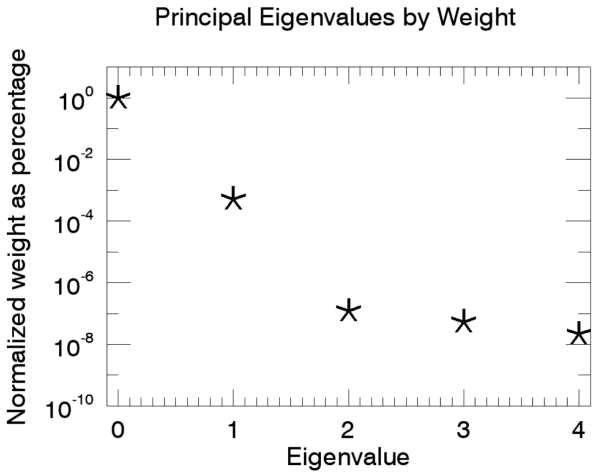

Figure A.10 Principal eigenvalues by weight: 0.998, 2.2×10^{-3}, 2.2×10^{-7}, 6.3×10^{-8} and 3.1×10^{-8}. The two largest values correspond to the two eigencolors representing the two different spot temperatures we assumed in our model. The results shows that the simulated photometric variations are indeed caused by only two colors (different from the mean color, which is a manifest of the effective temperature of the planet), or precisely the number of "extra colors" in our input map. The other three eigenvalues are zero to the precision we used. We used our own PCA routine, but the built–in IDL PCA routine also gives zeros for these three.

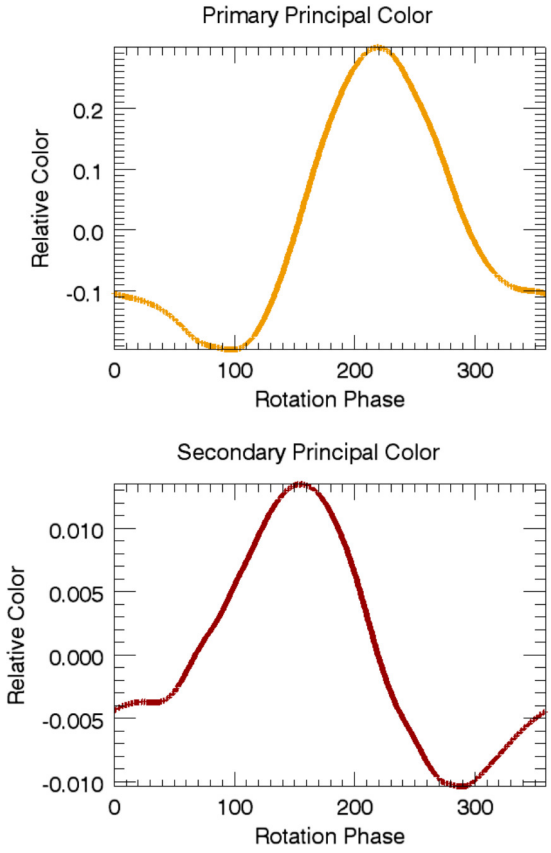

Figure A.11 Phase variations of the primary (top panel) and secondary (lower panel) eigencolors as inverted by PCA from the simulated photometry from Figure A.4. Rotation phase of zero is defined as the left panel on A.1. A maximum in the relative color outlines a rotation phase at which the most amount (largest area covered) of that respective eigencolor is present on the side of the planet facing the observer and a minimum – the least. The primary eigencolor practically mimics the input (orange) J–band lightcurve from Figure A.4, while the secondary has a completely different behavior, hard to notice by eye from the lightcurve.

ondary eigencolors are shown in the lower panels Figures A.12 and A.13, respectively. The "other" eigencolor on each map has been "masked out" because the two eigencolors are orthogonal. In the upper panels of Figures A.12 and A.13 we compare the PCA–inverted longitudinal maps to the input map (in the same projection) from Figure A.1. The two figures show that this simple method successfully recovers the longitudinal position of the major features, namely the giant hot spot at a longitude of $+135^\circ$ (Figure A.12) and the two groups of smaller, cooler spots at longitudes of -60° and $+60^\circ$ respectively (Figure A.13).

As Russell (1906) pointed out expanding the lightcurve in spherical harmonics does not completely determine the harmonics expansion of the surface brightness, as all but the first odd harmonics are absent in the lightcurve. Nevertheless, this simple model not only recovers the contribution to the lightcurve from the primary, dominant eigencolor (maximum variation of up to 0.3, upper panel, Figure A.11) but also identifies the effect of the much weaker components (maximum variation of 0.013, lower panel, Figure A.11) from the secondary eigencolor, allowing us to infer the presence of distinct surface features on the planet.

A more comprehensive way to obtain the surface map of the plane would be to use the PCA on the spectroscopic instead of the photometric variations, using the resolution of the instrument to increase the dimensionality of the data – a single, low-resolution spectrum of R$\sim$ 50 will increase the number of orthogonal data sets by an order of magnitude over the five filters discussed above.

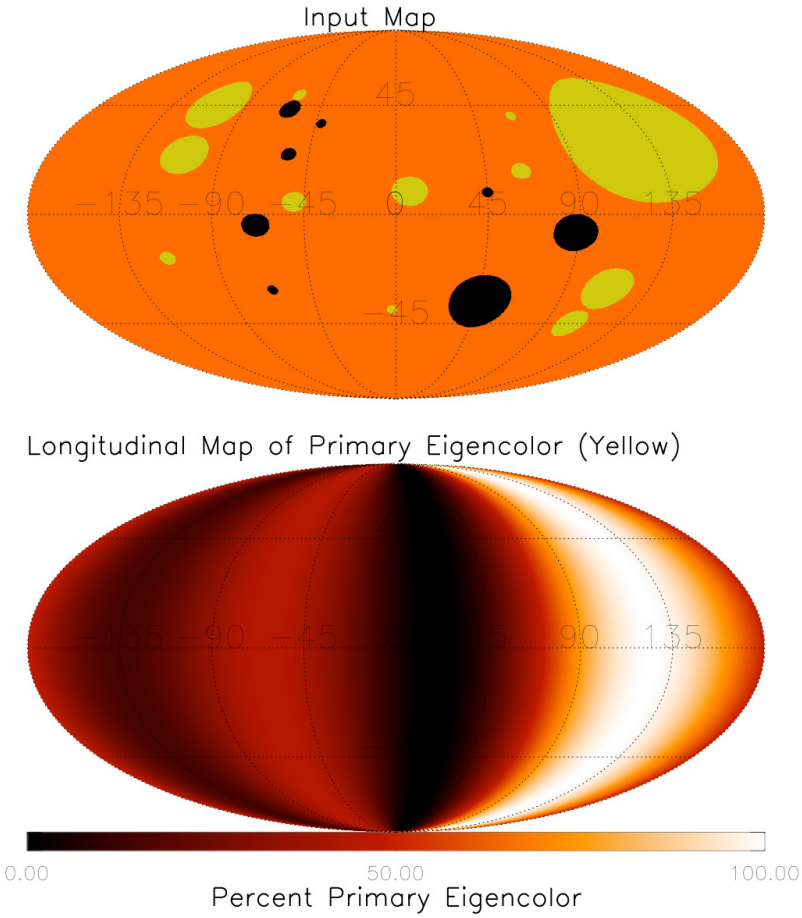

Figure A.12 Mollweide projection of the input map (upper panel: $orange = 1000K$, $yellow = 1200K$, $black = 800K$) and of the PCA–inverted, longitudinal distribution of the primary eigencolor (lower panel: normalized percentage contribution). The inversion method used successfully recovers the longitudinal position (there is no latitudinal resolution) of the giant hot spot at $+135°$ and, to a somewhat lesser degree, that of the two smaller spots at $\sim -110°$. The secondary eigencolor is masked out (as black) in the upper panel as it is orthogonal to the primary and does not contribute to the variations of the primary.

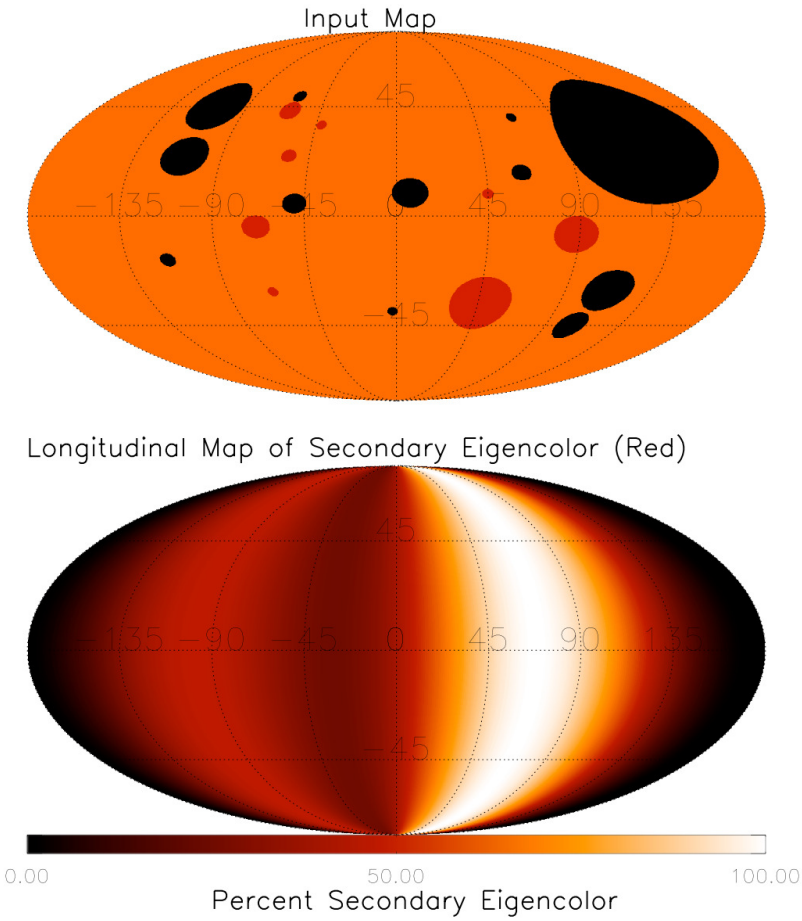

Figure A.13 The same as the previous figure, but for the secondary eigencolor (upper panel: *orange* $= 1000K$, *black* $= 1200K$, *red* $= 800K$). As in the case for the primary color, the inversion successfully recovers the longitudinal position of the two groups of cold spots, at $\sim -60^{\circ}$ and $\sim +60^{\circ}$ respectively. The primary eigencolor is masked out (as black) in the upper panel.

The method described thus far is well suited to study the color asymmetry caused by the spots in the form of spatial distribution over the surface of the planet, after simplifying assumptions like the longitudinal sinusoidal intensity map or an N-slice map (see Cowan et al. 2009).

A.5 Discussion

A.5.1 Patchy Dusty Atmospheres in Brown Dwarfs and Exoplanets

Early attempts to understand the nature of giant planets were based on the use of atmospheric models of L and T brown dwarfs as templates to assess the detection sensitivity for direct imaging surveys. While at similar temperatures to the regime of the L/T transition objects (between $\sim$ 900K and 1200K where dust clouds settle below the photosphere), it has been suggested that giant planets may, in fact, remain cloudy where the T dwarfs become cloud-free (Saumon & Marley, 2008; Currie et al., 2011; Barman et al., 2011a; Madhusudhan et al., 2011; Skemer et al., 2012), reminiscent of the results of Stephens et al. (2009) on low-gravity BDs. This does not necessary invoke a new kind of atmospheres for the directly–imaged giant planets. Most likely it is an age effect of atmospheres rather more dusty for their spectral type.

The observed abundance of methane compared to CO in the four planets of the HR8799

system has been reported to be lower compared to chemical equilibrium models predictions, suggesting efficient convective mixing on time-scales shorter than the CO to CH_4 equilibrium rate (Hinz et al., 2010; Barman et al., 2011a; Skemer et al., 2012). This assumption is further supported by the 3.88 to 4.10 μm spectroscopy of HR8799c being inconsistent with both the DUSTY (Chabrier et al., 2000) and the COND (Baraffe et al., 2003) models, indicating non-equilibrium chemistry at work. It appears that giant planets such as HR8799bcde and 2M1207b (a rather more pronounced case) may indeed have the temperature of T–dwarfs but the dusty appearance of L-dwarfs (Chauvin et al., 2004; Skemer et al., 2011; Barman et al., 2011b). In particular, the luminosity of HR8799b, for example, implies an effective temperature of 850K while its colors suggest a much hotter atmosphere of 1300K (Skemer et al., 2012). Models with thick clouds (with the cloud base significantly deeper compared to that of L/T dwarfs) and low surface gravity are invoked by Currie et al. (2011) to match the planets in the HR8799 system. Their best-fit model for HR8799b yields T_{eff} = 800–1000K and log(g) = 4.5 and T_{eff} = 1000–1200K and log(g) = 4–4.5 for HR8799cd. The authors put less importance on the effects of non-equilibrium chemistry in reproducing the 1 to 5 μm SEDs but suggest that the planet atmospheres may indeed be out of equilibrium. Interestingly, they also argue that "patchy" cloudy models may provide an even better fit to the data. On the contrary, to explain the observed low effective temperature (less than 1000K, typical of cloud-free T-dwarfs), red colors and smooth spectrum of HR8799b, the results of Barman et al. (2011a) support the presence of thick photospheric clouds and enhanced metallicity in the presence of non-equilibrium

chemistry. The authors note that the spectrum of the planet is markedly different from that of typical field brown dwarfs, namely in the weaker methane and CO and stronger water absorption (suggesting a hydrogen-rich atmosphere). In contrast to the results of Currie et al. (2011) who stress the importance of cloud thickness over non-equilibrium chemistry, Barman et al. (2011a) assign equal importance to both. However, their best-fit model for solar abundance, with T_{eff} = 1100K and log(g) = 3.5, indicates a radius that is smaller than theoretically expected, suggesting that the metallicity of the planet must be higher. A chemical enrichment by a factor of ten produces a significantly better fit for their data to a model with T_{eff} = 869K and log(g) = 4.3, consistent with the planet's mass and age. Similar scenario can be drawn for the case of 2M1207b, where the apparent low luminosity and red colors are in stark contrast with the spectrum-derived $T_{eff}\sim$1600K. Using an atmospheric model with thick clouds, non-equilibrium chemistry, a mixture of grains and low surface gravity, Barman et al. (2011b) propose a best-fit solution with T_{eff} = 1000K and log(g) = 4., consistent with cooling track predictions and disfavoring exotic scenarios such as edge-on disks or planetary collisions. For both HR8799b and 2M1207, Barman et al. (2011a,b) point out that the thick clouds (reminiscent of L–dwarfs) extending across the photosphere, effectively accounting for the observed red colors, and the non-equilibrium chemistry consistent with the observed CO/CH_4 ratio are equally important but only in the presence of low surface gravity.

Further observations of the HR8799 planets (Skemer et al., 2012) also indicate that all four planets are brighter than expected at 3.3 μm compared to equilibrium models that

postulate significant methane absorption and dimming at this wavelength. The authors report that the observations are inconsistent with models with decreased CH_4, thick clouds and non-equilibrium chemistry. Their 3.3 μm photometry of HR8799b is not consistent with the best-fit model of Barman et al. (2011a) and is twice the value obtained by Currie et al. (2011). Using the models of Madhusudhan et al. (2011) and adopting a "patchy" cloud cover, Skemer et al. (2012) find a best-fit model (to all their photometry data except M–band) with a two-component atmosphere of 93% T_{eff} = 700 K (Madhusudhan et al., 2011)('A'–type clouds) and 7% T_{eff} = 1400 K ('AE'–type clouds) for HR8799b. Similar hybrid model atmospheres provide better fit to HR8799 c, d, and e compared to thick clouds/non-equilibrium chemistry models that again fail to reproduce the 3.3 μm colors. The four HR8799 planets have different effective temperatures but, intriguingly, similar colors which led Skemer et al. (2012) to suggest that their atmospheres should have similar properties and may indeed be an evidence for their patchy appearance.

Low-level photometric variability due to rotation of L and T dwarfs have been reported by multiple groups in the IRAC 4.5 μm and 8 μm bands (Morales-Calderón et al., 2006), and at shorter near-infrared wavelengths (Clarke et al., 2008; Artigau et al., 2009; Radigan et al., 2012). Ongoing large Spitzer and Hubble Space Telescope programs are identifying a larger number of previously unknown varying brown dwarfs.

A.5.2 Photometric and Spectroscopic Variability of Directly-Imaged Giant Planets

We showed that rotation periods can be measured with existing adaptive optics systems (Section A.3.2) if the modulation is as prominent as our models predict ($\sim$ 20%). The detection of variability with lower amplitudes will be possible with next-generation adaptive optics systems. One such system (LBT/AO), for example, already provides such a capability (Skemer et al., 2012). Rotational variability can provide three different types of information for directly imaged exoplanets: 1) single-band photometry can determine the rotational period without the ambiguity of inclination; 2) multi-band photometry can constrain the heterogeneity of the surface and the relative colors of the features, and 3) spectral mapping can provide spectrally and spatially resolved maps of the ultra cool atmospheres, offering detailed insights into the atmospheric structures of giant exoplanets. In the following we will briefly discuss these different measurements and their observational requirements as predicted by our simple model.

We showed that rotation periods can already be measured with existing adaptive optics systems (Section A.3.2). We find that for planets broadly similar to those in the HR 8799 system the amplitude of predicted variations peaks in the J-band, yet the optimal wavelength for observations is the Ks-band, where AO performance is superior.

Next-generation AO systems on large telescopes will provide greatly improved AO performance at shorter wavelengths. Our models predict that these systems will be able

to detect rotational variations at multiple wavelengths, determining cloud covering fraction and providing color information on the surface features (see Section A.3.3).

We also briefly explored spectral mapping of exoplanets on the example of JWST. These observations will provide spatially and spectrally resolved maps over a broad wavelength range and unaffected by telluric absorption. Our models predict that such observations both with JWST and with instruments on 30m telescopes will be limited by instrumental stability and not by contrast. This fact highlights the importance for sub-percent-level flux calibration techniques.

We also use our models to evaluate the factors that determine the detectability of rotational variations. We find that temperature, spatial and size distributions of the spots and the effective temperature of the planet play the most important roles. For the spot distributions we modeled (Fig. A.1), changing the inclination to $+30^{\circ}$ does not affect the amplitude of the lightcurves compared to 0° inclination but slightly changes their shape. On the contrary, an inclination of -50° emphasizes the contribution from the two cold spots in the right panel of Figure A.1 and changes not only the shape of the lightcurves but also the maximum amplitudes (see Figure A.14) – they decrease by 12%, 9.5% and 10% in the J–, H– and Ks–bands respectively compared to the maximum amplitudes for the 0° inclination scenario seen in Figure A.4. The importance of the inclination of the planet also depends on the spatial distribution of the spots – if they are distributed mostly around the equatorial region, highly-inclined planets will show lower level variability than planets seen from their equatorial plane.

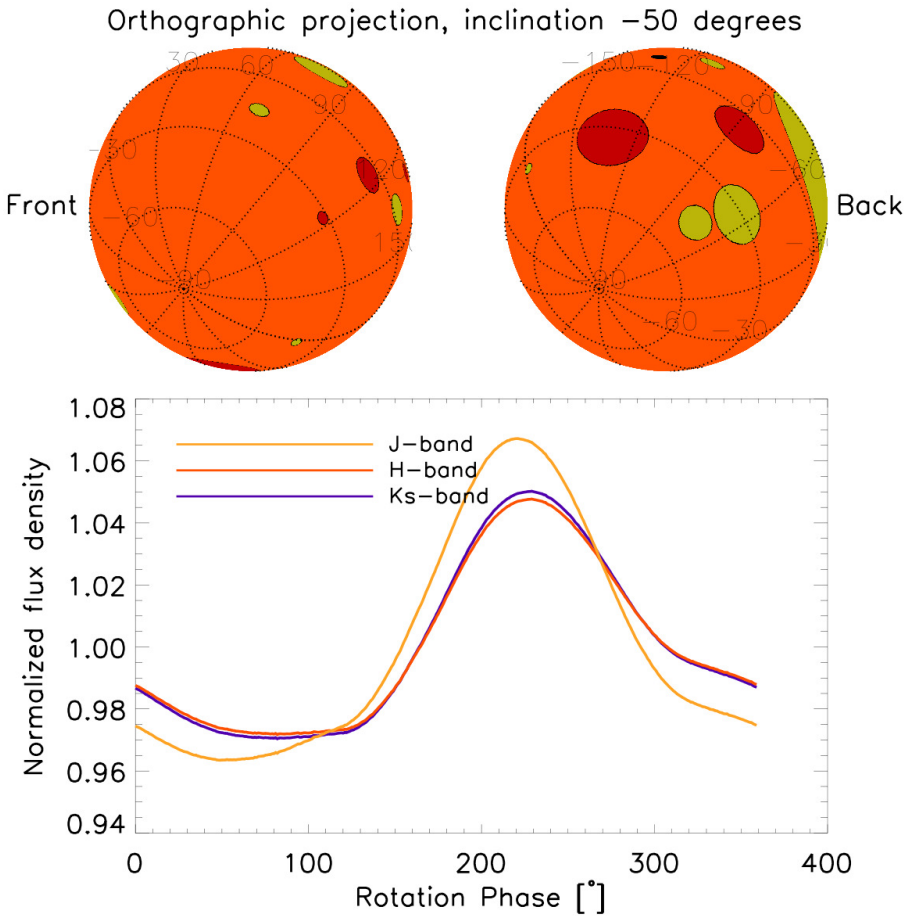

Figure A.14 Top panel: the same as Figure A.1 but for an inclination of $-50°$. Lower panel: the same as Figure A.4 but again for an inclination of $-50°$. The maximum amplitudes in all filters are significantly smaller (by as much as 12% in J–band) compared to an inclination of $0°$. The shapes of the lightcurves change as well (compared to A.4), emphasizing the lessened contribution from the giant hot spots.

We note the following major difference between the Clear and Cloudy B06 models we use that have major effects on the results presented in this paper: a) The flux densities of the Cloudy (yellow, Figure A.3) and Clear (green, Figure A.3) B06 models of 1,000 K are similar in both H and K-bands but differ significantly in the J–band, where the Clear model spectrum is notably higher. This is the well-known J-brightening effect (Burgasser et al., 2000, 2002; Leggett et al., 2000) caused by the appearance of cloud-free regions at the L/T transition; b) The J–band is stronger than the H–band for the 1,000 K Cloudy (yellow, Figure A.3) but the two bands have similar strength for the 1,200 K Cloudy (light orange, Figure A.3) models. The Ks-band is significantly weaker for both temperatures; and c) the 1,400 K Cloudy (dark orange, Figure A.3) model spectrum peaks in the H-band and the flux densities in the J and Ks-bands are somewhat similar. Therefore, we can expect that a heterogenous surface consisting of multiple patches (spots, holes and/or clouds) described by different spectra will have significantly different observational signatures compared to a homogeneous, one-surface-type atmosphere.

The distribution and sizes of cloud structures on directly imaged giant exoplanets will not be known a priori but constraints can be obtained by the model presented here. In Section 3 we showed that even a moderate spot total covering factor of 10% and spot distribution similar to that of Jupiter with a dominant giant spot can produce up to 20% photometric variability in J, H and Ks bands for a Cloudy surface with T_{eff} of 800 K, 1,000 K and 1,200 K, as seen from Figure A.7. Also, a giant spot with a temperature difference as small as $\delta T = 100$ K compared to the effective temperature can cause photometric

modulations of up to 20% in Ks–band for an effective temperature of $T_{eff} = 800$ K. We also argued that the most appropriate filter, where the largest simulated photometric variability consistently occurs depends on the different surface types present on the planet. As discussed in Section A.3.1, for our Model B2 and for the map in Figure A.1 the filter with the largest variations is Ks for T_{eff} lower than 1,000 K and J for T_{eff} ranging from 1,000 K to 1,400 K. However, for Model A2 the largest photometric variations occur in Ks for all T_{eff} from 700K to 1,400 K. This suggests that simply detecting the wavelength at which the largest photometric variations occur will already be a strong indicator of the relative contributions of cloudy and cloud–free regions to the planet's atmosphere and also of the temperatures of these regions.

Barman et al. (2011a) report a weak CH_4 absorption in both H– and K–bands and a triangular shape in the H–band spectrum for the case of HR8799b, indicating low surface gravity which may promote more efficient vertical mixing, deviation from chemical equilibrium and indicate a young age. As noted by the authors, such low surface gravity would also imply that the condensation curve crosses the T-P curve near the photosphere and clouds can form in the deeper, photospheric depths, suggesting that the giant young planets can be cloudy and cool. For the same effective temperature and surface gravity, the thickness of the cloud layer is significantly smaller compared to the case of chemical equilibrium but still sufficient enough to produce the observed colors, much redder than those of a cloud-free brown dwarf. Cloudy, cool, low-gravity brown dwarfs have indeed been reported (Stephens et al., 2009) at the L/T transition, pushing the transition temperature from

1,300 K (at log(g) of 5) down to 1,100 K (at log(g) of 4.5), supporting earlier evidence for such gravity–transition regime connection (Metchev & Hillenbrand, 2006; Saumon & Marley, 2008). The rotational phase mapping proposed here can provide critical insights into the structure and distribution of cloud layers and can test cloud scale height and compositional variations in directly imaged giant planets (Section A.3).

Our model predicts that the detection of photometric and spectroscopic variations with current instrumentation are limited by a combination of contrast and stability (section A.3), but next-generation extreme AO systems will provide superior contrasts that will no longer be the limiting factor. The sensitivity limits of the current state–of–the–art instruments like VLT/NACO limit the capabilities of these instruments to measuring rotation periods. With next–generation instruments like GPI, SPHERE, or extreme AO systems on GMT, TMT or E-ELT will be able to explore the details of the cloud asymmetry through the lower–amplitude (down to an assumed photometric precision of 1%) rotational modulations and study the J−Ks and H−Ks colors of spots covering the same fraction ($\sim 1\%$) of the surface area while JWST may push this limit down to the level of $\sim 10^{-4}$. The real power of the future very large–aperture telescopes, both ground– and space–based like GMT, TMT, E-ELT, JWST and possibly ATLAST, will be in the spectral modulation domain, where they will open up the possibility to study in detail the cloud colors, composition and/or spectra, weather patterns and even rings and satellites.

The Great Red Spot on Jupiter has already been shown to be a very dynamic feature – Asay-Davis et al. (2009) showed that the spot has shrunk by 15% over a period of 10

years. Such behavior needs to be taken into account when studying the atmospheres of directly–imaged giant exoplanets – variations on timescales different than the rotation period can indicate evolving atmospheric patterns or even storms. If the atmospheric patterns of these planets do indeed change on timescales shorter than the rotation period, the periodic photometric and/or spectroscopic modulations will be significantly modified or even completely erased (Goldman, 2005). Detections of photometric and/or spectroscopic evolution on timescales different from the rotation period will be a further step toward understanding the atmosphere of giant exoplanets. Such measurements, possibly achievable by JWST as discussed in Section A.3.5, will require very high-cadence observations and could be an indication of differential rotation (Artigau et al., 2009; Marley et al., 2010). We have not commented on the possible presence of symmetric belts or bands in the atmosphere of these planets as they will not cause photometric or spectroscopic variability and cannot be constrained by the model presented here.

A.6 Conclusions

We used simple models to explore light curve inversion as a tool to probe the surface brightness distribution and cloud properties of directly imaged exoplanets. We constructed models using state-of-the-art spectral libraries and simulated observations with current and future instruments. The key results of this study are as follows:

i) Current AO systems on large telescopes are capable of detecting large photometric

variations and thus measure rotation periods. Cadence is limited by the slowly varying PSF systematics.

ii) Next-generation extreme AO systems will be capable of detecting even low-level ($\sim$1%) variations, enabling the study of cloud heterogeneity and its wavelength dependence. These systems will also enable the study of the cloud cover evolution.

iii) Extremely large telescopes and JWST will provide spectral mapping data for clouds, allowing detailed composition maps of the cloud cover and the abundance of gas-phase absorbers. These setups will also provide a much higher cadence.

iv) For objects at the L/T transition, a B2 model with $T_{eff} = 1000K$ and a $1200K$ hot spot predicts the largest photometric variations to be in the J–band; for cooler sources or sources with very cool surface features the ideal wavelength gradually shifts toward 3 μm.

v) We demonstrated that simulated data can be inverted to a correct, low-resolution one-dimensional map of a giant planet.

The observations proposed here will allow detailed studies of the structure and composition of condensate cloud covers in directly imaged exoplanets and provide otherwise inaccessible insights into the atmospheric circulation of these exciting objects.

A Director's Discretionary research grant by the Space Telescope Science Institute was essential for starting this program. We are grateful to Markus Kasper for valuable discussions. We would also like like to acknowledge Justin Rogers for encouraging discussions and for his careful review of this paper.

Telescope	Instrument	Wavelength [μm]	Reference
8–m class ExAO	SPHERE/GPI/PISCES	1 to 2.5	1
30–m class ExAO	GMT/TMT/ELT	1 to 5	2
JWST	NIRCAM/MIRI	1 to 27	3
ATLAST	—	0.1 to 2.4	4

Table A.1 List of instruments we explore: [1] Mesa et al. (2011); Macintosh, et al. (2008); McCarthy et al. (2001); [2] GMT (2006); Macintosh, et al. (2006); Kasper et al. (2008, 2010); [3] Stiavelli et al. (2008) [4] Postman et al. (2010)

Instrument	NACO	SPHERE	GPI	PISCES	PFI	EPICS	NIRCAM
Class	8m AO	8m ExAO	8m ExAO	8m ExAO	30m+ ExAO	30m+ ExAO	JWST
Filter	Ks	J	H	H	H	J	J
Separation [″]	1	1	1	1	0.2	1	
5–σ Contrast	$\sim 10^{-4}$	$\sim 10^{-7}$	$\sim 10^{-8}$	$\sim 10^{-6}$	$\sim 10^{-8}$	$\sim 10^{-9}$	$\sim 10^{-7}$
Reference	1	2	3	4	5	6	7

Table A.2 Sensitivity limits for the instruments we explore at the respective angular separation: [1] Kasper et al. (2007, 2009) [2] Vigan et al. (2010); Mesa et al. (2011) [3] Macintosh, et al. (2008) [4] McCarthy et al. (2001); Skemer et al. (2012) [5] Macintosh, et al. (2006) [6] Kasper et al. (2008, 2010) [7] Green et al. (2005)

Model	Effective Surface		Spot Group 1		Spot Group 2	
	Type	Temp	Type	Temp	Type	Temp
A1	Clear	T_1	Cloudy	T_1	Cloudy	T_1
A2	Clear	T_1	Cloudy	T_2	Cloudy	T_3
B1	Cloudy	T_1	Clear	T_1	Clear	T_1
B2	Cloudy	T_1	Clear	T_2	Clear	T_3
C	Clear	T_1	Clear	T_2	Clear	T_3
D	Cloudy	T_1	Cloudy	T_2	Cloudy	T_3

Table A.3 Six different realizations of the three distinct surface types (Effective Surface, Spot Group 1, Spot Group 2) covering the atmosphere of a giant planet: A1 and A2) cloudy spots on a clear surface; B1 and B2) clear spots on a cloudy surface; C) clear surface with cold and hot clear spots; and D) cloudy surface with cold and hot cloudy spots. T_1, T_2 and T_3 represent three different temperatures.

Appendix B

Acronym glossary

BLS – Box-tting Least Squares

CB – CircumBinary

CBP(s) – CircumBinary Planet(s)

DSS – Digital Sky Survey

EB – Eclipsing Binary

HZ – Habitable Zone

KASI – Korea Astronomy and Space science Institute

KIC – Kepler Input Catalog

LC – Light Curve

MEGNO – Mean Exponential Growth of Nearby Orbits

NexSci – NASA Exoplanet Science Institute

PDCSAP – Pre-search Data Conditioning Simple Aperture Photometry

APPENDIX B. ACRONYMS

RV – Radial Velocity

SAP – Simple Aperture Photometry

TESS – Transiting Exoplanet Survey Satellite

VLT – Very Large Telescope

Vita

Veselin Boyanov Kostov received a B.S. in Physics and Astronomy from Sofia University in 2002. Veselin undertook graduate studies at University of Oklahoma where he received a M.S. in Astrophysics in 2005, and at Columbia University where he received a Master's degree in Geophysics in 2007.

Veselin enrolled in the Ph.D. program at Johns Hopkins University in the fall of 2008. He began his graduate research in 2009 under the guidance of Prof. Daniel Apai, working on direct imaging of giant extrasolar planets. In 2011 his advisor accepted a position at a different institution and Veselin transitioned to studying transiting extrasolar planets. From 2011 to 2014 his research focused on circumbinary planets under the supervision of Dr. Peter McCullough and Prof. Holland Ford. He received a NASA Earth and Space Science Fellowship in 2013. Veselin was awarded his PhD in Physics and Astronomy from JHU in 2014 for his thesis work on discovery and characterization of three of the seven known (at the time) transiting circumbinary systems from NASA's Kepler mission. Veselin will continue his scientific career in the fall of 2014 with Prof. Ray Jayawardhana.